JOHANNES GUTENBERG-UNIVERSITÄT MAINZ
Department of Physics, Mathematics and Computer Science
Institute of Physics

A perfect imperfection: Quantum magnetometry and applications using nitrogen-vacancy defects in diamond

by

Georgios Chatzidrosos

A thesis submitted for the degree of
Doctor of natural sciences

March 2021

Abstract

Work within this thesis advances research into nitrogen-vacancy (NV) defects in diamond. The NV center has proven to be a perfect candidate for metrology applications, including optical sensing of magnetic fields, electric fields, strain, rotations, and temperature. Its energy level structure can also be used as a qubit in quantum computing protocols. Some advantages of the NV center are: it can operate at any temperature range, its broad bandwidth, and its ability to measure magnetic fields with high sensitivity while boasting nano-scale spatial resolution due to its small size (nm-scale for single NV). Its size also makes it ideal for applications in industry where miniaturization and scalability are essential. Specifically, this dissertation presents the necessary theory needed to understand the physics of NV centers and various sensors we designed and constructed during my PhD, with the goal of exploring alternative methods for magnetometry or solving problems that competing magnetic technologies face. These sensors include:

- A miniaturized magnetometer, with a footprint of $390\,\mu\text{m} \times 4500\,\mu\text{m}^2$, that has achieved the second-highest sensitivity amongst NV magnetometers to date. Additionally, this sensor is based on an alternative magnetometric technique with NV centers, measuring absorption rather than fluorescence.
- A microwave-free magnetometer based on the NV ground-state level anti-crossing, which can operate in a dynamic environment where use of microwaves might be detrimental. Again, it achieved higher sensitivity than its peers at the time of publication.
- An eddy-current-detection NV-based sensor, which was the first of its kind and introduced NV centers to a well-established industry sector.
- A fiberized NV-based vector magnetometer, which advanced the efforts of the field towards a miniaturized, robust, and portable sensor.

Many of the investigated techniques for the construction of these sensors have been demonstrated with NV ensembles, but they are potentially applicable to single-NV sensors as well. Finally, I present simulations and analysis for a new sensor constructed to address shortcomings of previous NV sensors to fulfill all the criteria for endoscopic applications.

Declaration of Authorship

I, Georgios Chatzidrosos, declare that the thesis entitled *A perfect imperfection: Quantum magnetometry and application using Nitrogen-Vacancy defects in diamond.* and the work presented in the thesis are both my own, and have been generated by me as the result of my own original research. I confirm that:

- this work was done wholly or mainly while in candidature for a research degree at this University;
- where any part of this thesis has previously been submitted for a degree or any other qualification at this University or any other institution, this has been clearly stated;
- where I have consulted the published work of others, this is always clearly attributed;
- where I have quoted from the work of others, the source is always given. With the exception of such quotations, this thesis is entirely my own work;
- with the oversight of my main supervisor, editorial advice has been sought. No changes of intellectual content were made as a result of this advice.
- I have acknowledged all main sources of help;
- where the thesis is based on work done by myself jointly with others, I have made clear exactly what was done by others and what I have contributed myself;

Signed: Georgios Chatzidrosos

Date: *1st December 2020*

Contents

List of Figures

List of Tables

List of Abbreviations

Abbreviation	Description	Chapter
AOM	**A**cousto-**O**ptical **M**odulator	§§3, 4
AR	**A**nti-**R**eflective	§3
BW	**B**and**W**idth	§2
CAD	**C**omptuter-**A**ided **D**esign	§7
CVD	**C**hemical **V**apor **D**eposition	§§2, 4
DQ	**D**ouble **Q**uantum	§6
ECDL	**E**xternal-**C**avity **D**iode **L**aser	§3
EM	**E**lectro-**M**agnet	§5
EPR	**E**lectron **P**aramagnetic **R**esonance	§4
ESLAC	**E**xited-**S**tate **L**evel **A**nti-**C**rossing	§4
FM	**F**requency **M**odulation	§2
FWHM	**F**ull **W**idth at **H**alf **M**aximum	§§3, 4, 6
IR	**I**nfra**R**ed	§§2, 3, 8
ISC	**I**nter-**S**ystem **C**rossing	§2
GRIN	**G**gradient-**I**ndex **L**ens	§6
GSLAC	**G**round-**S**tate **L**evel **A**nti-**C**rossing	§§1, 2, 4, 6
HPHT	**H**igh **P**ressure **H**igh **T**emperature	§§2–4, 6
HR	**H**igh **R**eflective	§§3, 7
JGU	**J**ohannes **G**utenberg-**U**niversität	§7

Abbreviation	Description	Chapter
LCAO	**L**inear **C**ombincations of **A**tomic **O**rbitals	§2
LIA	**L**ock-**I**n **A**mplifier	§§2–6
LO	**L**ocal **O**scilator	§§3, 4
MO	**M**olecular **O**rbitals	§2
MF	**M**agnetic **F**ield	§4
MW	**M**icro**W**ave	§§1–4, 6–8
NMR	**N**uclear **M**agnetic **R**esonance	§§2, 8
NV	**N**itrogen **V**acancy	§§1–8
ODMR	**O**ptically **D**etected **M**agnetic **R**esonance	§§1–4, 6, 7
PC	**P**ersonal **C**omputer	§5
PD	**P**hoto**D**etector	§§6, 7
PCB	**P**rinted **C**ircuit **B**oard	§5
PID	**P**roportional-**I**ntegral-**D**erivative controller	§§3, 4, 6, 7
PL	**P**hoto**L**uminescence	§§2–7
PS	**P**ower**S**upply	§§2–4
RF	**R**adio**F**requency	§5
SQUID	**S**uperconducting **QU**antum **I**nterference **D**evice	§§1, 3, 8
TEM	**T**ransverse **E**lectro**M**agnetic	§3
ZULF	**Z**ero-to-**U**ltra-**L**ow-**F**ield	§8

List of Symbols

Symbol	Description	Notes	Chapter
$\lvert\gamma_e/2\pi\rvert$	electron gyromagnetic ratio over 2π	$\simeq 28.024$ GHz T^{-1}	§§1, 2, 4, 7
$\lvert\psi\rangle$	a ket vector in Hillbert space		§2
${}^3A_2, {}^3E$	Mulliken symbols for NV triplet states		§§2–7
${}^1E, {}^1A_1$	Mulliken symbols for NV singlet states		§§2–7
$\alpha_n, \alpha_c, \alpha_1, \alpha_1', e^x, e^y$	electron orbital states		§2
Γ_i	excitation rate of i		§2
γ_n	nuclear gyromagnetic ratio over 2π		§2
σ_i	absorption cross-section for i		§2
σ_i	conductivity of i		§5
H_i	Hamiltonian, energy operator of i		§2
$\vec{B} = (B_z, B_x, B_y)$	Magnetic field vector	B_i projection on i	§2
$\vec{I} = (I_z, I_x, I_y)$	nuclear spin operator	I_i projection on i	§2
$\vec{S} = (S_z, S_x, S_y)$	Electron spin operator	S_i projection on i	§2
T_2	spin relaxation time		§2
T_2^*	effective spin relaxation time		§1
k_{xy}	decay rate from x to y level		§2
W_i	pump rate associated with i		§2

Preface

Previously Published Work

Much of the work presented in this dissertation has been previously published.

The following publications constitute main works contributing to this thesis and are included in full with minor changes:

Ref. [26]: **G. Chatzidrosos**, A. Wickenbrock, L. Bougas, N. Leefer, T. Wu, K. Jensen, Y. Dumeige, and D. Budker. Miniature Cavity-Enhanced Diamond Magnetometer. Phys. Rev. Applied 8, 044019 (2017)

Ref. [119]: H. Zheng, **G. Chatzidrosos** , A. Wickenbrock, L. Bougas, R. Lazda, A. Berzins, F. H. Gahbauer, M. Auzinsh, R. Ferber, D. Budker, *Level anti-crossing magnetometry with color centers in diamond*, Proc. SPIE. 10119 (2017)

Ref. [27]: **G. Chatzidrosos**, A. Wickenbrock, L. Bougas, H. Zheng, O. Tretiak, Y. Yang, D. Budker,Eddy-current imaging with nitrogen-vacancy centers in diamond, Phys. Rev. Applied 11, 014060 (2019)

Ref. [25] **G. Chatzidrosos**, J. S. Rebeirro, H. Zheng, T. Schneemann, M. Omar, P. Bluemler, D. Budker, A. Wickenbrock, *Fiberized diamond-based vector magnetometers* , arXiv:2102.11902 (2021)

The following co-authored publications constitute minor works contributing to this thesis and are included in part or referenced for the purpose of analysis:

Ref. [42] Y Dumeige, J.-F. Roch, F. Bretenaker, T. Debuisschert, V. Acosta, C. Becher, **G. Chatzidrosos**, A. Wickenbrock, L. Bougas, A. Wilzewski, D. Budker,

Infrared laser magnetometry with a NV doped diamond intracavity etalon , Optics Express, Vol. 27, Issue 2, pp. 1706-1717 (2019)

Ref. [120] H. Zheng, Z. Sun, **G. Chatzidrosos**, C. Zhang, K. Nakamura, H. Sumiya, T. Ohshima, J. Isoya, J. Wrachtrup, A. Wickenbrock, and D. Budker, *Microwave-free vector magnetometry with nitrogen-vacancy centers along a single axis in diamond*, Phys. Rev. Applied, 13, 044023, (2020)

Ref. [54] V. Ivády, H. Zheng, A. Wickenbrock, L. Bougas, **G. Chatzidrosos**, K. Nakamura, H. Sumiya, T. Ohshima, J. Isoya, D. Budker, Igor A. Abrikosov, A. Gali, *Photoluminescence at the ground state level anticrossing of the nitrogen-vacancy center in diamond* ,Phys. Rev. B 103, 035307 (2021)

Ref. [114] A. Wickenbrock, H. Zheng, **G. Chatzidrosos**, J. S. Rebeirro, T. Schneemann, P. Bluemler, *High homogeneity permanent magnet for diamond magnetometry* , Journal of Magnetic Resonance, 3, 106867 (2021)

Ref. [67] T. Lenz, **G. Chatzidrosos**, Z. Wang, L. Bougas, Y. Dumeige, A. Wickenbrock, N. Kerber, J. Zázvorka, F. Kammerbauer, M. Kläui, Z. Kazi, K.-M. C. Fu, K. Itoh, H. Watanabe, D. Budker, *Probing topological spin structures using light-polarization and magnetic microscopy*, Phys. Rev. Applied 15, 024040, (2021)

Ref. [118] X. Zhang, **G. Chatzidrosos**, Y. Hu, H. Zheng, A. Wickenbrock, A. Jerschow, D. Budker, *Battery characterization via eddy-current imaging with nitrogen-vacancy centers in diamond*, Appl. Sci. 11(7), 3069 (2021)

§ 1

Introduction

§ 1.1 Background and motivation

In modern days quantum metrology sensors are widely employed for measurements of magnetic fields. One way to perform such measurements are magnetometers based on nitrogen vacancy (NV) centers in diamond. Sensitivity-limit estimates for them compare favorably with the currently most sensitive devices, depending on the intended application. The main competitors of NV-based sensors include superconducting quantum interference device (SQUIDs) and atomic vapor cell magnetometers. The key as to why, a comparison between the sensors favors the NV, lies in the fundamental limit for all spin-based magnetometers, the quantum noise associated with spin projection. For time of measurement t_m, this noise can be estimated by the following formula [23, 106]

$$\delta B_q \approx \frac{1}{\gamma_e/2\pi} \frac{1}{\sqrt{nVT_2^*}}, \tag{1.1}$$

where $\delta \mathrm{B}_q$ is the minimum detectable magnetic field, $|\gamma_e/2\pi| \simeq 28.024\,\mathrm{GHz\,T^{-1}}$is the gyromagnetic ratio of the electron spin [102], n is the density of the spins, V is the volume, T_2^* is the effective spin relaxation. Note that $\mathrm{t}_m \geq \mathrm{T}_2^*$.

Comparisons between different kinds sensors can be found in literature (e.g. Ref. [110]) with most of them based on projected sensitivity from equation eq. (1.1). Other than the favorable theoretical limit of quantum spin-projection noise, NV based sensors present a few other advantages as well. Some of them include the possibility to achieve nm-scale spatial resolution [12, 77, 91, 106], the ability to

operate at any temperature range without significant drawbacks [3], their high bandwidth [27], and their bio-compatibility to name a few.

Setting aside fundamental limits, atomic vapor cells and SQUIDs have both demonstrated more sensitive sensors with $160\,\mathrm{aT}/\sqrt{\mathrm{Hz}}$ [31] and $150\,\mathrm{aT}/\sqrt{\mathrm{Hz}}$ [103] sensitivities, respectively. Despite their high sensitivity though, both technologies suffer from other disadvantages. Atomic vapor cells, for example, lack nm-scale spatial resolution, due to the thermal motion of the atoms in the cells. By employing a high density of a noble gas, vapor-based magnetometry with a spatial resolution of ~ 10 μm is possible [80], but despite impressive results for mm-scale sensors [64, 98] the projected sensitivity for this length scale is exceeded by the diamond-based sensors. Furthermore, for optimal operation, vapor-based cells must be heated to well above room-temperature, which increases the power consumption and limits the range of applications. In the case of SQUIDs, better spatial resolution is possible, but the operating temperature range is cryogenic, limiting the range of applications. For both vapor cells and SQUID magnetometers the heating or cooling, needed for optimal operation, can limit the achieved proximity of the sensors to the magnetic-field sources, which in turn reduces the amplitude of the detected magnetic-field signal by them.

Unfortunately, most NV-based magnetometers fail to reach the limit set by eq. (1.1). The most sensitive NV-based sensors currently, are limited by another statistical limit, the photon shot-noise [16,26], which is calculated from the following equation

$$\delta B_p \approx \frac{1}{\gamma_e/_{2\pi}} \frac{\Delta\nu_{\mathrm{mr}}}{C\sqrt{\mathcal{R}}}, \tag{1.2}$$

where $|{}^{\gamma_e D}/_{2\pi}| \simeq 28.024\,\mathrm{GHz\,T^{-1}}$ is the gyromagnetic ratio of the electron spin, and $\mathcal{R}$ is the rate of detected photons. $\Delta\nu_{\mathrm{mr}}$ and C are the full width at half maximum (FWHM) linewidth and contrast of the resonance feature used for magnetometry, respectively.

It follows that, to achieve higher magnetic field sensitivity, the ratio of contrast to linewidth as well as the photon-collection rate $\mathcal{R}$, needs to be optimized. Unfortunately, the photon collection rate for most NV sensors is poor, with active research to overcome this problem still ongoing [1, 26, 41, 42, 49, 58, 63, 101]. The ratio of linewidth and contrast can be optimized up to a degree, but it is mostly diamond-sample dependent. The sensors presented in this dissertation, show my efforts to overcome the aforementioned shortcoming and aimed to allow the NV

to compete in research fields, where its competitors are established and where it had no access before, e.g. eddy-current imaging and endoscopy.

§ 1.2 Thesis outline

Chapter 1

This chapter motivates the importance of NV magnetometers, compares them with competing technologies and presents the outline of the thesis.

Chapter 2

This chapter gives an introduction to NV centers in diamond. It explains what NV centers are, how they can be formed in bulk diamond, their electronic structure and what applications they can be used for. It also details the basics principles of DC magnetometry using NV centers, with emphasis on the direction the field is headed towards.

Chapter 3

The chapter presents a highly sensitive miniaturized cavity-enhanced room-temperature magnetic-field sensor based on nitrogen-vacancy centers in diamond. The magnetic resonance signal is detected by probing absorption on the 1042-nm spin-singlet transition. To improve the absorptive signal the diamond is placed in an optical resonator. The device has a magnetic-field sensitivity of $28\,\mathrm{pT}/\sqrt{\mathrm{Hz}}$, a projected photon shot-noise-limited sensitivity of $22\,\mathrm{pT}/\sqrt{\mathrm{Hz}}$, and an estimated quantum projection-noise-limited sensitivity of $0.43\,\mathrm{pT}/\sqrt{\mathrm{Hz}}$ with the sensing volume of $\sim 390\,\mu\mathrm{m} \times 4500\,\mu\mathrm{m}^2$. The presented miniaturized device can be the basis for an endoscopic magnetic-field sensor for biomedical applications.

Chapter 4

This chapter presents developments in magnetic field sensing with negatively charged NV in diamond, employing magnetic-field dependent features in the photoluminescence and eliminating the need for microwaves. Two approaches towards improving the magnetometric sensitivity using the ground-state level anti-crossing (GSLAC) feature of the NV center at a background magnetic-field of 102.4 mT are discussed. Following the first approach, the GSLAC feature parameters are investigated for precise alignment in a dilute diamond sample; the second approach extends the sensing protocol into absorption via detection of the GSLAC in the diamond transmission of a

1042 nm laser beam. This leads to an increase of GSLAC contrast and results in a magnetometer with a sensitivity of $0.45\,\mathrm{nT}/\sqrt{\mathrm{Hz}}$ and a photon shot-noise limited sensitivity of $12.2\,\mathrm{pT}/\sqrt{\mathrm{Hz}}$

Chapter 5

This chapter presents microwave-free eddy current imaging using NV centers in diamond. By detecting the eddy current induced magnetic field of conductive samples, we can distinguish between different materials and shapes and identify structural defects. Our technique allows for the discrimination of different materials according to their conductivity. The sensitivity of the measurements is calculated as $8\times10^5\,\mathrm{S/m}\,\sqrt{\mathrm{Hz}}$ at 3.5 MHz, for a cylindrical sample with radius $\mathrm{r_0} = 1\,\mathrm{mm}$ and height $\mathrm{h} = 0.1\,\mathrm{mm}$ (volume $\sim 0.3\,\mathrm{mm}^3$), at a distance of 0.5 mm. In comparison with existing technologies, the diamond-based device exhibits a superior bandwidth and spatial resolution. In particular, we demonstrate a flat frequency response from DC to 3.5 MHz and a spatial resolution of $348 \pm 2\,\mu\mathrm{m}$.

Chapter 6

This chapter, presents two fiberized vector magnetic-field sensors, based on NV centers in diamond. The sensors feature sub-$\mathrm{nT}/\sqrt{\mathrm{Hz}}$ magnetic sensitivity. The sensors are constructed with commercially available components that achieve small sensor size, high photon collection, and minimal sensor-sample distance. Both sensors are located at the end of optical fibers with the sensor-head freely accessible and robust under movement. These features make them ideal for mapping magnetic fields with high sensitivity and spatial resolution ($\geq$ mm). As a demonstration we use one of the sensors to map the vector magnetic field inside the bore of a $\leq 100\,\mathrm{mT}$ Halbach array. The vector field sensing protocol translates microwave spectroscopy data addressing all diamonds axes and including double quantum transitions to a 3D magnetic field vector.

Chapter 7

This chapter, presents the ongoing efforts for a new NV-based magnetic field sensor that can be used for endoscopic applications. The design of the sensor is discussed in detail, explaining how it can be used to solve issues that the previous NV sensors we constructed faced, simulations of photon collection efficiency, temperature management and microwave delivery are presented. The properties of the sensor and its ability to operate at zero-magnetic field conditions, in combination with the advantages of NV-based magnetometers,

mentioned throughout the thesis, make it an ideal candidate for biological measurements as an endoscope.

Chapter 8

This chapter, presents a summary of the most important findings of this thesis, as well as an outlook, on future NV-related projects and the field of NV center research in general.

§ 2

Nitrogen-vacancy centers in diamond

§ 2.1 A brief history of nitrogen-vacancy centers

The modern history of the nitrogen-vacancy (NV) center begins in the late 1970s, when an optical transition at 637 nm and a characteristic electron magnetic resonance spectrum obtained with irradiated diamonds were assigned successfully to the NV center in diamond [33,68]. Later in the 1980s, the photoluminescence (PL) related to emission to the NV electric ground spin state was identified [90], and the effects of microwave (MW) irradiation resulting in optically detected magnetic resonances (ODMR) of NV centers in a bulk of diamond were studied [20, 108]. About a decade later, with the use of a scanning confocal optical microscope, ODMR was also observed with a single NV center [48].

In the 2000s coherent control of a single electron spin of the NV center, with application of MW and radio-frequency pulse sequences was demonstrated. This led to coherent control of a single electron spin of the NV center [56] and demonstrated strong coupling between the ^{13}C nuclear spin to the NV electron spin [55]. Due to these results demonstrating two-qubit manipulations with the NV electron spin and ^{13}C nuclear spin at room temperature, the NV has been considered a promising candidate for quantum information processing e.g. quantum computing and quantum communication.

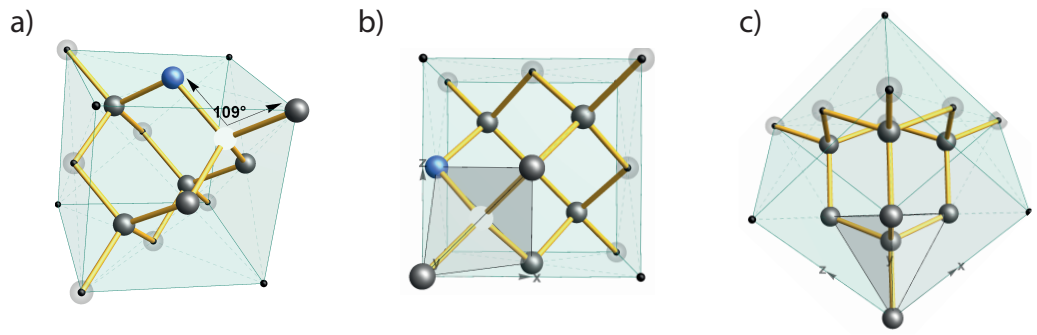

FIGURE 2.1: NV structure from different angles (a) arbitrary (b) cut along (100) plane (c) cut along the (111) plane.

In 2008, NV centers where proposed as quantum sensors for highly sensitive magnetometry [105]. Both single and ensemble electron spins could be used for magnetometry. Single NV was proposed as a probe for scanning magnetometry [18,28] and ensembles of NVs as pixels for optical magnetic imaging. In both cases, DC and AC magnetic field sensing would be possible using MW pulse protocols developed in conventional nuclear magnetic resonance (NMR) such as Ramsey, Hahn-echo, and dynamical decoupling sequences.

In 2010, after previously being mentioned in literature [21, 60], the temperature dependence of the NV zero-field splitting was studied [3], enabling the NV to be used for thermometry applications. Within the next few years new sensors based on NV centers in diamond were also used to measure electric fields [5, 40], as well as rotation [6, 65, 70] and strain [39, 85]. Through all these applications, as well as the advantages mentioned on the previous chapter, the NV center in diamond was established to be a highly versatile sensor, with high spatial resolution and sensitivity. Some prominent examples of sensing with NV centers in recent years include, single neuron action-potential detection [16], single-protein spectroscopy [69], as well as in-vivo thermometry [61].

§ 2.2 Physical structure and formation

The NV center is a point defect in the diamond lattice. It consists of a substitutional nitrogen atom adjacent to a vacancy i. e. a missing carbon atom. NV centers can exist in different charge states, but the one used for magnetometry is the NV^- state. The NV^- center has six electrons. Five of the electrons are contributed from the dangling bonds of the three neighboring carbon atoms and

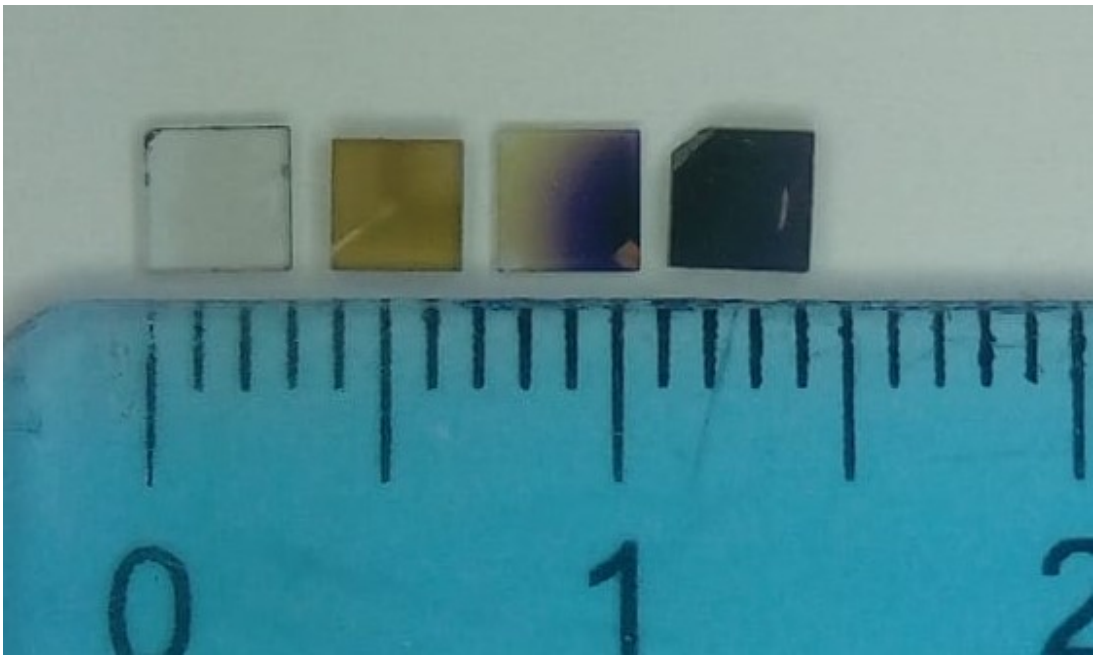

FIGURE 2.2: Photograph of single crystal HPHT diamonds. The samples contain from left to right: little to no impurities, added nitrogen, a gradient NV concentration (low to the left, high on the right) and a sample with very high (> 80 ppm) NV concentration.

the nitrogen atom. One extra electron is captured from an electron donor, usually another nitrogen atom in the lattice, and gives rise to the negative charge state. Throughout this thesis we refer to the NV^- when talking about NV, unless explicitly stated otherwise. The axis defined by the vacancy and the nitrogen atom is called the NV axis. There are four possibilities for the nitrogen atom to be positioned with respect to the vacancy, aligned parallel to one of four <111> crystallographic axes of diamond lattice ([111], $[\bar{1}\,\bar{1}1]$, $[1\bar{1}\,\bar{1}]$, and $[\bar{1}1\bar{1}]$), leading to four possible NV alignments. The NV center has C_{3V} spatial point-group symmetry. This means that, it has a 3-fold axis and 3 vertical mirror planes (in this case defined by the NV axis and one of the three neighboring carbon atoms), for this reason it is also symmetric to rotations of 0, 120^o and 240^o around the NV axis. Because of the symmetry group, the energy levels of NV can be constructed by linear combinations of atomic orbitals (LCAO) group-theoretical approach [38,76]. Typically diamond crystals are cut along different planes in Fig. 2.1 we see the NV center structure from several different angles. Figure 2.1 (a) shows a random angle and Fig. 2.1 (b) and (c) show the NV orientations after the diamond has been cut along the (100) and (111) planes respectively.

Artificial diamonds with NV centers are mainly constructed in two ways; high pressure high temperature (HPHT) synthesis [24] and chemical vapor deposition

(CVD) [82, 84]. As the name suggests, in the HPHT method a diamond crystal is grown under high pressure ($> 5\,\text{Gbar}$) and high temperature (>1250 ^{o}C). This method makes use of a solvent-catalyst for carbon-source dissolution to increase the growth rate and relax the pressure and temperature requirements, as well as allow better composition control. By varying the composition of the metal solvent catalyst, nitrogen can be easily incorporated into the diamond lattice during this process [37, 59, 86]. On the other hand in CVD growth, a diamond seed is placed into a heated growth chamber ($\sim 800\,^o$C). During the growth, plasma of various elements and molecules is introduced into the chamber, such as hydrogen mixed with methane (which acts as a carbon source) or oxygen and argon [53]. With careful control of hydrogen etching and carbon deposition rates, net diamond growth can be achieved [8]. The introduction of plasma into the growth chamber can be finely controlled resulting in high-purity diamond crystals. CVD synthesis can also be used to produce thin or doped layers from nanometer to micrometer thickness [78, 83].

NV centers can also be introduced in smaller amounts to a diamond crystal after synthesis. This is achieved by implantation of ions, most commonly N^+ and N_2^+ [79, 88, 89]. Typically bulk NV samples are irradiated with e^- in the MeV energy range. During the ion implantation and irradiation the crystal is damaged, creating vacancies. These vacancies can be mobile if the diamond crystal is heated to temperatures above $600\,^o$C [34] and often form bound states with adjacent nitrogen impurities, resulting in NV centers.

The creation of diamond samples with NV centers has evolved into its own research field, involving many different research groups [2,3,14,46,93,96,97] and companies (e.g. Element Six) trying to create high-purify diamonds containing long-coherence time NV centers.

Figure 2.2 shows four different samples created with the HPHT method. The leftmost sample is a an artificial diamond with little to no impurities, resulting in a transparent color. To its right we see a sample with added nitrogen without irradiation, giving it yellowish color. The third sample in the row is an irradiated diamond sample with added nitrogen, the sample was irradiated with a different dosage of electrons (from its left to right side) creating a gradient NV concentration (low to the left, high on the right), the higher the NV concentration in the sample the deeper purple color the diamond gets. Finally the further-right sample has very high ($> 80\,\text{ppm}$) NV concentration resulting in an almost black color.

§ 2.3 Electronic structure

The NV^- center is a system involving six electrons. Three electrons are contributed by neighboring carbons, two come from the N atom of the NV and one more electron is given by a donor in the diamond lattice, most commonly another N atom. One can use LCAO, to combine the atomic orbitals from the three C and the N atoms (c_1, c_2, c_3, n, respectively) into Molecular orbitals (MO). These can be further transformed into the following irreducible representations by taking into account the C_{3v} NV symmetry [38, 66, 76]:

$$\begin{aligned} a_n &= n, \\ a_c &= \frac{c_1 + c_2 + c_3}{3}, \\ e_x &= \frac{2c_1 - c_2 - c_3}{\sqrt{6}}, \\ e_y &= \frac{c_2 - c_3}{\sqrt{2}}. \end{aligned} \tag{2.1}$$

From a group-theory standpoint, a_n and a_c are invariant under the C_{3v} symmetry operations and lead into the irreducible representation of A_1. Here A is the Mulliken symbol that represents symmetry with respect to rotation around the principal rotational axis. The e_x and e_y MOs can transform as the rank-two irreducible representation E, where E signifies degenerate (German: entartet). As a next step, if we take into account Coulomb interaction between the electrons we end up with two mixed states of a_n and a_c, which form new representations:

$$\begin{aligned} a_1' &= \sqrt{1-\alpha^2}\, n - \frac{\alpha}{\sqrt{3}}(c_1 + c_2 + c_3), \\ a_1 &= \alpha\, n - \sqrt{\frac{\alpha}{3}}\,(c_1 + c_2 + c_3). \end{aligned} \tag{2.2}$$

This leads to a new overall base of MOs $\{a_1', a_1.e_x, e_y\}$. The MOs can then be sorted in energy by symmetry and the Coloumb interaction [38, 76].

A schematic of the six-electron configuration of the NV for its ground state is depicted in Fig. 2.3. The first exited state would be produced with an excitation

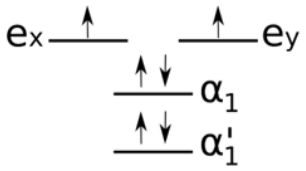

FIGURE 2.3: Six-electron configuration of the NV for its ground state. The arrows symbolize electrons and the orientation denotes spin state up or down.

Configuration	C_{3V} term	Wavefunction	Spin (S)	m_s
a_1e	^3E	$\|a_1\bar{e}_x\rangle+\|\bar{a}_1e_x\rangle$	1	0
		$\|\bar{a}_1\bar{e}_x\rangle$		-1
		$\|a_1e_x\rangle$		+1
		$\|a_1\bar{e}_y\rangle+\|\bar{a}_1e_y\rangle$		0
		$\|\bar{a}_1\bar{e}_y\rangle$		-1
		$\|a_1e_y\rangle$		+1
	^1E	$\|a_1\bar{e}_x\rangle-\|\bar{a}_1e_x\rangle$	0	0
		$\|a_1\bar{e}_y\rangle-\|\bar{a}_1e_y\rangle$		
e^2	$^1A_1$	$\|e_x\bar{e}_x\rangle+\|e_y\bar{e}_y\rangle$	0	0
	^1E	$\|e_x\bar{e}_x\rangle-\|e_y\bar{e}_y\rangle$	0	0
		$\|\bar{e}_xe_y\rangle-\|e_x\bar{e}_y\rangle$		
	$^3A_2$	$\|\bar{e}_xe_y\rangle+\|e_x\bar{e}_y\rangle$	1	0
		$\|\bar{e}_x\bar{e}_y\rangle$		-1
		$\|e_xe_y\rangle$		+1

TABLE 2.1: NV electronic levels. The ground electron levels belong to the e^2 configuration, while the a_1e to the exited states. The wavefunction as well as the total spin, S and projection m_s are indicated in their respective columns.

of an electron from the α_1 state to either e_x or e_y. Due to the NV being a six-electron system while the available levels allow for up to eight electrons, it is useful to track the two holes that result from the non-filled orbitals. On this logic, the example shown in Fig. 2.3 can be represented with a $|e_x, e_y\rangle$ wavefunction. Writing down all the unique wavefunctions for the system leads us to Table 2.1.

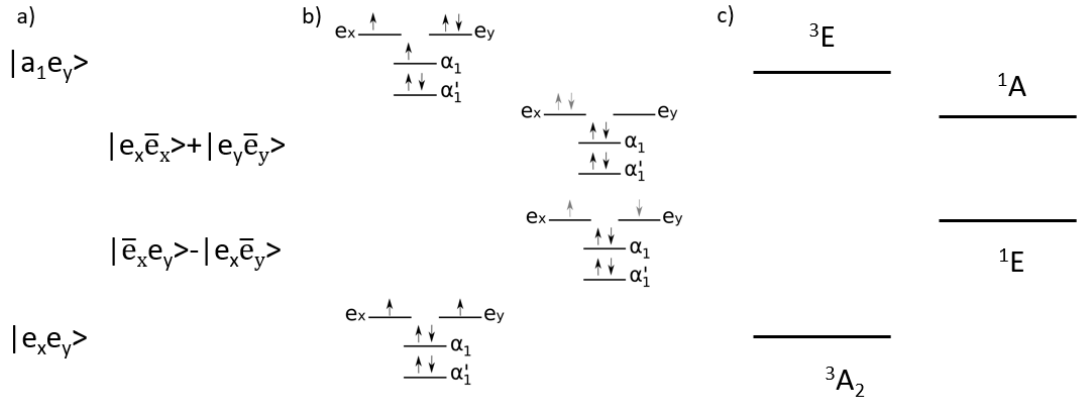

FIGURE 2.4: NV energy levels example at different representations a) wavefunctions b) six-electron configuration schematics c) C_{3v} terms.

§ 2.4 Energy levels

By matching the different wavefunctions and six electron configuration schematics to their C_{3v} terms, we can represent the energy levels with a picture familiar to those working in the field of NV physics, as seen in Fig. 2.4.

The picture depicted in Fig. 2.4 can be further evolved by writing down terms of the NV Hamiltonian (Eq. 2.3) and implementing their effect. Ignoring effects that are not studied in this thesis (e.g., interaction with P1 centers), the Hamiltonian can be approximated as:

$$H_{NV} = D\,S_z^2 + E(S_y^2 + S_x^2) - \gamma_e \vec{B}\vec{S} + P\,I_z^2 - \gamma_n \vec{B}\vec{I} + A\vec{S}\vec{I}. \tag{2.3}$$

The first three terms can be referred to as the spin Hamiltonian. The first term, with $D = 2\,\pi(2.87\,[\mathrm{GHz}] - 78\,[\frac{\mathrm{kHz}}{\mathrm{K}}]\,\Delta\mathrm{T} + 3.5[\frac{\mathrm{kHz}}{\mathrm{V/\mu m}}])$ for the ground state, at room temperature and S_z the projection of the electron spin operator along z, results in the splitting of the triplet states, and is also responsible for the NV being sensitive to temperature and transverse electric fields, the longitudinal term is omitted here. The second term, with E being constant and S_y, S_x being the projections of the electron spin along y and x, respectively, lifts the degeneracy between $m_s = +1$ and $m_s = -1$ states. The third term, with γ_e being the electron gyromagnetic ratio, $\vec{B}$ the magnetic field and $\vec{S}$ the electron spin operator, represents the Zeeman effect and gives the NV its sensitivity to magnetic fields. Terms four and five can be

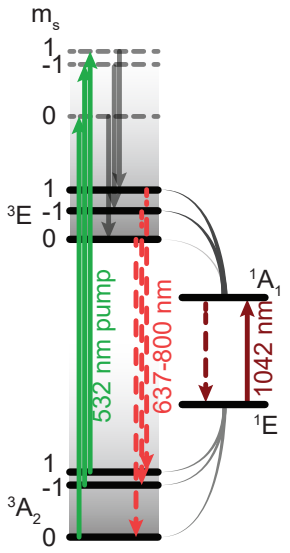

FIGURE 2.5: Schematic of NV energy levels. After taking into account the Hamiltonian and effects due to the NV phonon sidebands. The phonon sidebands of the singlet are omitted from this figure.

referred to as the nuclear Hamiltonian, with $\vec{I}$ being the nuclear spin operator and I_z its projection along the z axis, P is a constant and γ_n is the nuclear gyromagnetic ratio. Term six represents the hyperfine interaction with A being constant. We do not focus on the nuclear and hyperfine terms of the Hamiltonian in this Thesis, but refer back to the hyperfine term at Chapter 2.6 when we discuss ODMR in more detail.

Other effects that we have to consider relate to the NV being a solid-state system. Due to this excitation with smaller wavelengths (higher energy), than its zero-photon line (637 nm for the triplet states and 1042 nm for the singlet state) is allowed, due to a phonon sideband. Additionally, the phonon sideband can be used to achieve inter-system crossing (ISC), thus allowing transitions from the triplet to the singlet states. By including the effects mentioned above in Fig. 2.4 (c) we proceed to a more complete picture shown in Fig. 2.5. There, we are considering the NV to be at room temperature and thus only spin conserving excitations and de-excitations are depicted. This selection rule applies for the NV at room temperature, because the spin-orbit interaction is about 5 GHz (vs 6 THz corresponding to room temperature), but at low temperatures in the absence of strain optical transitions are allowed [17] and have been used to demonstrate spin-photon entanglement [22].

§ 2.5 Optical excitation & ionization

An important feature of the NV center is that it can be optically initialized to the $^3A_2$ triplet, $m_s = 0$ state, by light illumination, that drives the transition between all the sublevels of $^3A_2$ to the ^3E sublevels. This occurs due to a spin-dependant decay rate of the ^3E exited triplet state to the $^1A_1$ exited singlet state. The decay rates for the NV^-, as well as NV^0 energy levels, along with the absorption cross-section of the two for green and infrared light are show in Fig.2.6 (b). Comparing the decay rates k_{45} and k_{42} one can see that once population reaches the ^3E, $m_s = \pm 1$, states, it is more likely that it will undergo ISC and pass through the singlet states before ending up in the $^3A_2$ triplet ground state. We note here that the probability of the singlet state population decaying to $^3A_2$, $m_s = 0$ is higher as well, k_{61} and k_{62} but to a smaller degree than k_{45} and k_{42}. Population that is transferred in the $^3A_2$, $m_s = 0$ state has a higher probability to return there after an optical excitation and de-excitation cycle. Thus after many excitation cycles population is initialized to the $^3A_2$, $m_s = 0$ state.

After approximately a microsecond of illumination with green light a steady state is established with the $^3A_2$, $ms = 0$ state overpopulated at a polarization level of up to 80 % [92]. In this way, the electron spin of the NV can be hyperpolarized at room temperature with a single laser, and without the need for cryogenic or high temperature or application of external magnetic fields. This property makes the NV a promising candidate for quantum computing applications, as well as application where hyperpolarization is essential, e.g. Nuclear Magnetic Resonance (NMR).

The NV^- is not photochemically stable. Thus, an unwanted effect of illuminating NV^- with light resonant with the $^3A_2$ to ^3E transition is its ionization from NV^- to NV^0 [72]. When modeling the photo dynamics of the NV it is necessary to take this into account. Even though a detailed analysis is beyond the scope of the current chapter, we will mention here that the final ratio of NV^- and NV^0, depends on the excitation light intensity and wavelength and is $\leq 75\%$ [11, 72].

§ 2.6 ODMR

After the NV has been initialized to the $^3A_2$, $m_s = 0$ state, the most common way to measure magnetic fields is by ODMR. To achieve this, one can apply a MW field

a)

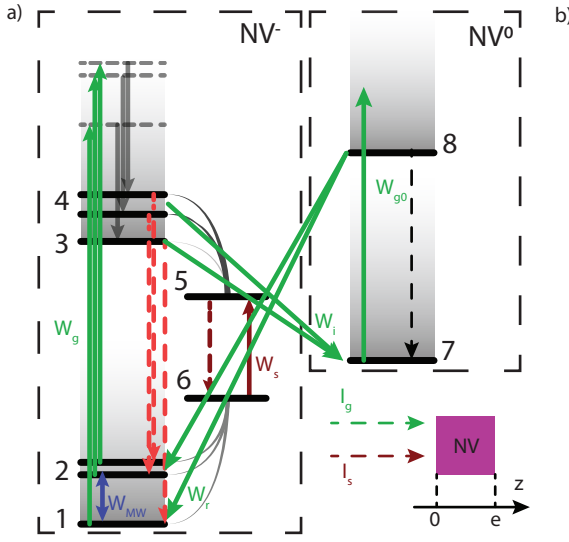

b)

Parameter	Value
$K_{31} = k_{42}$	(66 ± 5) μs^{-1}
K_{35}	(7.9 ± 4.1) μs^{-1}
K_{45}	(53 ± 7) μs^{-1}
K_{61}	(1.0 ± 0.8) μs^{-1}
K_{62}	(0.7 ± 0.5) μs^{-1}
K_{56}	1 ns^{-1}
k_{87}	(53 ± 7) μs^{-1}
σ_g	3.0×10^{-21} m^2
σ_{g0}	$1.8\sigma_g$
σ_i	$(9.5 \pm 4.7) \times 10^{-21}$ m^2
σ_r	$(9.8 \pm 4.9) \times 10^{-21}$ m^2
σ_s	$(6.1 \pm 4.4) \times 10^{-23}$ m^2

FIGURE 2.6: a) Description of the photodynamics between the spin sublevels of the NV^- and NV^0 ground and excited electronic states. W_g is the pumping rate associated to the NV^- and W_{g0} that of the NV^0. W_s is the transition rate of the infrared (IR) singlet resonance. W_i and W_r are respectively the ionization and recombination rates from NV^- to NV^0. W_{MW} is the $m_s = 0$ to $m_s = \pm 1$ transition rate, which can be induced by resonant MW field. The insert shows pumping by green light and IR, with propagation through a diamond plate of thickness e. b) Decay rates and absorption cross sections for the NV^- and NV^0 system. Decay rates are represented in the form of k_{xy}, where x is the initial and y is the final level. The absorption cross sections are: σ_g for green light and the NV^-, σ_{g0} for green light and the NV^0, σ_i for ionization of NV^- to NV^0 caused by green, σ_r for the recombination of NV^0 to NV^- caused by green and σ_s the IR light absorption cross-section of the NV^- singlet states. The numbers referenced can be found in Ref. [42].

with a changing frequency around the zero-field splitting of 2.87 GHz, while most commonly, monitoring the NV red fluorescence. Once the MW field is resonant with one of the $m_s = 0$ to $m_s = \pm 1$ transitions, fluorescence will decrease. This happens because population that is exited to the ^3E, $m_s = 0$ most often decays back to the ground triplet state, emitting red florescence, while population exited to the ^3E, $m_s = \pm 1$ partly undergoes non-radiative ISC and goes to the singlet states. A few examples of ODMR spectra can be seen in Fig. 2.7. The most common case is depicted in Fig. 2.7 (a), where by scanning the magnetic field we observe four pairs of peaks. We see them in pairs because we observe both m_s states and there are four pairs because the magnetic field is projected along the four different NV axes. Each axis sees a different magnetic field amplitude, resulting in different displacement of the peaks from the 2.87 GHz zero-field splitting, in the

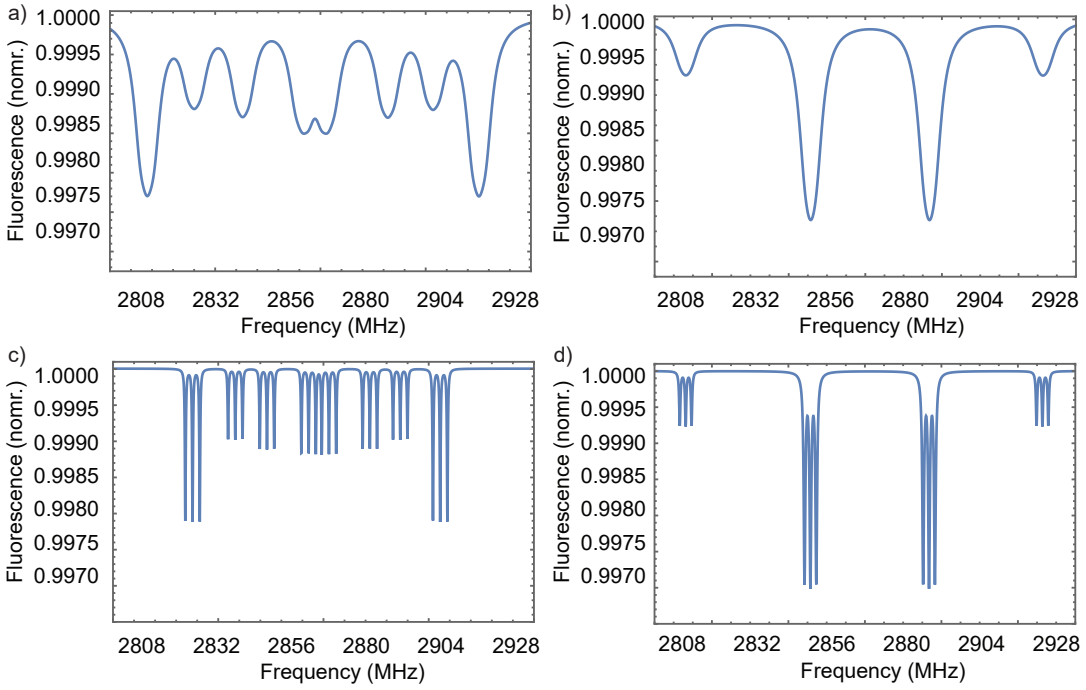

FIGURE 2.7: Different ODMR examples a) Broad resonance and arbitrary magnetic field ODMR, b) Broad resonance with magnetic field aligned along an NV axis, c) Narrow resonance and arbitrary magnetic field, d) Narrow resonance with magnetic field aligned along an NV axis. The data for the broad resonances are obtained with sample C7 and for the narrow resonance with sample S1. Information on which can be found in C.

most general case. The amplitude of the peaks should, in principle, be the same. In practice, we most often observe different amplitudes due to the projection of MW field along the NV axes, due to green light polarization related effects and in the case of CVD samples, due to preferentially oriented grown samples [84]. Once the ODMR spectrum is obtained, one can measure the frequency difference between the peak pairs Δf. Knowing that $\Delta f = \gamma_e |B|$ one can then calculate the DC magnetic field around the NV, and even reconstruct the vector magnetic field from measuring along the different axes, as described in Chapter 6. If the magnetic field is aligned with one NV axis then the projection of the magnetic field along the other three axes would be the same, and an image like Fig. 2.7 (b) and (d) would be obtained, where only two peak pairs, with roughly one-to-three amplitude ratio, are visible. Other special cases of magnetic field and NV axis alignment are discussed in Chapter 6.

The cases depicted in Fig. 2.7 (c) and (d), correspond to similar cases as (a) and (b) for a sample with a narrower ODMR linewidth. In this case the hyperfine

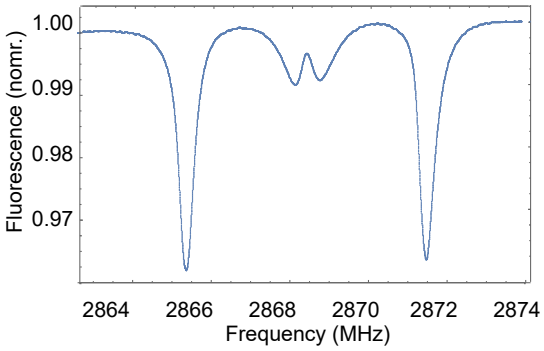

FIGURE 2.8: Zero field ODMR obtained with sample S1.

interaction with, most commonly, a ^{14}N nucleus, which is part of the NV center, results in splitting of the main peak into three (due to the ^{14}N nuclear spin 1). In the presence of ^{15}N the peak would split into two instead. The frequency difference between the hyperfine components is about 2 MHz.

It should be noted that in the absence of an external magnetic field and for the case of a narrow-linewidth sample, with ^{14}N hyper-fine interaction, four, instead of three peaks are visible, as seen in Fig. 2.8. The central feature of the hyperfine splitting is further split into two peaks due to stray electric field effects in the diamond. This electric field couples to the NV, lifting the degeneracy between the central $m_s = \pm 1$, ODMR peaks [81].

Finally, we note here that ODMR can also be done by probing the NV absorption of IR light, under illumination of green light and application of a MW field. Since, when the MW field is resonant with one of the $m_s = 0$ to $m_s = \pm 1$, population is transferred through the singlet states, whose zero-phonon line is at 1042 nm, resulting in higher absorption of IR light. This can be done to avoid the loss in sensitivity associated with collecting the fluorescence emitted by the diamond. A topic described in greater detail in Chapter 3.

§ 2.7 DC magnetometry

Using ODMR one can measure static or slowly-varying magnetic fields. Constructing a DC magnetometer one can measure magnetic fields with frequency components from DC up to the bandwidth (BW) of the magnetometer, which in the case of NV is up to a few MHz [27]. If a MW frequency is scanned across one of the ODMR features within a certain τ_{scan}, one can obtain the magnetic field value

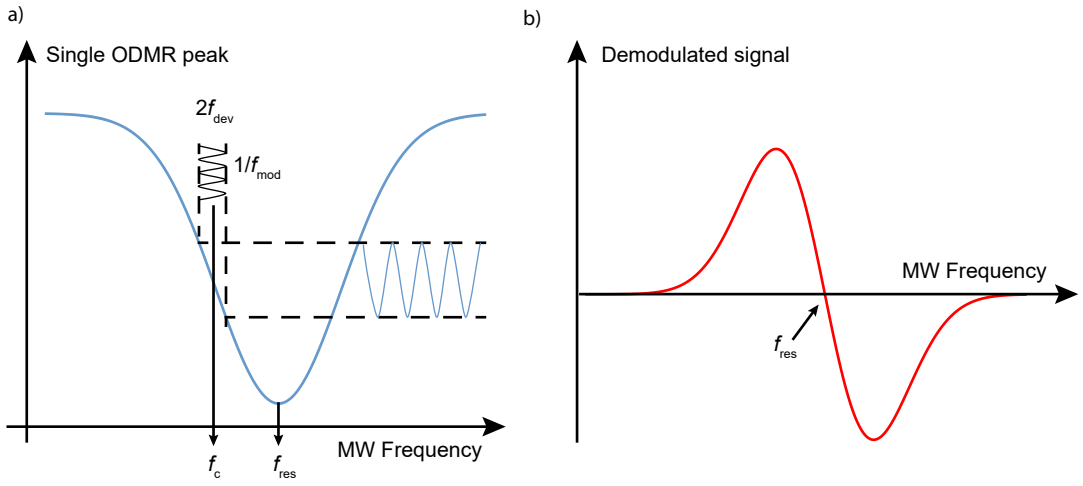

FIGURE 2.9: a) Single ODMR feature. The MW frequency is modulated at a frequency f_{mod} around a central value f_c with a certain frequency deviation f_{dev}. b) The demodulated signal has a dispersive lineshape when sweeping f_c. The slope at the zero-crossing gives a calibration factor from signal amplitude to magnet field.

during such a time interval, with a BW $\sim 1/\tau_{scan}$. The BW in that case would normally be limited by technical limitation e.g., the scan frequency of the MW generator used. Furthermore, this slow scan makes the magnetometer susceptible to low-frequency technical noise or drifts, such as moving magnetic objects, 50/60 Hz magnetic fields from the line voltage, power fluctuations of the pump laser, air turbulence around the system, etc. One way to reduce these kinds of noise is to move to a modulation technique with the use of a lock-in amplifier (LIA). For this procedure, most commonly, an external magnetic field is modulated, with the use of another coil [1] or a MW field is modulated, with a built-in frequency modulation (FM) option [26, 58], existing in most MW frequency generators. Since a MW coil is implemented on most NV magnetometry setups the FM technique is easily implemented and most commonly used.

An example of this modulation technique can be seen in Fig. 2.9. The MW frequency is modulated at a frequency f_{mod} around a central value f_c with a certain frequency deviation f_{dev}. f_c should be chosen to be close to the resonance frequency f_{res}, from $m_s = 0$ to $m_s = \pm 1$ of the $^3A_2$ triplet. The measured fluorescence signal is then demodulated by a LIA referenced at f_{mod}, resulting in a similar shape as the one seen in Fig. 2.9 (b). The demodulated signal will then have a zero-crossing at $f_c = f_{res}$, and will scale as $f_c - f_{res}$, if one remains within the magnetic resonance linewidth. To estimate the magnetic field sensitivity of the sensor or measure the magnetic field around the NV, one can acquire a time trace at $f_c = f_{res}$ while

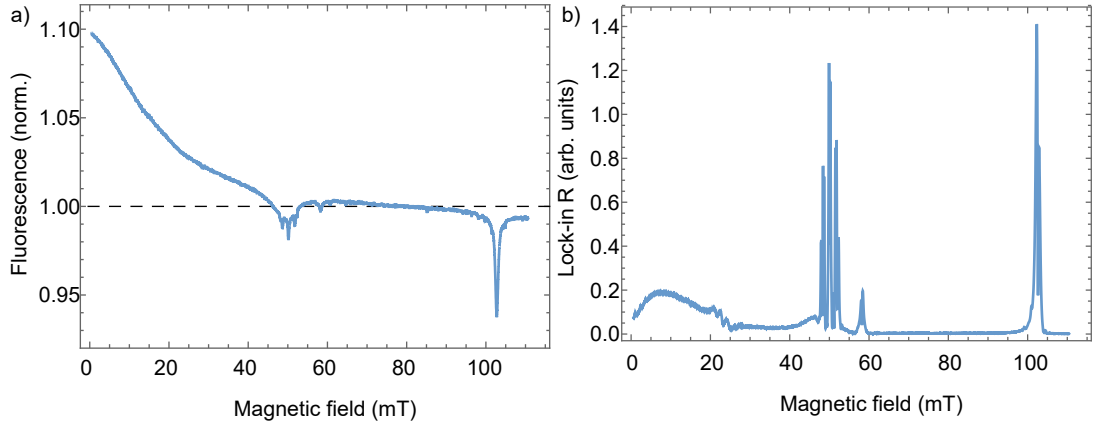

FIGURE 2.10: a) Normalized PL collected from NV centers as a function of magnetic field b) LIA R output for the same PL trace, obtained with the application of an oscillating magnetic field.

the MW is modulated and the LIA output is recorded. Once the time trace is acquired it can be Fourier transformed. This will provide the signal fluctuations per square root frequency of the sensor as a function of frequency. The slope around the zero-crossing of Fig. 2.9 (b) can be used as a calibration to translate this signal/$\sqrt{\text{Hz}}$ fluctuations to magnetic field/$\sqrt{\text{Hz}}$, if multiplied with the electron gyromagnetic ratio. In practice the BW of the sensor using this method will be limited by the combined low-pass filter response of the NV BW with the LIA measurement effective BW_{LIA}, which scales as $\text{BW}_{LIA} \sim 1/\tau_{LIA}$, if τ_{LIA} is the LIA time constant.

It should be noted here, that while the typical approach to magnetometry with NV centers includes the use of MW, their application is not necessary for magnetometry. One alternative approach includes the use of bias magnetic fields while monitoring the magnetic-field-dependent PL of the NV [27, 113]. When an external magnetic field is applied to the NV, various features appear as seen in Fig. 2.10. The features appearing during such a scan, can provide information on the environment surrounding the NV, such as nitrogen [N] and [NV] concentrations, as well as [^{13}C] [54]. The feature most commonly used for magnetometry is the one occurring at the ground-state level anti-crossing (GSLAC) of the NV, around 100 mT, but other features can also be used as discussed in Chapter 5. These features further depend on other experimentally controllable factors, which are discussed extensively in Chapter 4.

§ 2.8 Magnetic field sensitivity

While magnetic field sensitivity is not the main strength of NV-center magnetometers, NVs still remain very sensitive magnetic field sensors. The magnetic field sensitivity indicates the smallest change in magnetic field a sensor can detect normalized per unit of measurement BW, it is normally expressed in $\mathrm{T}/\sqrt{\mathrm{Hz}}$. This corresponds to an acquisition time, τ_m and should be correspondingly normalized for different time-acquisition windows.

If, for simplicity, we assume a magnetometer that has a 100 % duty cycle, and δB is the uncertainty on the measured magnetic field. If the measurement is repeated N times, then, for the case of uncorrelated noise, the uncertainty will decrease by $\sqrt{N}$, thus higher resolution in magnetic field can be achieved, but the sensitivity will remain the same, i.e. it does not depend on averaging.

The sensitivity of an NV magnetometer will be ultimately limited by certain quantum limits as mentioned in Chap. 1. The most fundamental of which is the spin-projection noise associated with the finite number of NV centers $\mathrm{N_{NV}} = n\,V$, where V is the interrogated diamond volume and n is the density of the spins. The spin-projection noise, δB_q, is given by Eq.1.1 and repeated here for convenience:

$$\delta\, B_q \;\approx\; \frac{1}{\gamma_e/_{2\pi}} \frac{1}{\sqrt{n V t_m T_2^*}}, \tag{2.4}$$

where T_2^* is the coherence time. It is worth noting that:

$$T_2^* \sim \frac{1}{\pi \Delta\nu} \tag{2.5}$$

where, $\Delta\nu$ is the linewidth of the ODMR feature discussed in Chapter 2.6. The spin-projection noise can only be surpassed if one uses quantum entanglement of the sensing spins, as the noise associated with spins afterwards becomes correlated [51].

Even though spin-projection is the fundamental limit, most of the best NV magnetometers [16, 26] end up being limited by photon-shot noise, δB_p, of the light collected to read out the NV spin state. The photon-shot noise is given by the following formula:

$$\delta B_p \approx \frac{1}{\gamma/_{2\pi}} \frac{\Delta\nu_{\mathrm{mr}}}{C\sqrt{\mathcal{R}}}, \tag{2.6}$$

where C is the contrast of the ODMR feature magnetometry is performed on, and R is the rate of collected photons.

Since the overall magnetometer signal, S, increases linearly the rate R and the uncertainty due to photon-shot noise increases only as $\Delta\mathrm{S} \sim \sqrt{R}$ the sensitivity improves as $\Delta\mathrm{S}/\mathrm{S} = 1/\sqrt{R}$.

Trying to compare the two different noise sources, we consider the following. If we denote the excitation rate on the triplet states as Γ_p, then for a standard NV experiment $\Gamma_p \sim 1/T_2^*$, as a higher rate will result in smaller coherence time and broader linewidths. If we can collect all the fluorescence produced by the NV then $R \sim N_{NV}/T_2$ and we can see Eq. 2.6 differs from Eq. 2.4 only by the contrast C. In practice C is much smaller than 100 % making photon-shot noise the first limit we encounter.

The most sensitive NV-based DC magnetometers as of the writing of this Thesis, are in the order of $10\,\mathrm{pT}/\sqrt{\mathrm{Hz}}$ [16, 26], even though there have been demonstrations of sub-pT sensitivities with the use of ferrite "flux concentrators" [44] or with AC magnetometry protocols [115].

§ 3

Miniature cavity-enhanced diamond magnetometer

§ 3.1 Abstract

We present a highly sensitive miniaturized cavity-enhanced room-temperature magnetic-field sensor based on nitrogen-vacancy (NV) centers in diamond. The magnetic resonance signal is detected by probing absorption on the 1042 nm spin-singlet transition. To improve the absorptive signal the diamond is placed in an optical resonator. The device has a magnetic-field sensitivity of $28\,\mathrm{pT}/\sqrt{\mathrm{Hz}}$, a projected photon shot-noise-limited sensitivity of $22\,\mathrm{pT}/\sqrt{\mathrm{Hz}}$ and an estimated quantum projection-noise-limited sensitivity of $0.43\,\mathrm{pT}/\sqrt{\mathrm{Hz}}$ with the sensing volume of $\sim 390\,\mu\mathrm{m} \times 4500\,\mu\mathrm{m}^2$. The presented miniaturized device is the basis for an endoscopic magnetic field sensor for biomedical applications.

§ 3.2 Introduction

Biomagnetic signatures are an important diagnostic tool to understand the underlying biological processes. Time-resolved biomagnetic signals are measured with Hall probes [71], Giant magnetoresistance sensors [13], alkali-vapor magnetometers [57], superconducting quantum interference devices (SQUIDs) [107] and single negatively-charged nitrogen-vacancy (NV) centers or ensembles thereof [16]. Typical devices probe magnetic fields outside the body, i.e., far from their origin. However, signal strength and spatial resolution can both be improved by utilizing

endoscopic sensors. The most sensitive from the above magnetometers are based on SQUIDs and alkali-vapor cells, but neither is ideal for biological applications. NV centers in diamond have already been used as nanoscale-resolution sensors [12,77,91] with high sensitivity [16,115]. Prominent examples of sensing with NV centers include, single neuron-action potential detection [16], single protein spectroscopy [69], as well as in vivo thermometry [61]. Due to their ability to operate in a wide temperature range as well as their small size, NV magnetometers are amenable for in-vivo and/or endoscopic applications.

The majority of NV sensors use a photoluminescence (PL) detection which suffers from low photon-detection efficiency. Approaches to counter this problem include, for example, the use of solid immersion lenses [49,63,101], or employ infrared (IR) absorption [1,41,58]. Compared to NV sensors based on PL detection, those based on absorption feature collection efficiency approaching unity [1].

Due to the small cross-section of the IR transition [1, 41], to achieve similar or higher sensitivities compared to PL-detection techniques, we use an optical cavity to enhance the optical pathlength in the diamond, and thus the IR absorption signal [41,58]. With the cavity enhancement we can achieve sensitivities closer to the fundamental projection-noise limit, even at room temperature [41,58].

Here we demonstrate a sensitive compact cavity-based IR absorption device operating near the photon shot-noise limit opening realistic prospects for a practical endoscopic magnetometer. The best DC magnetometer using NV centers, in a sensing volume of $13 \times 200 \times 2000$ μm^3, have reached magnetic field sensitivity of $15(1)\,pT/\sqrt{Hz}$ (Ref. 16). Our sensor features a similar sensing volume and sufficient sensitivity to measure biomagnetic signals e.g. magnetic signals by the human heart.

§ 3.3 Experiment

The ground and excited electronic spin-triplet states of NV are $^3A_2$ and ^3E, respectively [Fig. 3.1 (a)], with the transition between them having a zero-phonon line at 637 nm. The lower and upper electronic singlet states are ^1E and $^1A_1$, respectively, with the transition between them having a zero-phonon line at 1042 nm (IR). While optical transition rates are spin-independent, the probability of non-radiative intersystem crossing from ^3E to the singlets is several times higher [41] for $m_s = \pm 1$ than that for $m_s = 0$. As a consequence, under continuous illumination with green pump light (532 nm), NV centers are prepared in the $^3A_2$ $m_s = 0$

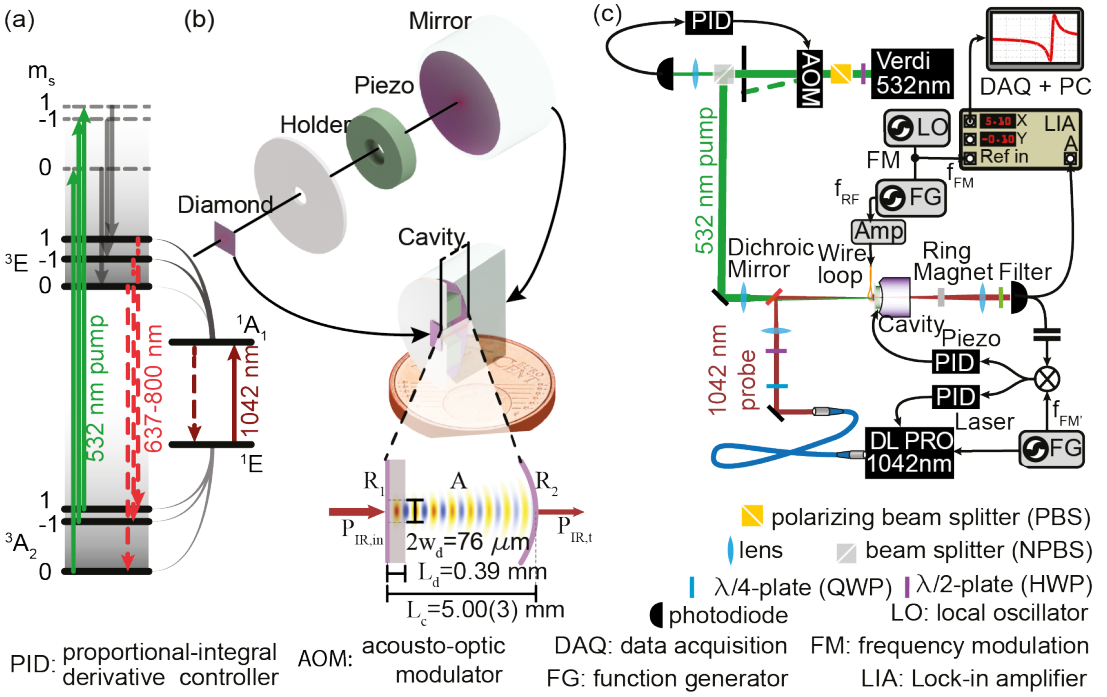

FIGURE 3.1: (a) Relevant NV center energy levels and transitions (Ref. 5). Solid green and red lines indicate excitations, dashed lines indicate radiative transitions, and gray solid lines indicate non-radiative transitions. (b) Explosion view and 2D cross section of the cavity magnetometer (c) Schematic of the experimental setup.

ground state sublevel and in the metastable ^{1}E singlet state. For metrology applications, the spins in the the $^3A_2$ ground state can be coherently manipulated by microwave fields. In this work, the population of the ground state is infrared by monitoring IR light absorption on the singlet transition.
The diamond sample used for this sensor is a type Ib, (111)-cut, HPHT grown sample, purchased from Element Six. The initial nitrogen concentration of the sample was specified as < 100 ppm, which seems consistent with linewidth measurements. The sample was irradiated with 5 MeV electrons and dosage of 2×10^{19} cm^{-2} and then annealed at 700 ^{o}C for 2 hours.

To increase the absorption of IR light we construct a cavity as shown in Fig. 3.1 (b). A spherical mirror with a curvature radius of 10 mm, reflectivity $R_2 = 99.2(8)\%$ (see supplemental material 3.7) and diameter of 12.5 mm serves as the output mirror. A piezoelectric transducer is used to adjust the length of the cavity within a range of a few µm. It is glued with an epoxy resin (Torr Seal) between the spherical mirror and the ceramic holder for the diamond. The diamond plate serves as the input plane mirror of the cavity and is glued to the holder. The holder doubles

as a heat sink. The (111)-cut diamond plate is dielectrically coated with high reflective (HR) coating $R_1 \sim 98.5\%$ for IR light as well as anti-reflective (AR) for green light on the outside of the cavity. The diamond surface inside the cavity is supplied with an anti-reflective coating for both green light and IR light. The reflectivity of the coatings for both, the diamond and the output mirror, were chosen according to the losses in the diamond. The total optical length of the cavity is $L_c = 5.00(3)$ mm, and the finesse is $\mathcal{F} = 160(4)$ (see supplemental material 3.7). The cavity mode has a waist on the diamond with a radius of $w_d = 38\,\mu$m; the mode radius is 54 µm on the concave mirror surface. With this design, it is possible to bring the diamond's outer surface in close proximity to a magnetic sample under study in compact geometry. Currently, the diameter of our sensor is 12.5 mm with a total length of ~ 8 mm. For comparison, some modern medical endoscopes feature comparable outer diameters (Olympus, GIF-2TH180, 12.6 mm)."
The setup for magnetometric measurements is shown in Fig. 3.1 (c). Green light is provided by a diode-pumped solid-state laser (Coherent, Verdi V10) and IR light is provided by an external-cavity diode laser (ECDL, Toptica DL-Pro). The green laser power is stabilized using an acousto-optical modulator (AOM, ISOMET-1260C with an ISOMET 630C-350 driver) controlled through a proportional-integral-derivative controller (PID, SIM960). The IR beam profile is matched to the lowest-order transversal cavity mode (TEM_{00}), while the green beam is overlapped with the IR beam in the diamond; the green beam profile does not have to be mode matched to the cavity but it should be bigger than the IR profile to provide a homogeneous pumping rate of the interrogated NV centers. The frequency difference of the laser and the cavity mode is stabilized using an error signal derived by frequency modulation of the laser ($f_{FM'}$=2.4 MHz). Two PIDs are deployed for the feedback. One to lock the cavity piezo to the laser (bandwidth 6 kHz) and the other to provide feedback to the laser controller. The latter addresses piezo and current of the ECDL and has a bandwidth of 21 kHz.
The microwaves (MW) to manipulate the NV spins are generated by a MW generator (SRS SG394). They are amplified with a 16 W amplifier (ZHL-16W-43+), passed through a circulator (CS-3.000, not shown in Fig.1) and high-pass filtered (Mini Circuits VHP-9R5), before they are applied to the NV centers using a mm-sized wire loop. The other side of the wire is directly connected to ground. A bias magnetic field is applied with a permanent ring magnet mounted on a precision positioning stage.

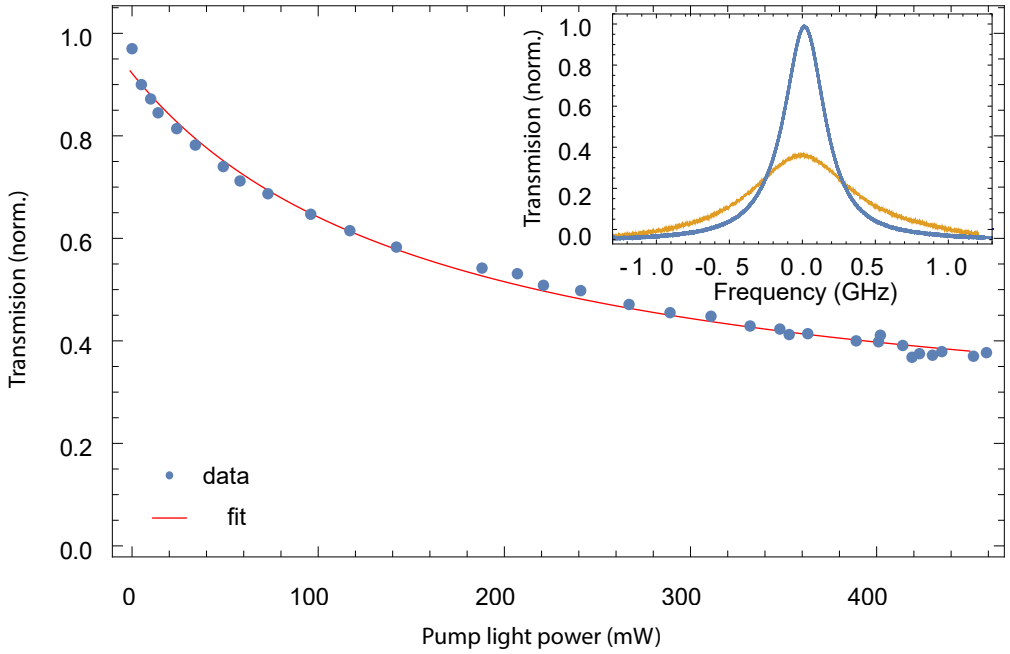

FIGURE 3.2: IR light transmission of the cavity ($P_{IR,t}$ as a function of green pump power (P_{532}). The transmission is normalized to unity for zero pump power. The inset displays the TEM_{00} cavity mode at 0 mW (blue) and 500 mW of pump light power (amber) .

§ 3.4 Results and discussion

The cavity transmission signal $P_{IR,t}$ for IR light is shown in Fig. 3.2 as a function of green light power P_{532} in front of the cavity. The steady-state population of the singlet state increases with increasing green power, resulting in higher IR absorption. The IR absorption is enhanced by the cavity by $2\mathcal{F}/\pi$, yielding significantly reduced IR transmission for higher pump powers. Higher absorption also results in an increase of the cavity-mode linewidth (Fig. 3.2, inset). The data in Fig. 3.2 are fitted with a saturation curve $P_{IR,t}(P_{532})/P_{IR,t}(P_{532} = 0) = 1 - \alpha P_{532}/(P_{532} + P_{532,sat})$ (Ref. 58), with saturation power $P_{532,sat}$ and reduction in transmission at saturation α. The fit results are $P_{532,sat} = 735(1)$ mW and $\alpha = 0.605(1)$. Magnetic-resonance measurements (Fig. 3.3) are performed by scanning the MW frequency around the NV zero-field splitting (2.87 GHz). When the MW field is resonant with the ground-state $m_s = 0 \rightarrow m_s = \pm 1$ transitions, population is transferred through the exited triplet state to the metastable singlet state, resulting in increased IR absorption, which produces the observed optically detected magnetic resonance (ODMR) signal.

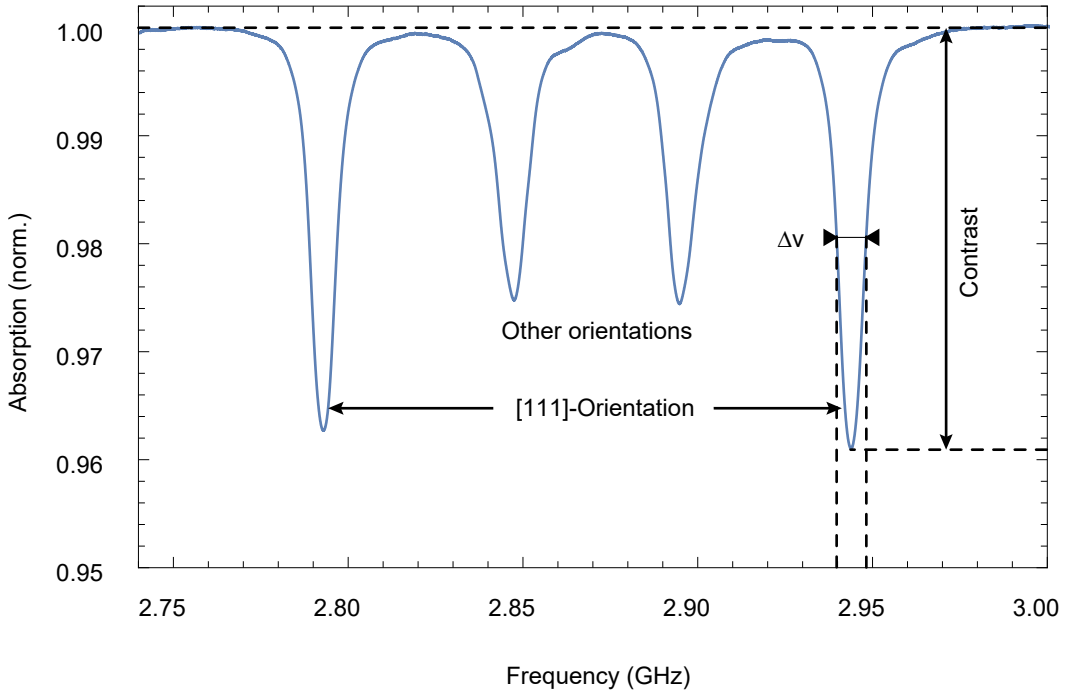

FIGURE 3.3: IR transmission signal normalized to unity off resonance as a function of microwave frequency.

With a bias magnetic field (in this case, about 3 mT) aligned along the [111] axis, four peaks are visible by scanning the MW frequency (Fig. 3.3). The outer features result from the NVs along the [111] axis and the inner features from the remaining NV orientations. The relative amplitudes of ODMR peaks depend on several things, such as, polarization of MWs, IR light polarization and green light polarization. It will also depend on how well the magnetic field is aligned, as if it is not perfectly along [111]-direction, the innermost peaks will broaden and have reduced amplitude The contrast $\mathcal{C}$ and the full width at half maximum $\Delta\nu$ of the outer peaks are $\sim 3.7\,\%$ and 5.6 MHz, respectively.

For the magnetometric measurements we focus on the highest frequency feature in Fig. 3.3. We modulate the MW frequency f_{MW} around the central frequency f_{c} of the feature with frequency $f_{\mathrm{mod}} = 8.6\,\mathrm{kHz}$ and amplitude $f_{\mathrm{dev}} = 4.5\,\mathrm{MHz}$: $f_{\mathrm{MW}} = f_{\mathrm{c}} + f_{\mathrm{dev}}\cos(2\pi f_{\mathrm{mod}} t)$ and detect the first harmonic of the transmission signal with a lock-in amplifier (LIA). These values were chosen to optimize the sensor's noise floor in the laboratory environment. Fig. 3.4 shows the resulting dispersive signal centered at the feature (red) along with the feature itself (blue). Around the zero-crossing of the dispersive feature, we observe a linear signal $S_{\mathrm{LI}} \sim a(f_{\mathrm{c}} - f_{\mathrm{res}})$ as a function of $(f_{\mathrm{c}} - f_{\mathrm{res}})$ when $|f_{\mathrm{c}} - f_{\mathrm{res}}| << \Delta\nu/2$. We extract the slope $a \propto \mathcal{C}/\Delta\nu$ from the fit of Fig. 3.4 (black) and use it to convert

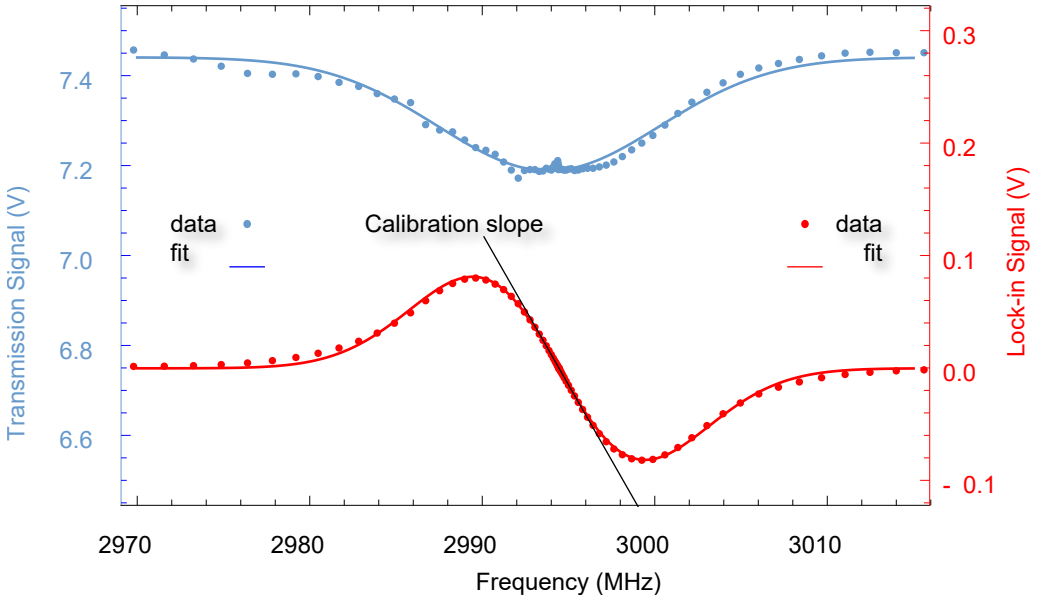

FIGURE 3.4: The cavity-transmission signal (blue) and lock-in demodulated signal (red) as a function of a central frequency f_c scanned over a magnetic resonance. The experimental data are represented with dots and the fits with solid lines. The slope of the fit is represented with a straight line.

the magnetometer's voltage output into magnetic field.

Figure 3.5 shows the magnetic-field-noise spectrum. The spectrum was obtained by a Fourier transform of the LIA output with a reference frequency of 8.6 kHz. The peaks at 50 Hz and harmonics are attributed to magnetic field from the power line in the lab and are not visible on the magnetically insensitive spectrum, which we obtain in the absence of a MW field. The noise floor in the region of 60-90 Hz for the magnetically insensitive spectrum is calculated as $28\,\mathrm{pT}/\sqrt{\mathrm{Hz}}$. The above measurements where obtained at 400 mW of pump light and 80 mW of IR which was the maximum available for our system.

This sensitivity is ≈ 100 times better than what has been demonstrated previously with magnetometers based on IR absorption [58]. The photon-shot-noise limited sensitivity of the two sensors is comparable ($70\,\mathrm{pT}/\sqrt{\mathrm{Hz}}$ against $22\,\mathrm{pT}/\sqrt{\mathrm{Hz}}$) using similar sensing volumes, while the length of the cavity was reduced by an order of magnitude. Main improvements that aided in the increased sensitivity are: a dramatic reduction in cavity size, increase in probe laser power and improvements to the laser-lock stability. The size reduction translates to robustness in frequency noise of the laser. The increase in IR light power allowed us to surpass the shot-noise-limit of the previous design. While with improvements to the laser-lock stability we were able to optimize the sensor's noise-floor in regards to the noise of

the laboratory. We verify the sensitivity by applying test magnetic fields (seen supplemental material 3.7). The photon shot noise limit is estimated as $22\,\mathrm{pT}/\sqrt{\mathrm{Hz}}$ for 4.2 mW of collected IR light. The electronic shot noise is $2\,\mathrm{pT}/\sqrt{\mathrm{Hz}}$. For an estimated NV density in the metastable singlet state of 0.68(1) ppm (see supplemental material 3.7) and the demonstrated ODMR linewidth $\Delta\nu = 5.6\,\mathrm{MHz}$ we calculate a spin-projection noise limit of $0.43\,\mathrm{pT}/\sqrt{\mathrm{Hz}}$. The bandwidth of the magnetometer is set by the LIA filter settings. For the presented measurements a time constant of 300 µs results in a 530 Hz bandwidth. The filter steepness is selected as 24dB/octave.

§ 3.5 Discussion

We demonstrate a miniaturized cavity-enhanced room-temperature absorption-based magnetometer using NV centers in diamond. The small size of the magnetometer yields a robust device with improved magnetic field sensitivity and makes it an ideal candidate for endoscopic measurements. The closer proximity to biomagnetic signal sources, inherent to endoscopic measurements, provides enhanced signal strength and spatial resolution, which may be further improved by using a combination of a different diamond with narrower ODMR feature linewidth and a higher finesse cavity. To realize the endoscopic sensor design the following changes must be made; The diamond should act as the output mirror of the cavity, an all optical protocol has to implemented, the two different light beams should be delivered by an optical fiber and smaller components (e.g. mirror) have to used when possible. With the diamond acting as the output mirror we would have better access to the surface of the diamond sensor, the sensor would then detect the signal on reflection rather than transmission allowing samples to be placed close to the diamond plate without blocking any of the light sources. An all optical protocol as in Ref. 119 would allow us to avoid the usage of MW which could be detrimental for biomedical applications. If we deliver the light beams with an optical fiber we could reduce the need for extra optical components and reduce the footprint of our sensor. Smaller components, such as a smaller mirror and diamond, should also be used in the next design for the same purpose.

Our sensor features a noise-floor of $28\,\mathrm{pT}/\sqrt{\mathrm{Hz}}$ close to the shot-noise limit (see supplemental material 3.7). The sensitivity may be improved in future iterations by increasing the IR light power [4], optimizing the impedance matching condition of the cavity [41] to provide higher contrast, implementing AC sensing protocols

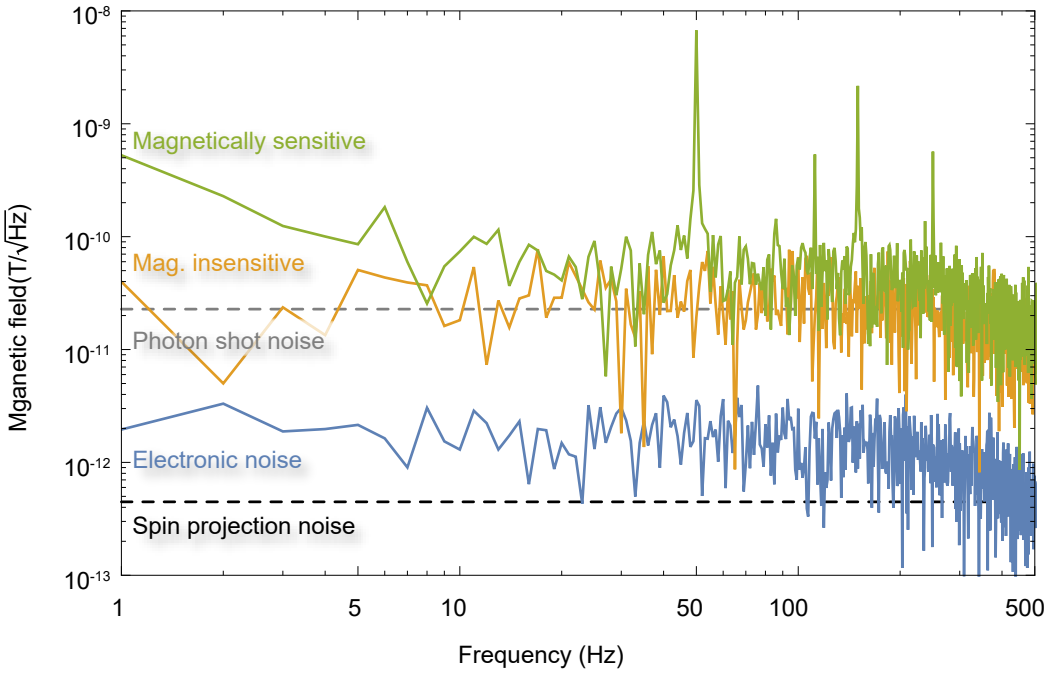

FIGURE 3.5: Magnetic-field noise spectrum (green) represents the magnetically sensitive spectrum corresponding to a environment limited noise floor of $37\,\mathrm{pT}/\sqrt{\mathrm{Hz}}$ between 60 and 90 Hz, (amber) the magnetically insensitive with a noise floor of $28\,\mathrm{pT}/\sqrt{\mathrm{Hz}}$ and (blue) the electronic noise with a floor of $2\,\mathrm{pT}/\sqrt{\mathrm{Hz}}$. The shot noise limit of the system and the spin projection noise are also depicted with a dashed lines at $22\,\mathrm{pT}/\sqrt{\mathrm{Hz}}$ and $0.43\,\mathrm{pT}/\sqrt{\mathrm{Hz}}$, respectively.

that allow increased NV coherence times due to dynamic decoupling from the decoherence sources [43], and using a diamond sample with narrower linewidth which would increase the calibration slope obtained by the calculation of Fig. 3.4.

§ 3.6 Acknowledgements

The authors acknowledge support by the German Federal Ministry of Education and Research (BMBF) within the Quantumtechnologien program (FKZ 13N14439) and the DFG through the DIP program (FO 703/2-1). GC acknowledges support by the internal funding of JGU. NL acknowledges support from a Marie Curie International Incoming Fellowship within the 7th European Community Framework Programme. LB is supported by a Marie Curie Individual Fellowship within the second Horizon 2020 Work Programme. DB acknowledges support from the

AFOSR/DARPA QuASAR program. We thank J.W. Blanchard for a fruitful discussion.

§ 3.7 Supplemental material to: Miniature cavity-enhanced diamondmagnetometer

§ 3.7.1 NV singlet state population

We can calculate the NV state population from the increase in cavity losses under saturating green pump light. The losses are related to the measurable quantities finesse ($\mathcal{F}$) and the cavity's IR light transmission on resonance to initial IR light ratio ($\frac{I_{\mathrm{tr}}}{I_{\mathrm{in}}}$). Measuring the losses with (A_2) and without (A_1) green pump light allows us to infer the losses due to NVs in the singlet state (A_{NV}). Finally, the increase in losses per roundtrip can be related to the NVs singlet population by the Beer-Lambert law. Assuming ideal loss-free mirrors finesse and transmission are given by:

$$\left(\frac{2\mathcal{F}}{\pi}\right)^2 = \frac{4\sqrt{R_1R_2(1-A)}}{(1-\sqrt{R_1R_2(1-A)})^2}, \tag{3.1}$$

$$\frac{I_{\mathrm{tr}}}{I_{\mathrm{in}}} = \frac{4(1-R_1)(1-R_2)(1-A)}{(2-R_1-R_2+A)^2}, \tag{3.2}$$

where R_1 the reflectivity of the diamond coating, R_2 is the reflectivity of the output mirror and A represents the losses per roundtrip due to the diamond crystal.
According to the company specification, $R_1 = 98.5(5)\%$. R_2 and A_1 can be inferred solving Eq. (S1-S2) with measurements of finesse and transmission. Without green pump light we determine $R_2 = 99.2(8)\%$ and $A_2 = 1.66(1)\%$. Assuming the same reflectivity and adding saturating green pump light we get a new value for losses $A_2 = 3.09(3)\%$. The difference in losses $\Delta A = A_{\mathrm{NV}}$ can be attributed to absorption on the singlet transition. These losses can be related to NV population in the singlet state via the Beer-Lambert law. The transmission of the diamond for losses A_{NV} is given by:

$$1 - A_{\mathrm{NV}} = e^{-n\sigma l}, \tag{3.3}$$

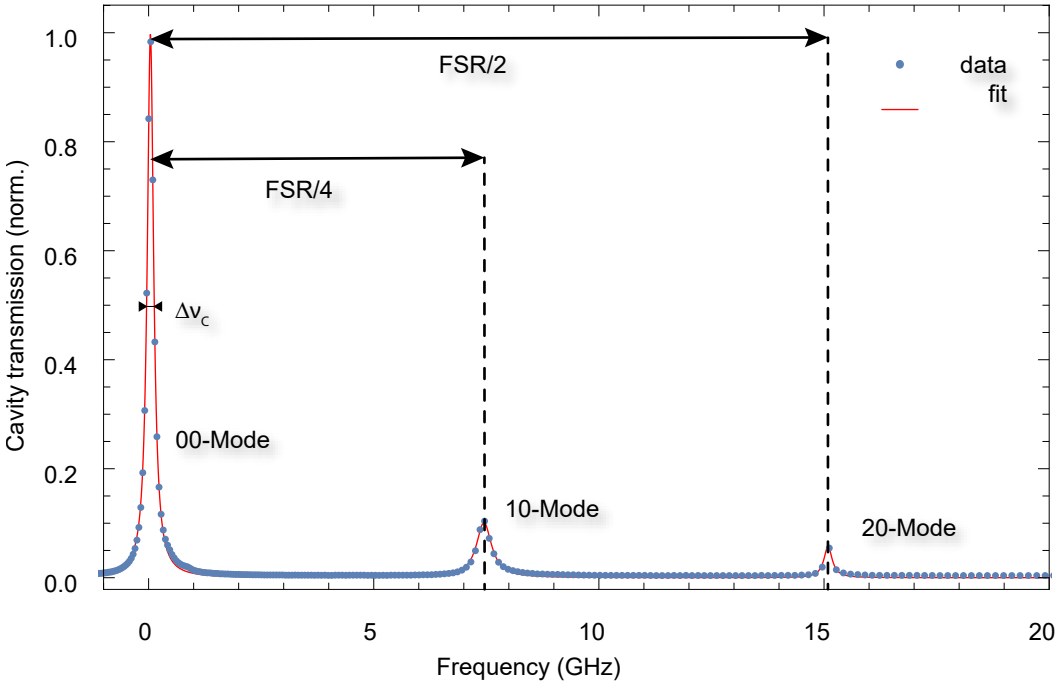

FIGURE 3.6: IR transmission spectrum of the cavity obtained by scanning the cavity length, in the absence of green light. Data are represented with dots (blue) and the fit with a line (red).

Where n is the density of the NVs in the singlet state, σ the absorption cross section of IR light on resonant with the singlet transition and l the path length in the diamond. With a path length $l = 2L_\mathrm{d}$ (where L_d= 0.39 mm is the geometric length diamond) and $\sigma = 3 \times 10^{-18}\,\mathrm{cm}^2$ (Ref. [41]) we calculate the density of NVs in the metastable state as $n = 0.68(1)$ ppm.

§ 3.7.2 Cavity finesse

Figure 3.6 shows the transmission of IR light while scanning the length of the cavity. From our measurements, after fitting we estimate the finesse ($\mathcal{F}$) of our cavity to be $\mathcal{F} = 160(4)$ [the FSR of the cavity is $\sim 30.1(2)$ GHz]. The finesse is measured in the absence of green pump light.

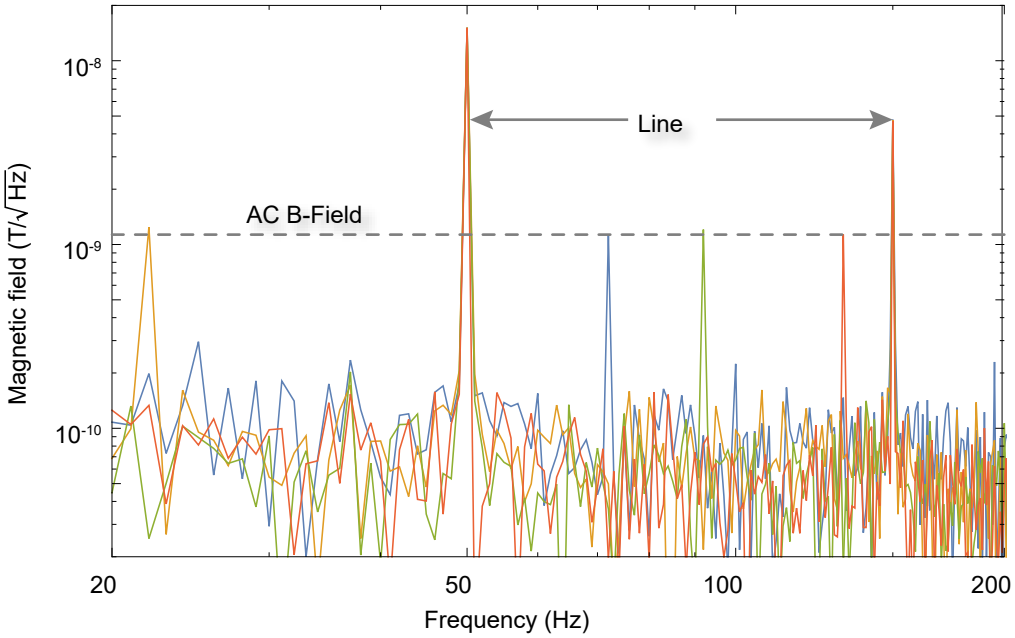

FIGURE 3.7: Magnetic-field noise spectrum for different fields as a function of frequency. The test field is applied for different frequencies of 22 Hz (amber), 72 Hz (blue), 92 Hz (green) and 132 Hz (red).

§ 3.7.3 Magnetometer Calibration

The sensitivity of the sensor is verified by applying external magnetic fields of a given amplitude and frequency to it. Fig. 3.7 shows the noise spectrum of the magnetometer in response to a sine-wave-modulated magnetic field of 1 nT RMS amplitude, at different frequencies.

The field is provided by a multi-turn circular current coil. The radius of the coil is r_{coil} ~2.5 cm and its distance from the sensor is z_{coil} ~1 cm. The coil is connected in series with a 1 kΩ resistor to decrease induction induced current. The amplitude of the produced magnetic field B_{test} is then compared with the recorded magnetometer signal B_{rec}. B_{test} can be calculated as:

$$B_{test} = \frac{\mu_0 N_{turns} I_{coil} r_{coil}^2}{2[z_{coil}^2 + r_{coil}^2]^{3/2}}, \tag{3.4}$$

where $\mu_0 = 4\pi \times 10^{-7}$ N/A^2 is the vacuum permeability, $N_{turns} = 11$ are the number of turns of the coil and $I_{coil} = 6.5$ µA the current flowing through the coil. Our measured B_{rec} is consistent with B_{test} within a 2% error.

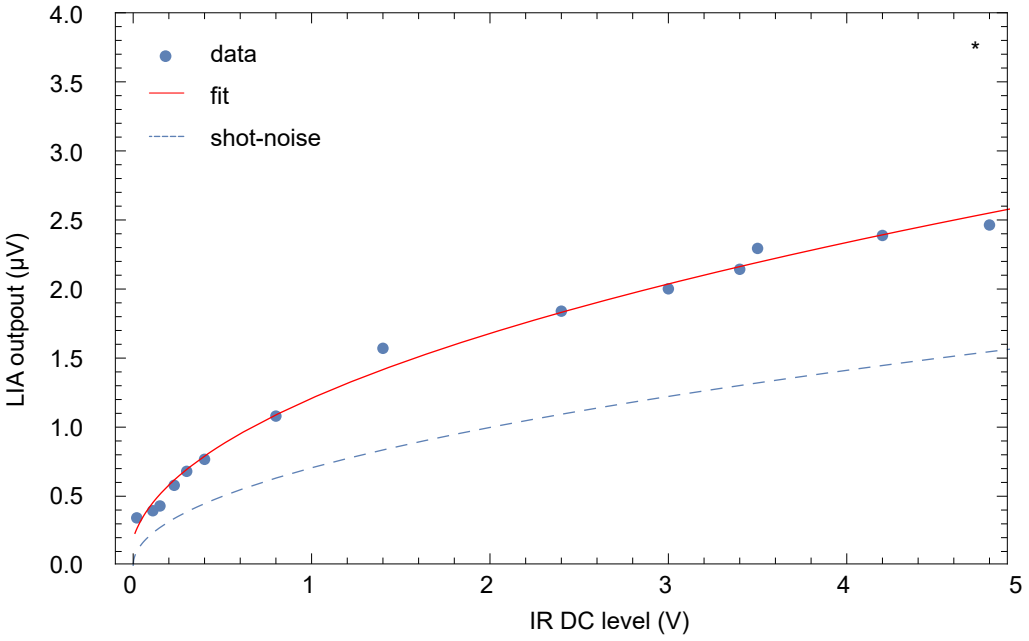

FIGURE 3.8: Measured and calculated RMS noise of cavity transmission. Data show in dots (blue), are fitted with a line (red) . Theoretical calculation for the shot noise is presented with dashed lines and an asterix symbol (*) is placed to signify the noise level under normal operation.

§ 3.7.4 Photon shot-noise behavior

To confirm the photon shot noise behavior of our sensor, in the absence of MWs, we record the output of the LIA (S_{IR}) as we detect transmission ($P_{\mathrm{IR,t}}$) for a wide range of IR light powers. We then fit the data with a curve S_{IR}. Where $S_{\mathrm{IR}} = \sqrt{a^2 + b^2 P_{\mathrm{IR,t}} + c^2 P_{\mathrm{IR,t}}^2}$, where a signifies laser power independent noise sources (e.g. electronic noise), b relates to IR light shot-noise and c to IR intensity noise sources.

Figure 3.8 shows the above measurements in dots (blue) at 100 mW of green light. The data is fitted (red) giving fit values $a = 0.23(8)$, $b = 1.16(6)$ and $c = 2\times10^{-3}(2)$ which indicates shot-noise dominated behavior for IR DC levels above ~ 0.2 V. The theoretically calculated shot noise is represented by the dashed line. Finally, the asterisk (*) is placed in Fig. 3.8 to signify the average noise floor between 60-90 Hz under normal operation corresponding to 400 mW of green pump light and a MW field applied to the NVs. The noise floor thus includes environmental and MW-related noise.

§ 3.8 Author contribution

For the work presented in this chapter, I build upon the idea conceived by Prof. D. Budker and the other co-authors in Ref. [58]. I performed calculations to optimize and constructed the cavity needed for the experiment. I created programs to interact with experimental equipment. I improved the sensitivity of the sensor, by investigating different noise sources, performed the experiment and acquired the data. With the help of Dr. A. Wickenbrock, I constructed the figures and with the help of the rest of the co-authors, I co-wrote the manuscript.

§ 4

Level anti-crossing magnetometry with color centers in diamond

§ 4.1 Abstract

Recent developments in magnetic field sensing with negatively charged nitrogen-vacancy centers in diamond employ magnetic-field dependent features in the photoluminescence and eliminate the need for microwaves. Here, we study two approaches towards improving the magnetometric sensitivity using the ground-state level anti-crossing feature of the nitrogen-vacancy center at a background magnetic field of 102.4 mT. Following the first approach, we investigate the feature parameters for precise alignment in a dilute diamond sample; the second approach extends the sensing protocol into absorption via detection of the ground-state level anti-crossing in the diamond transmission of a 1042 nm laser beam. This leads to an increase of ground-state level anti-crossing contrast and results in a magnetometer with a sensitivity of $0.45\,\mathrm{nT}/\sqrt{\mathrm{Hz}}$ and a photon shot-noise limited sensitivity of $12.2\,\mathrm{pT}/\sqrt{\mathrm{Hz}}$.

§ 4.2 Introduction

Magnetic-field (MF) sensing is of importance in many applications in fundamental physics, biology, and materials science. Using the negatively-charged nitrogen-vacancy (NV) center in diamond is attractive due to its high magnetic sensitivity at ambient conditions for a given sensing volume [12,47,62,77,95]. Diamond-based

magnetic sensors are realized via measurements of the NV center's magnetically sensitive ground state, commonly by using optically detected magnetic resonance (ODMR) techniques [95, 106, 109, 115]. ODMR sensing protocols predominantly involve the use of green pump light for NV-center spin polarization, application of microwave (MW) fields for spin manipulation, and an optical readout step involving either detection of the photoluminescence (PL) of the NV triplet state or absorption on the singlet transition at 1042 nm [Fig. 4.1 (a)]. However, there are applications, e.g., nano-magnetic resonance imaging [7], eddy current detection [35, 111] and MF mapping of conductive, magnetic structures [100] where the use of strong, continuous wave (cw) or pulsed, MW fields employed in MW-based ODMR is intolerable.

Recently, we demonstrated a novel MW-free magnetometric protocol based on the properties of the NV-center's ground-state level anti-crossing (GSLAC) [113]. Applying a ∼102.4 mT background MF causes an avoided crossing between two of the ground-state NV Zeeman-sublevels, resulting in spin-population transfer observable in changes of the NV-PL or 1042 nm absorption. The resulting MF-dependent feature can be used for sensitive magnetometry [7, 113, 117].

In this work, we explore two distinct avenues towards improved magnetometric sensitivities using the MW-free sensing protocol. We investigate the GSLAC lineshape as a function of nitrogen concentration, [N], and MF alignment, and, for the first time, we implement a magnetometer based on the GSLAC feature in absorption on the singlet transition $^1\mathrm{E} \rightarrow {}^3\mathrm{A}_2$ [Fig. 4.1(a)]. Additionally, we compare our recently published results [113] to a comparable diamond in a highly homogeneous magnet in Riga, to exclude MF gradient-related broadening.

§ 4.3 Experimental setups

The experiments where conducted on three different setups, two in Mainz and one in Riga.

A combined schematic of the experimental setups in Mainz is shown in Fig. 4.1(b); the first one is fluorescence-based and allows us to perform measurements on different samples with complete and precise control over all degrees of freedom in alignment, while the other one is an absorption-based magnetometer. In both setups, the NV centers in the diamond samples are optically spin-polarized with power-stabilized 532 nm light provided by a diode-pumped solid-state laser (Coherent

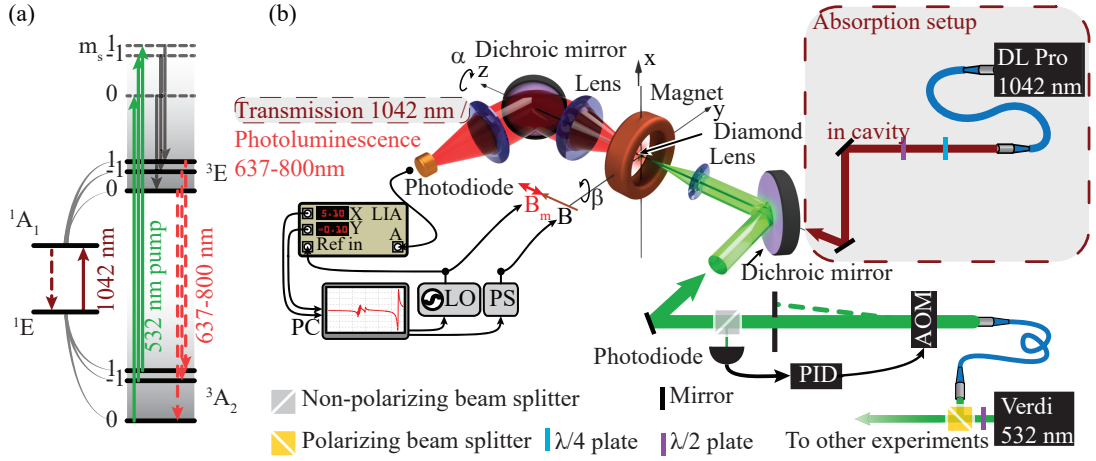

FIGURE 4.1: (a) NV-center energy level schematic. Solid green and red lines indicate excitations, dashed lines indicate radiative transitions, and gray solid lines indicate non-radiative transitions. (b) Schematic of the experimental setup. AOM: acousto-optic modulator, PID: proportional-integral-derivative controller, LIA: lock-in amplifier, LO: local oscillator, PS: power supply.

Verdi V10). Details of the optical and electrical components in the fluorescence-detection setup can be found in Ref. [113]. In the absorption-detection setup, 1042 nm light used to probe the singlet transition is delivered by a fiber-coupled extended-cavity diode laser (Toptica DL Pro) and locked to an optical cavity, which consists of the diamond sample with appropriate coating on either side and a spherical mirror. The absorption-magnetometry method and the setup are based on an improved version of a recently demonstrated cavity-enhanced NV magnetometer [41] and a more detailed description of the current experimental improvements is presented in Ref. [26].

The diamond samples in both setups are placed within custom-made electromagnets of the same build. They have 200 turns in a 1.3 cm thick coil with a 5 cm bore, are wound on a water-cooled copper mount, and produce a background field, B, of 2.9 mT per ampere supplied. For a field of 120 mT, approximately 1.8 kW are dissipated. The current is provided by a computer-controlled power supply (Keysight N8737A).

In the fluorescence-detection setup the diamond can be rotated also around the z-axis [Fig. 4.1(b); angle α]. Moreover, the electromagnet can be moved with a computer-controlled 3D translation stage (Thorlabs PT3-Z8) and a rotation stage (Thorlabs NR360S, x-axis) [Fig. 4.1(b); angle β]. Therefore, in this setup, all degrees of freedom for placing the diamond in the center of the magnet and aligning the NV axis parallel to the MF can be addressed with high precision.

In the absorption-based setup, the electromagnet is mounted on a manual 3D translation stage. An additional secondary coil (15 turns, gauge 22 wire, inner diameter of 12.5 mm) is used to apply a small MF modulation, B_m, to the background field that allows for phase sensitive detection for magnetometric measurements. Its current is supplied by a function generator (Tektronix AFG2021), which acts also as the local oscillator (LO) for a lock-in amplifier (LIA; SRS 865).
The fluorescence-detection setup in Riga employed a custom-built magnet initially designed for electron paramagnetic resonance (EPR) experiments. It consists of two 19 cm diameter iron poles with a length of 13 cm each, separated by a 5.5 cm air gap. This magnet could provide a highly homogeneous field. The diamond sample under investigation is held in place using a non-magnetic holder, allowing also for alignment of the NV axis to the applied MF. Green 532 nm light (Coherent Verdi) is delivered to the sample via 400 µm diameter core optical fiber (numerical aperture of 0.39). The same fiber is used for PL collection, which is separated from the residual green reflections by a long-pass filter (Thorlabs FEL0600) and focused onto an amplified photodiode (Thorlabs PDA36A-EC). The signals are recorded and averaged on a digital oscilloscope (Agilent DSO5014A).
Finally, in Table 4.1 we present the characteristics of all the diamond samples used in this work. We note here, that the measurements using diamond sample F11 were previously reported in Ref. [113]. The sample was initially built into the PL-detection setup in Mainz, and for this work we replaced it with a more dilute sample W4. In addition, for the PL-detection measurements performed in Riga, we used sample C7. In the absorption-detection setup we used the sample B3A, which has dielectric coatings on both sides. In particular, one side of the B3A diamond has a highly reflective (98.5%) coating while the other side has an anti-reflective coating for 1042 nm. This way, with an additional spherical mirror, the optical cavity to enhance the absorption on the singlet transition is formed [26].

§ 4.4 Results and discussion

Here we present a systematic investigation of relevant parameters in level anti-crossing magnetometry with NV centers towards highly sensitive MF measurements. For a level anti-crossing based magnetometric protocol, the attainable

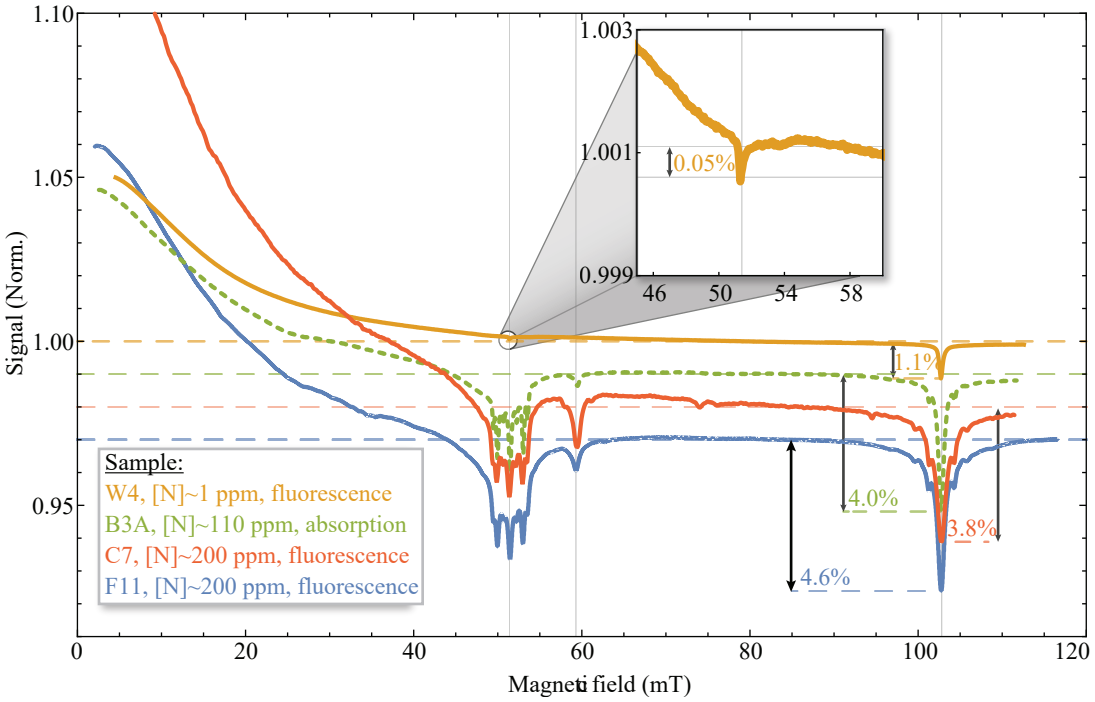

FIGURE 4.2: Traces of PL (solid) and absorption (dotted) signals for different [N]-density diamond samples as a function of the applied MF, normalized to their respective signals at 80 mT. For better visibility the traces have been offset as is indicated by the dotted lines. The observed contrasts are shown explicitly for the GSLAC feature for the different traces. The inset shows a detailed view on the W4 trace around 51.2 mT.

Sample	**W4**	**B3A**	**F11**	**C7**
Type	CVD	HPHT	HPHT	HPHT
Surface cut	(100)	(111)	(111)	(100)
[N] (ppm)	< 1	< 110	< 200	< 200
e^- irradiation dosage (cm^{-2})	10^{18}	2×10^{19}	10^{18}	10^{18}
e^- irradiation energy (MeV)	10	10	10	10
Sample annealing	720 °C, 2 h	700 °C, 2 h	700 °C, 3 h	750 °C, 3 h

TABLE 4.1: Diamond samples. CVD: chemical vapor deposition, HPHT: high pressure, high temperature.

photon-shot-noise-limited MF sensitivity is proportional to [41]:

$$\delta B(\mathrm{T}/\sqrt{\mathrm{Hz}}) \approx \frac{1}{\gamma/_{2\pi}} \frac{\Delta\nu_{\mathrm{mr}}}{C\sqrt{\mathcal{R}}}, \tag{4.1}$$

where $|\gamma/_{2\pi}| \simeq 28.024\,\mathrm{GHz\,T^{-1}}$ is the gyromagnetic ratio of the electron spin, and $\mathcal{R}$ is the rate of detected photons in either PL or absorption measurements. $\Delta\nu_{\mathrm{mr}}$ and C are the full width at half maximum (FWHM) linewidth and contrast of the GSLAC feature, respectively. It follows that, for a given photon-collection rate $\mathcal{R}$, to achieve the highest MF sensitivity, the ratio of contrast to linewidth needs to be maximized.

In Fig. 4.2 we present normalized PL and absorption measurements as a function of the background MF following an initial alignment of the electromagnet. This figure gives an overview of the changes in contrast and linewidth of the observable, anti-crossing, features for all the samples listed in Table 4.1. The MF for W4 and B3A is scanned from 0 to 110 mT in 10 s, and the presented signal is the average of 64 traces. The MF of the EPR magnet in Riga is scanned in 100 s from 0 to 120 mT, and the presented signal is the average of 35 traces. The PL data using sample F11 are taken from Ref. [113]. The presented traces contain several features extensively discussed in past [10, 50] and more recent [9, 113, 116] works. In particular, the initial gradual decrease in the observed signals is associated either with a reduction in PL emission (samples W4, C7, F11; Fig. 4.1), or with an increase in absorption (sample B3A; Fig. 4.1) from the non-aligned NV centers due to spin-mixing. When a magnetic field is applied not along the NV-axis, it mixes the Zeeman sublevels. This resulting spin mixing reduces the effect of the optical pumping, and thus, decreases the population of the $^3\mathrm{A}_2$ m_s=0 spin state and increases the population of the metastable singlet state. Moreover, around 51.2 mT, the observed features for samples F11, B3A and C7 correspond to cross-relaxation between the NV center and substitutional nitrogen (P1) centers. We note here, that, for the most dilute sample used in this work (W4) we observe a significantly different structure. At a field of 51.2(1) mT (calibrated with microwave-spectroscopy measurements; not shown here) we observe a small drop in PL (contrast 0.05%) that could be attributed to the excited state level-anticrossing (ESLAC) of the NV center. Detailed investigation of its origin will be the subject of future work. The feature at 60 mT is attributed to cross relaxation with NV centers that are not aligned along the MF [9, 10, 113]. At ∼102.4 mT we observe the feature attributed to the GSLAC of the NV center. Several additional features

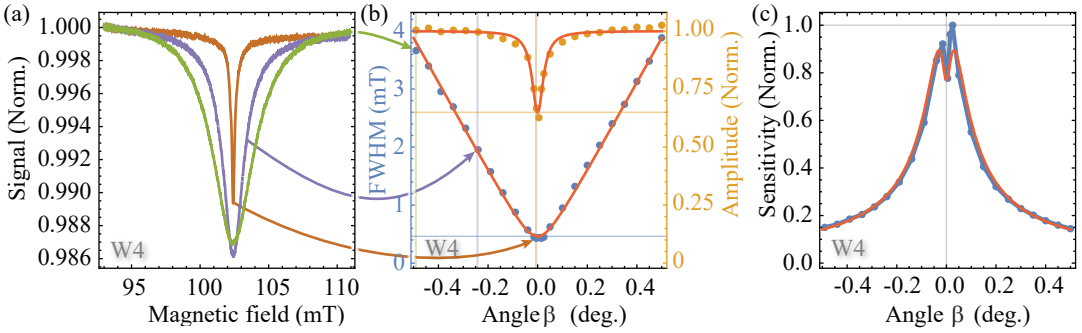

FIGURE 4.3: (a) GSLAC fluorescence contrast of diamond sample W4 as a function of the applied MF at different y-axis angles to the NV axis. (b) GSLAC FWHM width (blue dots) and contrast amplitude (amber dots) as a function of misalignment angle (x-axis). The experimental data are represented with dots, and the fits with solid lines. (c) Magnetic-field sensitivity (amplitude/width) as a function of misalignment angle β, normalized to the maximum obtained sensitivity.

are visible, however, here, we focus on the contrast and linewidth of the central component due to their relevance to magnetometry applications (see Eq.4.1). Finally, we tried to rule out MF gradients as the limitation of the GSLAC-feature width as reported before for sample F11 [113]. Therefore, a sample C7 with a comparable NV density was investigated in a highly homogeneous EPR magnet in Riga. However, due to alignment constraints, the results were inconclusive. We add them here for completeness.

In Fig. 4.3 we present PL-based measurements investigating the dependence of the GSLAC-feature lineshape on MF alignment for the dilute sample W4, which displays the narrowest linewidth, as seen in Fig. 4.2. In particular, the angles α (z-axis) and β (y-axis) between the NV-axis and the applied MF are controlled with a precision better than 0.01 degrees. Following an initial alignment optimization of both angles towards minimal GSLAC linewidth, we record traces of the feature as a function of the angle β. Figure. 4.3 (a) shows three examples of the recorded traces for different values of β. The data are then fitted with a Lorentzian function to extract the GSLAC feature's FWHM linewidth and contrast amplitude. The resulting data are displayed in Fig. 4.3 (b). While decreasing β from large misalignment angles ($|\beta| > 0.1$ degrees), the linewidth reduces linearly towards a minimal value of $\Delta\nu_{\mathrm{mr}} = 0.46(2)$ mT. The contrast amplitude, however, stays constant and then sharply decreases to less than 65% of its value for large misalignment. The contrast-amplitude data are presented in Fig. 4.3 (b), and are fitted with a Lorentzian function, yielding a FWHM width for the observed

feature of $54(4)\times10^{-3}$ degrees. This observed feature, resulting from a misalignment angle between the MF and the NV-axis, can be translated into a transverse MF-component of 97(7) μT in magnitude. This behavior can be interesting for applications of transverse MF sensing (similarly to the work presented in Ref. [117]), which we will pursue further in the future. For longitudinal MF sensing however, this effect leads to an undesirable behavior, which we demonstrate in Fig. 4.3 (c). Here we present as a measure for longitudinal MF sensitivity (Eq. 4.1), the ratio of contrast to linewidth. Due to the different angle dependence of the GSLAC feature width and the contrast amplitude, it appears that the sensitivity has a local minimum for optimum angle alignment ($\beta = 0$) and a maximum for a non-zero angle of $|\beta| = 0.01$ degrees. At this angle, the amplitude of the GSLAC feature is highly sensitive to transverse magnetic fields, as well as to mechanical angle fluctuations which will appear as an additional (non-magnetic) noise source.

In Fig. 4.4 we present transmission measurements of 1042 nm light propagating through a cavity-enhanced absorption-based magnetometer utilizing the B3A sample, as a function of the applied background MF field and of the 532 nm pump-light power. We note here, that for the measurements presented in Fig. 4.4 (a), (b), & (c), the 532 nm light-beam spot-size and 1042 nm light-beam spot-size on the diamond were similar and approximately equal to ∼50 μm. In particular, in Fig. 4.4 (a) & (b) we present three examples of the recorded traces for three different values of 532 nm light power. While we observe a similar behavior and features as for the PL-detection measurements (see Fig. 4.2 and the preceding discussion), a different initial signal drop, as well as, different GSLAC contrast amplitudes are observed for different 532 nm light powers. Figure.4.4 (b) shows a detailed expansion of the GSLAC-feature for the three different 532 nm light powers used in Fig. 4.4 (a), along with the respective contrast amplitude. Moreover, a shift in the position of the feature, caused by a temperature increase due to the 532 nm pump light is observed (see, for example, Ref [3] for a discussion of the temperature dependence of the ground state $^3A_2$ splitting). All recorded traces at different 532 nm light powers are fitted with a Lorentzian function, allowing us to extract the GSLAC feature's FWHM linewidth and contrast amplitude. The resulting data for the GSLAC contrast amplitude are displayed in Fig. 4.4 (c), showing a saturating behavior that yields a maximum attainable contrast of 15% [resulting from the fit shown in Fig. 4.4 (c)]. We did not observe a significant change in the GSLAC FWHM as a function of the 532 nm light power, and the average GSLAC FWHM of the recorded data is 0.84(1) mT.

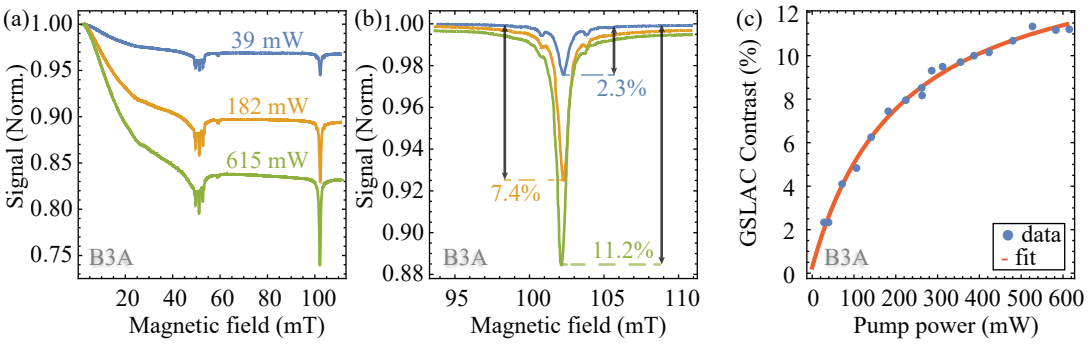

FIGURE 4.4: (a) Transmission signal of 1042 nm light through the optical cavity utilizing sample B3A, as a function of applied magnetic field, and normalized to the measured transmission at zero-field. The three traces presented correspond to different pump-light powers. (b) Detail of the magnetic-field scan around the GSLAC feature for different pump-light powers normalized to the background transmission at 80 mT. (c) GSLAC-feature contrast amplitude as a function of pump-light power.

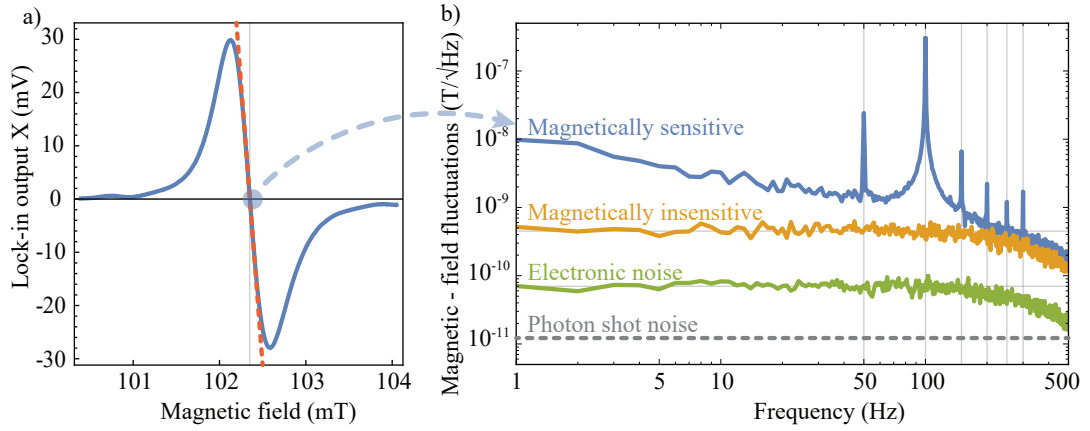

FIGURE 4.5: Absorption-based magnetometry with sample B3A. (a) Detail of the LIA output around the GSLAC feature (blue) with a linear fit to the data (red, dotted). The fit is used to calibrate the magnitude of the magnetic field fluctuations. (b) Noise of the magnetometer: magnetically sensitive at a field of 102.4 mT, magnetically insensitive at a field of 80 mT (average noise between 1−100 Hz is 0.45 $\mathrm{nT}/\sqrt{\mathrm{Hz}}$), and electronic noise with no cavity transmission (average noise between 1−100 Hz is 70 $\mathrm{pT}/\sqrt{\mathrm{Hz}}$). The photon shot noise limit of the magnetometer is indicated at 12.2 $\mathrm{pT}/\sqrt{\mathrm{Hz}}$. The decrease in signal for frequencies above 200 Hz is due to the filtering of the LIA.

Finally, we demonstrate the MF sensitivity of the implemented absorption-based magnetometer utilizing sample B3A, using the GSLAC feature. For a 532 nm pump-light power of $\sim$ 600 mW, we record the transmission of 1042 nm light locked on resonance to the optical cavity, while bringing the NV-center's energy levels into the GSLAC (102.4 mT). In particular, by scanning the background MF around the GSLAC feature while applying a small oscillating MF ($B_m \simeq 0.01$ mT at the modulation frequency of 15 kHz), we record the transmission signal using a photodiode (Thorlabs, PDA36A-EC). We obtain the signal-component oscillating at the modulation frequency using a LIA (SRS 865; demodulation time constant 3 ms). The resulting demodulated absorption signal (as detected in the properly phased LIA X output) is presented in Fig. 4.5 (a). It depends linearly on the applied background MF around the GSLAC, and can, therefore, be used for precise magnetometric measurements. Thus, by setting the background MF field value exactly to the center of the GSLAC feature (102.4 mT) we record the transmission signal for an acquisition time of 1 s. In Fig. 4.5 (b) we present the resulting MF noise-spectrum of the acquired data. We observe a 1/f MF sensitivity limited by the noise of the electromagnet-current power supply and ambient noise, and demonstrate a noise floor of magnetically insensitive measurements corresponding to $0.45\,\mathrm{nT}/\sqrt{\mathrm{Hz}}$. The peaks at 50 Hz and harmonics are attributed to magnetic noise in the lab and are not visible on the magnetically insensitive spectrum, which is obtained operating at a background MF value of 80 mT. The electronic noise floor was measured as $70\,\mathrm{pT}/\sqrt{\mathrm{Hz}}$. The photon-shot-noise limit is calculated to be $12.2\,\mathrm{pT}/\sqrt{\mathrm{Hz}}$ for 4.2 mW of collected 1042 nm light (Eq. 4.1), and the quantum-projection-noise limit, related to the number of NV centers we probe, is calculated to be $0.7\,\mathrm{pT}/\sqrt{\mathrm{Hz}}$.

§ 4.5 Conclusions

In this article, we investigate two approaches to increasing the magnetometric sensitivity in microwave-free diamond-based magnetometers using the GSLAC of the NV center. Sensitivity gains via feature width-reduction are problematic due to an experimentally observed amplitude decrease for a dilute sample at optimum alignment. The measured feature in misalignment angle is very narrow [corresponding to a transverse MF of 97(7) μT] and has the potential to be used for transverse MF magnetometry. For magnetometry along the background MF, however, a more promising route is the increase of signal amplitude in an absorption-based setup. We demonstrate an improved microwave-free magnetometer setup based

on a cavity-enhanced singlet-absorption GSLAC measurement, which exhibits an average noise floor of $0.45\,\mathrm{nT}/\sqrt{\mathrm{Hz}}$, and for our experimental conditions a photon-shot-noise limit of $12.2\,\mathrm{pT}/\sqrt{\mathrm{Hz}}$.
Future investigations will involve a thorough study of the lineshape and width of the signal near the GSLAC and ESLAC, as well as the additional features around it, with the aim of understanding the fundamental sensitivity and bandwidth limitations [99] of our sensing protocol.

§ 4.6 Acknowledgements

We acknowledge support by the DFG through the DIP program (FO 703/2-1). HZ is a recipient of a fellowship through GRK Symmetry Breaking (DFG/GRK 1581). GC acknowledges support by the internal funding of JGU. The Riga group gratefully acknowledges financial support from the Latvian National Research Programme (VPP) project IMIS2. LB is supported by a Marie Curie Individual Fellowship within the second Horizon 2020 Work Programme. DB acknowledges support from the AFOSR/DARPA QuASAR program. We thank Victor M. Acosta and J. W. Blanchard for fruitful discussions.

§ 4.7 Author contribution

For the work presented in this chapter, Dr. H. Zheng led the experiment. I constructed the NV-absorption-based MW-free sensor whose sensitivity plot was presented. I acquired the data for Fig. 4.4 and Fig. 4.5 and prepared said figures. I provided the data for sample B3A in Fig. 4.2. I aided with the formatting of the rest of the figures and along with the other co-authors, I co-wrote the manuscript.

§ 5

Eddy-current imaging with nitrogen-vacancy centers in diamond

§ 5.1 Abstract

We demonstrate microwave-free eddy-current imaging using nitrogen-vacancy centers in diamond. By detecting the eddy-current induced magnetic field of conductive samples, we can distinguish between different materials and shapes and identify structural defects. Our technique allows for the discrimination of different materials according to their conductivity. The sensitivity of the measurements is calculated as $8\times10^5\,\mathrm{S/m}\sqrt{\mathrm{Hz}}$ at 3.5 MHz, for a cylindrical sample with radius $r_0 = 1\,\mathrm{mm}$ and height $h = 0.1\,\mathrm{mm}$ (volume $\sim 0.3\,\mathrm{mm}^3$), at a distance of 0.5 mm. In comparison with existing technologies, the diamond-based device exhibits a superior bandwidth and spatial resolution. In particular, we demonstrate a flat frequency response from DC to 3.5 MHz and a spatial resolution of $348 \pm 2\,\mu\mathrm{m}$.

§ 5.2 Introduction

Magnetic induction measurements have proven to be useful in biomedicine [75], security and surveillance [36, 52], and materials testing [32]. Magnetic-induction imaging works by detecting magnetic fields produced by eddy-currents. When a material is placed in an alternating magnetic field (primary field), electric fields

will be induced in the material, causing eddy-currents to flow. These in turn will produce a secondary magnetic field, that can be detected along with the primary field. The secondary field depends on the material's properties and shape, as well as the skin depth of the primary field. Eddy-current detection has been commercially available with coil-based devices (e.g. Zetec, MIZ-22). Recently it has also been demonstrated using vapor-cell magnetometers [74, 111, 112].

Here, we demonstrate eddy-current imaging using magnetic sensing with nitrogen-vacancy (NV) centers in diamond. Compared to other sensors, diamond-based devices operate in a wide temperature range and may have nanoscale-resolution [12, 77, 91] with high sensitivity [16, 26] and wide bandwidth [26]. The present eddy-current measurements are performed using an all-optical NV magnetometer. The device has a bandwidth of 3.5 MHz and exhibits a spatial resolution of 348 μm.

§ 5.3 Experimental setup

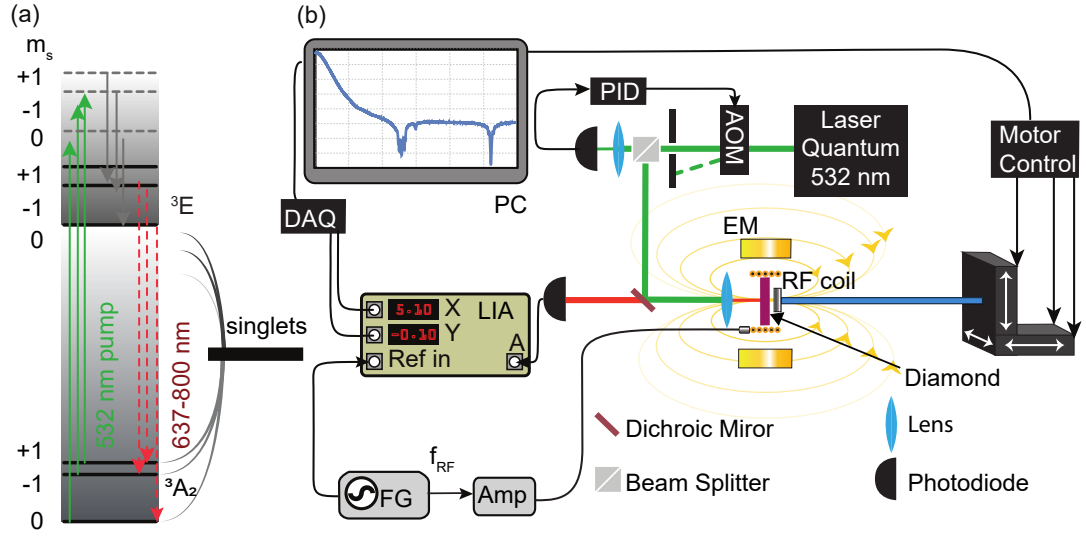

FIGURE 5.1: (a) Relevant NV center energy levels and transitions. Solid green and red lines indicate excitations, dashed lines indicate radiative transitions, and gray solid lines indicate non-radiative transitions. (b) Schematic of the experimental setup.

Fig. 5.1 NV center energy levels. The ground and excited electronic spin-triplet states of the NV are $^3A_2$ and ^3E, respectively, with the transition between them having a zero-phonon line at 637 nm. Additionally, there are two singlet states. Optical transition rates in the system are spin-independent, however, the probability of nonradiative intersystem crossing from ^3E to the singlets is several times

higher for $m_s = \pm 1$ than that for $m_s = 0$ [41]. As a consequence, under continuous illumination with green pump light (532 nm), NV centers are prepared in the $^3A_2$ $m_s = 0$ ground state sublevel and in the metastable ^1E singlet state. Population in the $^3A_2$ $m_s = 0$ state, then gets excited by the green light and decays back, emitting red photoluminescence (PL).

The setup consists of a microwave-free diamond magnetometer in AC-mode, a driving coil to induce eddy currents and a 3D-translation stage to make spatially dependent eddy-current measurements i.e. to create a conductivity image. The setup is shown in Fig. 5.1 (b). The diamond used for this sensor is a type Ib, (111)-cut, HPHT grown sample, purchased from Element Six. Its dimensions are $3\times3\times0.400\,\mathrm{mm}^3$. The initial nitrogen concentration of the sample was specified as $<110\,\mathrm{ppm}$. The sample was irradiated with 14 MeV electrons at a dosage of $10^{18}\,\mathrm{cm}^{-2}$ and then annealed at $700\,^o\mathrm{C}$ for three hours. Green light is provided to the setup by a diode-pumped solid-state laser (Laser Quantum, gem 532). The power of the laser is stabilized using an acousto-optical modulator (AOM, ISOMET-1260C with an ISOMET 630C-350 driver) controlled with a proportional-integral-derivative controller (PID, SRS SIM960). The light is focused on the diamond using a 50 mm lens. Before being detected with a photodiode (Thorlabs PDA36A-EC), the PL is filtered with a dichroic mirror. The samples to image are attached on to a 24 cm non-conductive rod, which is screwed onto a motorized, computer controlled, 3D-translation stage system (Thorlabs, MTS25-Z8). Using the translation stage, the samples are moved in front of the diamond. The eddy-current inducing magnetic field is produced with a function generator (FG, Tektronix AFG 2021), ranging from 2 Hz to 4 MHz. The signal is supplied to a coil placed around the diamond (RF coil) with five turns and 3.4 mm diameter. It is made from 0.05 mm diameter copper wire.

The all-optical magnetometric scheme to detect oscillating magnetic fields used here requires a homogeneous background field, which is provided by an electromagnet (EM). Both the diamond and the RF coil are placed inside the bore of the custom-made EM. The magnet consists of $\sim$200 turns wound with a rectangular-cross-section ($1.4\,\mathrm{mm}\times0.8\,\mathrm{mm}$) wire around a 5 cm-diameter bore. The coil is wound on a water-cooled copper mount, and produces a background field of 2.9 mT per ampere supplied. A current up to 55 A is provided by a Keysight N8737A power supply. A lock-in amplifier (LIA) (SRS, SR865), referenced at the eddy-current frequency, detects the amplitude (R) and phase (θ) of the PL modulation. R and θ are recorded on a personal computer (PC) along with the position of the 3D-translation stages.

§ 5.4 Magnetometry

The detection of magnetic fields commonly requires the use of microwaves to manipulate the spin state of the NV ensemble [26]. However, in close proximity to conducting materials the amplitude and phase of the microwaves are affected. For this reason we developed microwave-free detection techniques [113,119] that make use of different cross-relaxation and/or quenching mechanisms at various magnetic fields applied to the diamond. We demonstrate the mechanism with an EM, but in a miniaturized device, this could be replaced by a carefully chosen permanent magnet.

PL by the NV centers displays several features discussed in the literature as a function of magnetic field [9,10,50,113,116,119], which can be used for magnetometry. Figure 5.2 (a) presents normalized PL measurements as a function of the background magnetic field at different alignments of the magnetic field relative to the NV axis. Figure 5.2 (b) shows the corresponding amplitude of the PL oscillation due to the oscillating magnetic fields, R as measured with a LIA component from the lock-in amplifier. We investigated three different areas: α) the slope from 0 to $\sim 25\,\mathrm{mT}$, β) the cross-relaxation features around 50 mT and γ) the ground-state level anti-crossing (GSLAC) feature at 102.4 mT. To perform the measurements, we apply a bias field and maximize R for the different features. While R is maximized due to the quadratic shape of the feature, we are not sensitive to small changes in the bias field. However because we are demodulating at the frequency of the eddy current using a lock-in amplifier, we are sensitive to AC field changes.

As it is shown in Fig. 5.2 (b) the maximum R is obtained at the GSLAC for the red trace. However, as demonstrated in the literature [119], this feature is sensitive to misalignment. To make the sensor more robust to misalignment, we perform the measurements, at area α. Even though area α is less sensitive it allows for robustness which will be useful in a portable device. Instead of requiring a highly homogeneous magnetic field, a standard permanent magnet could bias the field. The smaller field value additionally facilitates implementation in a miniaturized sensor and requires less power dissipation if an EM is used.

For eddy-current detection measurements a broad bandwidth is important because the frequency of the primary field determines its penetration depth into the sample under study. The penetration depth in turn provides information about the geometry, thickness, and material of the sample. Hence, to optimize images of different thickness materials, a wide frequency range is beneficial. Furthermore,

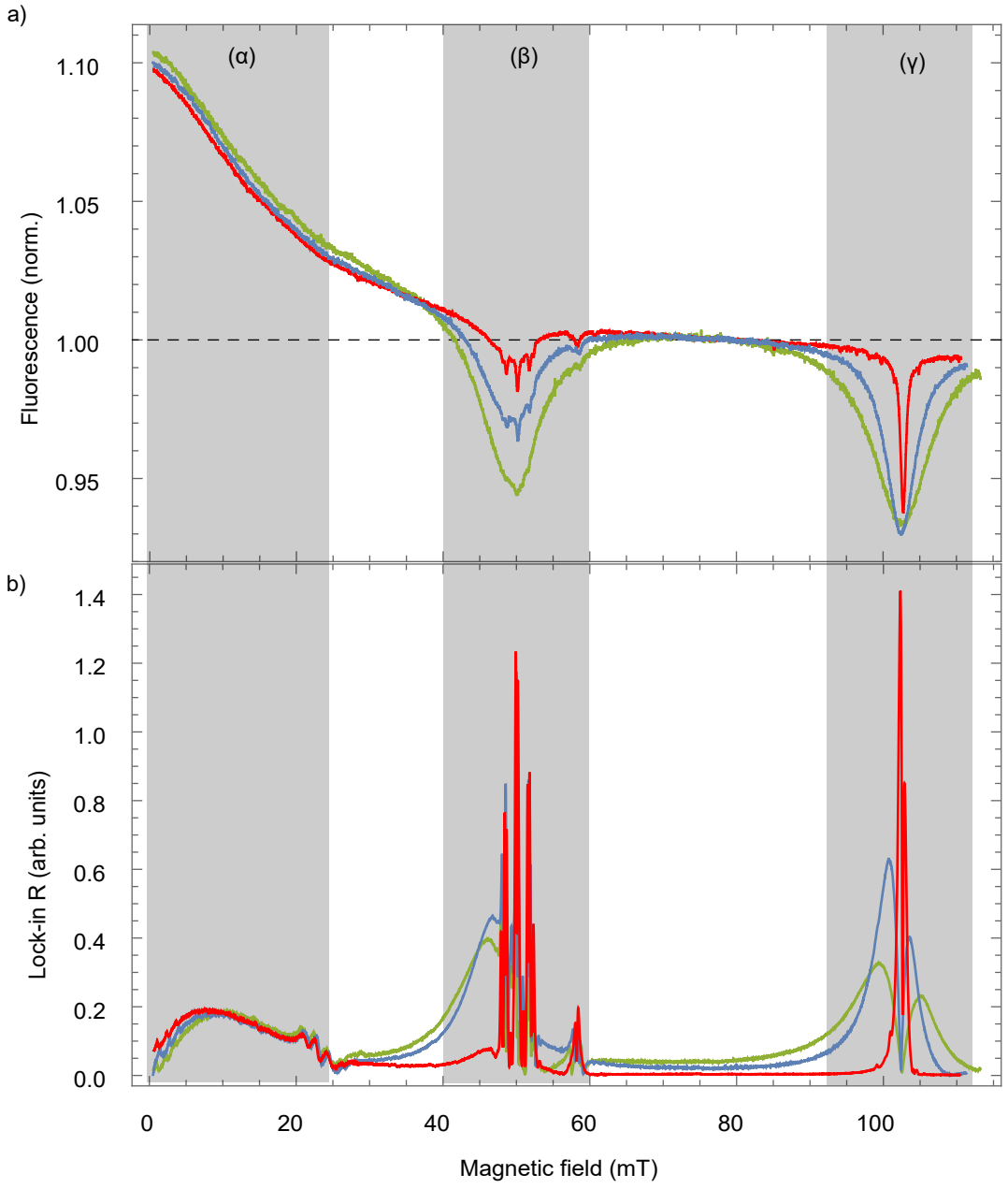

FIGURE 5.2: (a) Fluorescence as a function of magnetic field at different alignments (up to $\sim 5^o$) between the NV and magnetic field axis. The smallest misalignment is represented by the red trace and the biggest by the green. The data is normalized to the PL at 80 mT. (b) Lock-in amplifier R component for the same alignments between the NV and the magnetic field axis, with an applied magnetic field modulation of 60 kHz and an amplitude of 50 μT. The shaded areas α, β, γ represent magnetic field values at which we performed AC magnetometry

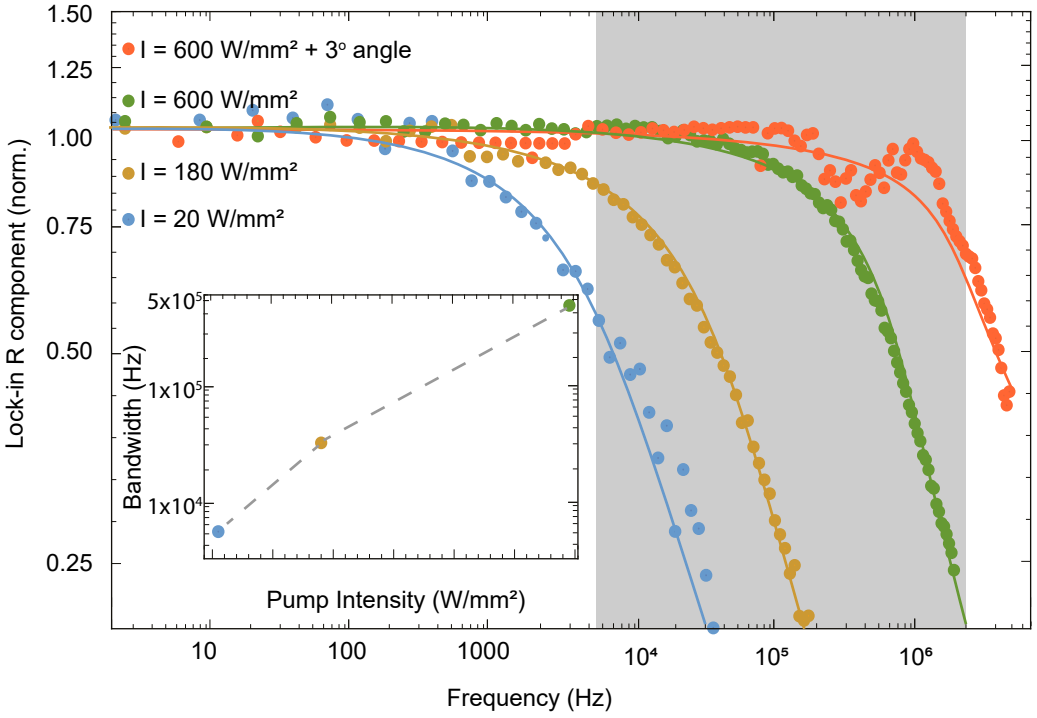

FIGURE 5.3: Eddy current response as a function of frequency. The blue, orange and green measurements show the bandwidth of the device for different pump power intensities. The red measurement is taken at saturation pump intensity and with 3^o misalignment between the NV and magnetic field axis. The shaded area between 7 kHz and 2 MHz represents the maximum reported bandwidth of current atomic based sensors used for eddy-current imaging. [73, 112]. The inset shows the bandwidth of the magnetometer versus intensity with the corresponding colors of the traces.

higher frequencies enhance the response and make it possible to image materials with lower conductivity. Figure 5.3 shows the normalized eddy-current response as a function of frequency, to characterize the sensor's bandwidth. The blue trace is taken at a pump intensity of $I = 20\,W/mm^2$, the orange at $I = 180\,W/mm^2$ and the green at $I = 600\,W/mm^2$, which corresponds to the saturation intensity for the probed NV volume. The inset shows the normalized PL of the NV as a function of pump light intensity. The intensity values at which the data are taken are represented in the inset with the corresponding colors of the main plot. The measurements are fitted with first order low-pass-filter functions. As illustrated in Fig. 5.3, the bandwidth can be tuned by varying the laser-light intensity and by changing the alignment between the NV axis and magnetic field, which affects the mixing of the NV $m_s = 0$ and $m_s = -1$ states [119]. We demonstrate a maximum bandwidth ~ 3.5 MHz.

§ 5.5 Spatial Resolution

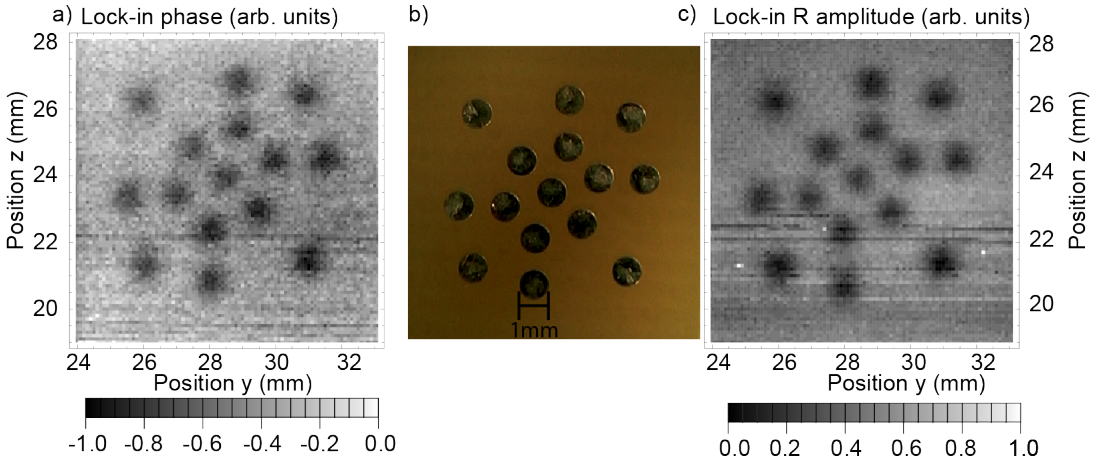

FIGURE 5.4: a),c) Lock-in Phase and Lock-in R amplitude for a PCB containing fifteen aluminum dots imaged with eddy-current b) photograph of the PCB with the corresponding length of 1 mm noted for scale.

One of the advantages of NV-based sensors is their spatial resolution. For eddy-current imaging, for a constant conductivity, the smaller a material is, the smaller the amplitude of the secondary field it produces. As a test of spatial resolution, we image fifteen 1 mm-diameter 35 µm thick disks made out of aluminum. The amplitude and phase response of the magnetic field sensor caused by these disks is shown in Fig. 5.4. Both the disks and the distance between them, which is sub-mm, are clearly visible. Note that covering the pattern with aluminum foil adds an offset but does not significantly alter the eddy-current image patterns shown in Fig. 5.4 a and c.

Figure 5.5 shows the average cross section of the fifteen 1 mm disks imaged in Fig. 5.4. Using the average detected cross section data we deconvolute them with a square function, searching for a Gaussian function kernel that would recreate the experimental result. The kernel provides information about the disks' width. In Fig. 5.5 the red plot signifies the disks' width of 1 mm as a square function, the blue dots are the experimental data, the green trace represents the Gaussian function kernel and the convolution result of the red and green traces. All the traces amplitudes are normalized to unity for representation in the figure. The Gaussian kernel full-width-half-maximum is 348 ± 2 µm which we use as a measure for the spatial resolution of the sensor. The spatial resolution is mostly limited by the distance between sample and sensor. The diamond thickness sets the minimum distance to the sample. To decrease the distance between the sensor and the

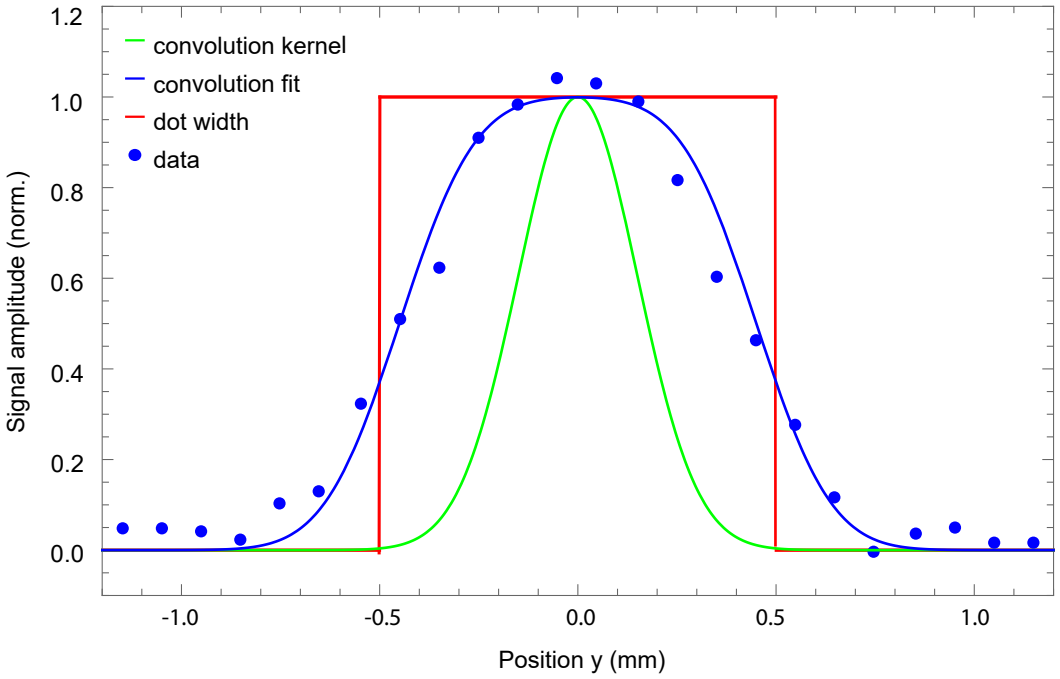

FIGURE 5.5: Determining spatial resolution. The blue dots signify the average cross section of fifteen 1 mm disks imaged by our sensor, the red plot signifies the disks' width as a square function, the green trace represents a Gaussian function needed as a kernel to recreate the experimental data and blue trace represents the convolution result of the red and green trace.

imaged sample a thinner diamond sample or a diamond with a shallow implanted NV layer could be used. A close proximity would improve measurement contrast and therefore the spatial resolution and allow the imaging of smaller objects.

Using the high bandwidth and spatial resolution of the device we are able to image intricate structures on printed circuit boards (PCBs). Figure 5.6 shows a miniature coat-of-arms of the city of Mainz as imaged by the eddy-current based method. The coat-of-arms is printed on a PCB, made out of copper with a 35 µm thickness.

§ 5.6 Sensitivity

To calculate the sensitivity of the device we have to make assumptions about the sample imaged. We assume a primary field of $B_{prim.} = 91\,\mu\text{T}$ with frequency of 3.5 MHz, a cylindrical material with radius $r_0 = 1\,\text{mm}$ and height $h = 0.1\,\text{mm}$ (volume $\sim 0.3\,\text{mm}^3$). The sensor is placed at a distance $d = 0.5\,\text{mm}$ from the material. We calculate the minimum conductivity σ that the material should have

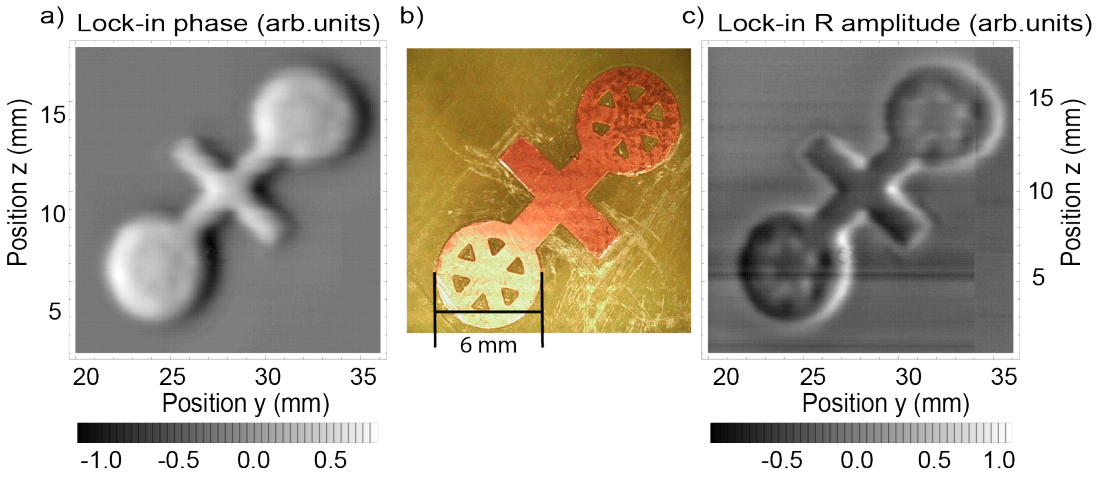

FIGURE 5.6: a),c) Lock-in θ and R of a PCB depicting the symbol of the city of Mainz imaged with eddy-current. b) photograph picture of the PCB with the corresponding length of 6 mm noted for scale.

in order to produce a field strong enough to be detected with our magnetic field sensor (current sensitivity $\sim 10\,\mu\mathrm{T}/\sqrt{\mathrm{Hz}}$).

The secondary magnetic field can be calculated using the expression for the electromotive force (EMF)

$$U = -\frac{\Delta\Phi}{\Delta t} = -2E\pi r, \tag{5.1}$$

where $\Delta\Phi$ is the magnetic flux and $1/\Delta t = \omega = 2\pi\mathrm{f}$, f being the modulation frequency of $B_{prim.}$, E is the electric field and r is the distance from the center of the imaged sample. Using Biot-Savart's law, the field produced by the eddy-currents (i.e. secondary field, $B_{sec.}$) and the minimum σ able to be detected can be calculated. For the example presented it would be $\sim 8\times10^5\,\mathrm{S/m}/\sqrt{\mathrm{Hz}}$. Enough to detect small pieces of materials like copper and aluminum, ($\sigma_{copper} = 5.96\times10^7\,\mathrm{S/m}$, $\sigma_{aluminium} = 3.77\times10^7\,\mathrm{S/m}$) will be visible with our sensor.

§ 5.7 Discussion

We have demonstrated eddy-current imaging using NV centers in diamond. The magnetic sensitivity is achieved with an all-optical method that is robust to misalignment and makes use of the NV-NV cross-relaxation feature in the PL as function of the magnetic field. The bandwidth extends to 3.5 MHz. The spatial resolution is $348\,\mu\mathrm{m} \pm 2\,\mu\mathrm{m}$. The sensitivity of the device is calculated as $8\times10^5\,\mathrm{S/m}\sqrt{\mathrm{Hz}}$ at 3.5 MHz, for a cylindrical sample with radius $r_0 = 1\,\mathrm{mm}$ and

height $h = 0.1\,\mathrm{mm}$ (volume $\sim 0.3\,\mathrm{mm}^3$) at a distance of 0.5 mm. Combining the above characteristics our device can be used, to distinguish between different materials, detect structural defects, and image complex structures on PCBs. The technique can be further improved by closer proximity to the imaged sample, which can be achieved using a thinner diamond or one with a shallow implanted NV layer. Compared to measurements with atomic vapor cells, the current NV-based method has superior bandwidth and spatial resolution. Comparing with coil-based commercial devices, it features superior bandwidth (e.g. Zetec, MIZ-22, bandwidth 50 Hz to 2 MHz) and sensitivity ($5\times10^5\,\mathrm{S/m}$).

With its high bandwidth and spatial resolution, if combined with state-of-the-art NV sensors [16,26] the sensitivity (on the order of 10 $\mathrm{pT}/\sqrt{\mathrm{Hz}}$) would be sufficient for applications in biomedicine to distinguish between different tissues, or even healthy and unhealthy tissues, because of their different conductivities (ranging from 0.5 mS/cm to 13.7 mS/cm) [45] . The device's robustness to misalignment and small size would allow it to be implemented on a hand-held, small and portable endoscopic sensor.

§ 5.8 Acknowledge

The authors acknowledge support by the EU FET-OPEN Flagship Project "ASTERIQS" (action # 820394), the German Federal Ministry of Education and Research (BMBF) within the Quantumtechnologien program (FKZ 13N14439), and the DFG through the DIP program (FO 703/2-1). GC acknowledges support by the internal funding of JGU. LB is supported by a Marie Curie Individual Fellowship within the second Horizon 2020 Work Programme. HZ is a recipient of a fellowship through GRK Symmetry Breaking (DFG/GRK 1581). We thank N. L. Figueroa for fruitful discussions.

§ 5.9 Author contribution

For the work presented in this chapter, I experimentally realized the idea of Dr. A. Wickenbrock to construct an eddy-current detection NV based sensor. I performed calculations to estimate the sensitivity and I constructed and optimized the magnetometer needed for the experiment. I programmed the required communication with scientific equipment. I performed the experiment and acquired the

data. With the help of Dr. A. Wickenbrock, I constructed the figures and with the help of the rest of the co-authors I co-wrote the manuscript.

§ 6

Fiberized diamond-based vector magnetometer

§ 6.1 Abstract

We present two fiberized vector magnetic-field sensors, based on nitrogen-vacancy centers in diamond. The sensors feature sub-nT/$\sqrt{\text{Hz}}$ magnetic sensitivity. We use commercially available components to construct sensors with a small sensor size, high photon collection, and minimal sensor-sample distance. Both sensors are located at the end of optical fibres with the sensor-head freely accessible and robust under movement. These features make them ideal for mapping magnetic fields with high sensitivity and spatial resolution ($\leq$ mm). As a demonstration we use one of the sensors to map the vector magnetic field inside the bore of a $\geq 100\,\text{mT}$ Halbach array. The vector field sensing protocol translates microwave spectroscopy data addressing all diamonds axes and including double quantum transitions to a 3D magnetic field vector.

§ 6.2 Introduction

Nitrogen-vacancy (NV) centers in diamond have attracted attention as magnetic field sensors with high spatial resolution [12, 77, 91] and sensitivity [16, 26]. The range of their application includes, but is not limited to, single neuron-action

potential detection [16], single protein spectroscopy [69], as well as in-vivo thermometry [61]. Advantages of NV-based magnetometers, compared to other magnetic field sensors, include their ability to operate in wide temperature and magnetic field ranges [119]. The ability to operate them also without the use of microwaves [113, 119, 120], has recently enabled a variety of new applications in environments where microwaves (MW) would be detrimental [27].

The NV consists of a substitutional nitrogen and an adjacent vacant carbon site. It can appear in different orientations along the crystallographic axes of the diamond lattice. This enables vector measurements of magnetic fields [29]. Vector magnetometry itself can be useful in magnetic navigation applications [30], magnetic anomaly detection, current and position sensing, and the measurement of biological magnetic fields [16]. Vector measurements near a background field of $\sim 100\,\mathrm{mT}$, where the NV's ground state level anti-crossing (GSLAC) occurs, are of particular interest [120]. Some of the challenges of vector measurements near the GSLAC field include the necessity to precisely align the NV and the bias magnetic field axes for optimum sensitivity of the microwave-free method [119] or the need to account for transversal field related nonlinearities of the NV gyromagnetic ratio when performing microwave spectroscopy.

One of the challenges NV magnetometers face is their low photon-collection efficiency. Approaches to increase the efficiency include, use of solid immersion lenses [49, 63, 101], or employment of infrared absorption [1, 26, 41, 42, 58]. Photoluminescence (PL) for fiberized sensors is preferentially collected with the same fiber delivering the pump light but detected on the input side of the fiber [87]. Despite considerable effort, even modern sensors typically just feature a PL-to-pump-light ratio of about 0.1% [16, 87].

In this paper, we discuss the construction of two fiberized NV-based vector magnetic field sensors one constructed in Helmholtz Institute Mainz, referred to as Mainz sensor in the following and the other one is a sensor demonstrator of Robert Bosch GmbH, referred to as Bosch sensor in the following. They both achieve sub-$\mathrm{nT}/\sqrt{\mathrm{Hz}}$ magnetic sensitivity. The sensor constructed in Mainz achieved a sensitivity of $453\,\mathrm{pT}/\sqrt{\mathrm{Hz}}$, limited by intensity noise of the pump laser, with $11\,\mathrm{pT}/\sqrt{\mathrm{Hz}}$ photon-shot noise sensitivity and 0.5% PL-to-pump power ratio taking the fiber coupling efficiency into account. The sensor constructed by Bosch achieved a sensitivity of $344\,\mathrm{pT}/\sqrt{\mathrm{Hz}}$, which was approximately one order of magnitude larger than the expected photon-shot noise limited sensitivity [104]. The PL-to-pump power ratio was 0.3% taking the fiber-coupling efficiency into account.

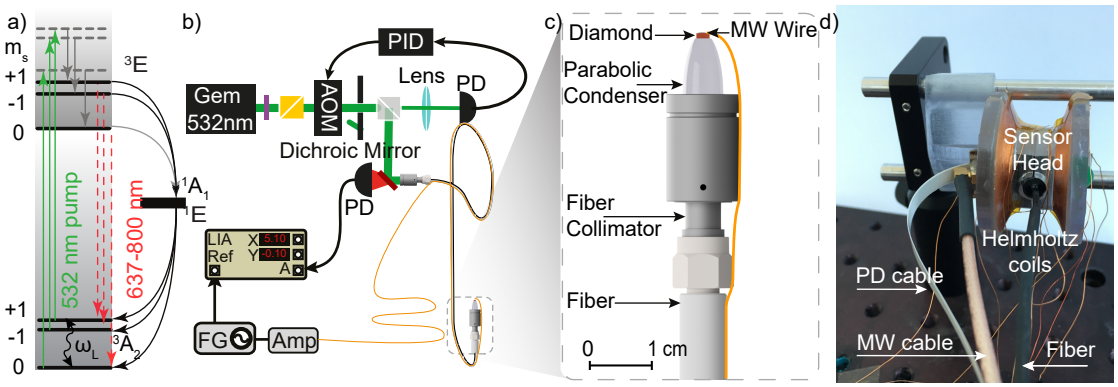

FIGURE 6.1: a) Relevant energy levels of the NV center. The states as well as their spin projection m_s are labeled. Solid green lines represent pump light, solid gray lines phononic de-excitation, dashed red lines represent PL, curved gray lines represent inter-system crossing. b) Experimental setup in Mainz (the experimental setup by Bosch can be found in Ref. [104]). c) Schematic of the fiberized sensor head. d) Photograph of the fiberized sensor by Robert Bosch GmbH. The abbreviations used in the figure are; PD: Photo-diode, AOM: acousto-optic modulator, PID: proportional-integral-derivative controller, LIA: lock-in amplifier, FG: function generator, Amp: amplifier, MW: microwave.

The components used for the construction of both sensors are commercially available. They allow for a small sensor size ($11 \times 40\,\mathrm{mm}^2$ for Mainz and $15 \times 25\,\mathrm{mm}^2$ for Bosch) with maximized PL-to-pump-light ratio, as well as robustness to movement, which also makes the sensors portable. All of this makes the sensors ideal for mapping magnetic fields and measuring in regions that are not easily accessible. The magnetometers are constructed in such a way that they allow close proximity of the sensors to magnetic field sources, thus allowing for high spatial resolution when mapping magnetic fields. After demonstrating the sensitivity of the sensors and explaining the principles of vector magnetometry with NV centers, we used the Mainz sensor to perform spatially resolved optically detected magnetic resonance (ODMR) measurements covering an area of $20 \times 30\,\mathrm{mm}^2$ inside a Halbach-magnet array. The Halbach array itself provides a highly homogeneous magnetic field around 100 mT which makes it ideal for near-GSLAC magnetic field measurements and studies with NV centers. We present the analysis for the translation of the extracted frequency measurements into magnetic field. Details about the construction of the highly homogeneous Halbach array is subject of another publication [114].

§ 6.3 Experimental Setup

The diamond sample used for the Mainz sensor is a $2.0 \times 2.0 \times 0.5\,\mathrm{mm}^3$ type Ib, (100)-cut, high-pressure high-temperature (HPHT) grown sample, purchased from Element Six. The initial [N] concentration of the sample was specified as $< 10\,\mathrm{ppm}$. The sample was irradiated with 5 MeV electrons at a dose of $2 \times 10^{19}\,\mathrm{cm}^{-2}$ and then annealed at 700 °C for 8 hours. The diamond sample used for the Bosch sensor is a $0.8 \times 0.8 \times 0.5\,\mathrm{mm}^3$ (111)-cut, 99.97 % ^{12}C enriched, HPHT grown diamond. The sample was irradiated with 2 MeV electrons at a dose of $2 \times 10^{18}\,\mathrm{cm}^{-2}$ at room temperature and then annealed at 1000 °C for 2 hours in vacuum. The [NV^-] concentration was determined by electron spin resonance to be 0.4 ppm [104].

Figure 6.1 (a) shows the relevant energy levels of the negatively charged NV center, which we use for magnetometry. The ground and excited spin-triplet states of the NV are labeled $^3A_2$ and ^3E, respectively [Fig. 6.1 (a)], the transition between them has a zero-phonon line at 637 nm, but can be exited by more energetic photons (of shorter wavelengths) due to phonon excitation in the diamond lattice. The lower and upper electronic singlet states are ^1E and $^1A_1$, respectively. While optical transition rates are spin-independent, the probability of nonradiative intersystem crossing from ^3E to the singlets is several times higher [41] for $m_s = \pm 1$ than that for $m_s = 0$. As a consequence, under continuous illumination with green pump light (532 nm), NV centers accumulate mostly in the $^3A_2$, $m_s = 0$ ground state sublevel and in the metastable ^1E singlet state. For metrology applications, the spins in the $^3A_2$ ground state can be coherently manipulated with microwave fields.

Figure 6.1 (b) shows the experimental setup used for the measurements conducted in Mainz. To initialize the NV centers to the ground-triplet state, we use a 532 nm (green) laser (Laser Quantum, gem532). To reduce intensity noise from the laser source, the light intensity is stabilized using an acousto-optic modulator (AOM, ISOMET-1260C with an ISOMET 630C-350 driver) controlled through a proportional-integral-derivative controller (PID, SIM960), in a feedback loop. The green laser is then coupled into a 2 m long, high-power multi-mode fiber cable (Thorlabs, MHP365L02).

The MW to manipulate the NV spins are generated with a MW function generator (FG; SRS, SG394). They are amplified with a 16 W amplifier (Amp; Mini-Circuits, ZHL-16W-43+) and passed through a circulator (Mini-Circuits, CS-3.000) before they are applied to the NV centers using a mm-sized wire loop. The other side

f_{res}	f_{mod}	f_{depth}	Detection limit
2880.4 MHz	3 kHz	100 kHz	$3.7 \pm 0.6\,\mathrm{nT}/\sqrt{\mathrm{Hz}}$
2894.3 MHz	2 kHz	100 kHz	$3.1 \pm 0.3\,\mathrm{nT}/\sqrt{\mathrm{Hz}}$
2873.5 MHz	5 kHz	100 kHz	$2.7 \pm 1.6\,\mathrm{nT}/\sqrt{\mathrm{Hz}}$

TABLE 6.1: Settings and detection limit for the three different NV axis used in the Bosch sensor.

of the wire is directly connected to ground. The radius of the wire used for the wire loop is 50 µm. The wire is then attached to the optical fiber allowing the two parts to move together. For the magnetic resonance measurements presented in this paper, the MW frequency was scanned between 3800 MHz and 5000 MHz. Information on the experimental setup used to conduct the measurements with the Bosch sensor can be found in Ref [104].

A schematic of the Mainz fiberized magnetic field sensor head is shown in Fig. 6.1 (c). The diamond is glued to a parabolic condenser lens, which itself is glued onto a 11 mm focal length lens and attached to a fiber collimator (Thorlabs, F220SMA-532) to which the high-power multi-mode fiber (Thorlabs, MHP365L02) is connected. The MW wire loop is attached to the other side of the diamond to provide the rapidly oscillating magnetic fields required for this magnetic field detection scheme. The light is delivered to the diamond via the parabolic condenser, lens, collimator and the high-power fiber. The same components collect the spin-state-dependent red PL of the NV ensemble. On the other side of the fibre the PL is filtered using a longpass dichroic filter (Thorlabs, DMLP605) which is also used to couple the incoming green light into the fiber. After the dichroic filter residual reflected green light is removed by a notch filter (Thorlabs, NF533-17) and the PL is focused onto a photodiode (PD; Thorlabs, PDA36a2). The detected signal with the PD is connected to a a lock-in amplifier (LIA; SRS, SR830). With this setup we were able to achieve 0.5% PL-to-pump-light ratio, which is an order-of-magnitude improvement compared to other fiberized sensors [87]. A photograph of the Bosch sensor can be seen in Fig. 6.1 (d). The sensor head, containing a microwave resonator, a custom designed balanced photodetector, and the diamond, which was glued to the collimated output of a single-mode fiber, is located inside a custom designed Helmholtz coil. The Helmholtz coil was used to generate a magnetic bias field of 1.07 mT and the collimation of the laser beam was achieved with a gradient-index lens (GRIN). Further details on the setup used for the Bosch sensor can be found in Ref. [104]. The final sensor head, of the Mainz sensor, has a diameter of ≤ 11 mm and a height of 40 mm, in a configuration that allows for

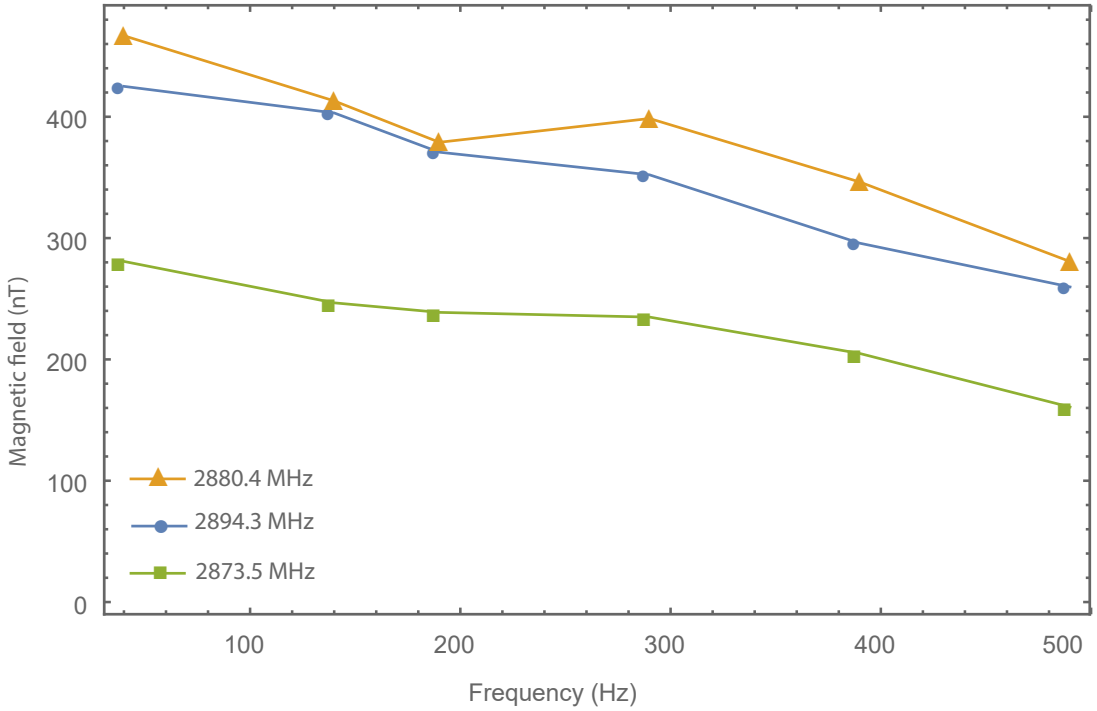

FIGURE 6.2: Amplitude of magnetic test signal, measured along three different NV axes with the Bosch sensor. An oscillating, external magnetic field of about 0.7 µT was applied to the sensor.

$\leq 300\,\mu m$ average distance between sample and sensor. The 2 m long fiber with the attached MW wire and the fiberized sensor head for the Mainz sensor (shown in Fig. 6.1 (c)) can be moved independently of the other components. The footprint of the sensor head of the Bosch sensor was $15 \times 25\,mm^2$. The smallest distance between the center of the diamond and the outer surface is roughly 2.4 mm, the sensor can move independently as well. To filter low-frequency systematic noise components, e.g. laser-power fluctuations, the MW-frequency ω_L is modulated and the detected PL is demodulated with the LIA. To produce the magnetic field maps presented here, the Mainz sensor assembly was mounted on a computer-controlled motorized 3D translation stage (Thorlabs, MTS25/M-Z8) in the center of the Halbach array (not shown in Fig. 6.1).

§ 6.4 Magnetic field sensitivity

Figure 6.2 depicts the response of the Bosch sensor for three different NV axes upon application of an AC magnetic field with varying frequencies and a constant amplitude of 0.7 µT. The three axes see different effective amplitudes due to the

different angles of the NV axes with respect to the magnetic field vector as expected. The sensor response slightly decreases with increasing frequency of the test field independent of the axis. This decrease might stem from the fact, that with increasing frequency, the excitation field becomes under-sampled meaning that the full reconstruction of the sinusoidal excitation field is not possible anymore leading to a decrease in measured amplitude.

To estimate the magnetic sensitivity of the two sensors we follow another method. When the MW field is resonant with the ground-state $m_s = 0 \rightarrow m_s = \pm 1$ transitions, population is transferred through the excited triplet state to the metastable singlet state, resulting in PL reduction. PL as a function of MW frequency is the ODMR signal. By focusing around a single of feature in this ODMR signal the sensitivity can be extracted. The magnetic resonance for the Mainz sensor features a 350 kHz linewidth and 1.6 % contrast. The best sensitivity of the Bosch sensor was achieved with a linewidth of $\approx$ 92 kHz and a contrast of 0.6 %. We modulate the MW frequency around a central frequency f_c, and record the first harmonic of the transmission signal with a LIA. This generates a demodulated signal, which together with the NV gyromagnetic ratio of $|{}^{\gamma_e}/_{2\pi}| \sim 28.024\,\mathrm{GHz\,T^{-1}}$ can be used to translate PL fluctuations to effective magnetic field noise. The optimized parameters resulting in the best magnetic field sensitivity for the Mainz sensor were: a modulation frequency of f_{mod} = 13.6 kHz and modulation amplitude of f_{amp} = 260 kHz. The sensitivity of the Bosch sensor was optimized for 3 different NV axes as summarized in table 6.1.

Figure 6.3 shows the magnetic-field-noise spectrum of the sensors. The blue trace of Fig. 6.3 corresponds to magnetically sensitive data of the Mainz sensor, the orange to magnetically insensitive. The purple and green trace correspond to magnetically sensitive spectrum of the Bosch sensor outside and inside a magnetic shield, respectively, finally the red trace corresponds to the insensitive plot. The magnetically insensitive spectrum can be obtained if f_c is selected to be far from the ODMR features. The peak at 50 Hz is attributed to magnetic field from the power line in the lab. The average sensitivity in the 60-90 Hz area is $453\,\mathrm{pT}/\sqrt{\mathrm{Hz}}$ and $344\,\mathrm{pT}/\sqrt{\mathrm{Hz}}$ for the Mainz and Bosch sensors, respectively. The noise traces for the Bosch sensor are based on continuous data series, that are recorded with a sampling rate of 1 kHz for 100 s. To calculated the amplitude spectral density (ASD), the data series was split in 100 consecutive intervals, each with a duration of 1 s. For each interval the ASD was calculated. The depicted is the average of the 100 ASDs.

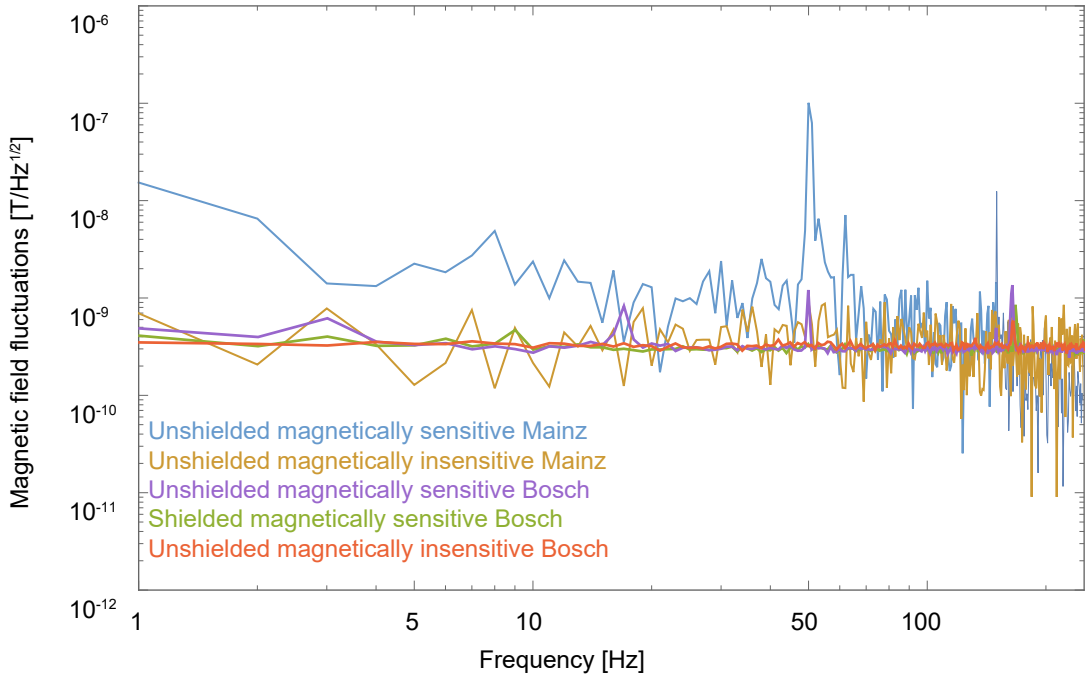

FIGURE 6.3: Magnetic field fluctuations measured with the fiberized NV magnetometers. The blue and orange traces depict magnetically sensitive and insensitive data of the Mainz sensor. The purple and green traces correspond to magnetically sensitive spectra of the Bosch sensor outside and inside a magnetic shield, finally, the red trace corresponds to unshielded magnetically insensitive data. The average sensitivity in the 60-90 Hz band is sub-nT/$\sqrt{\text{Hz}}$. The Bosch data are the result of 100 averages, while the Mainz data is from a single acquisition.

§ 6.5 Vector magnetic field sensing

Data Acquisition

As a demonstration of the robustness and portability of our sensors as well as the ability to produce highly resolved magnetic field maps, we select the Mainz sensor to characterize the homogeneity of a custom-made Halbach-array magnet constructed in the Mainz laboratory. The schematic of the magnet is shown in Fig. 6.4 (a) with more details found in Ref. [114]. It is a double ring of permanent magnets arranged to generate a homogeneous magnetic field in its inner bore along the radius of the rings. The field outside the construction decays rapidly with distance. We performed ODMR measurements in a $30 \times 20\,\text{mm}^2$ plane nearly perpendicular to the main magnetic field direction in the center of the Halbach

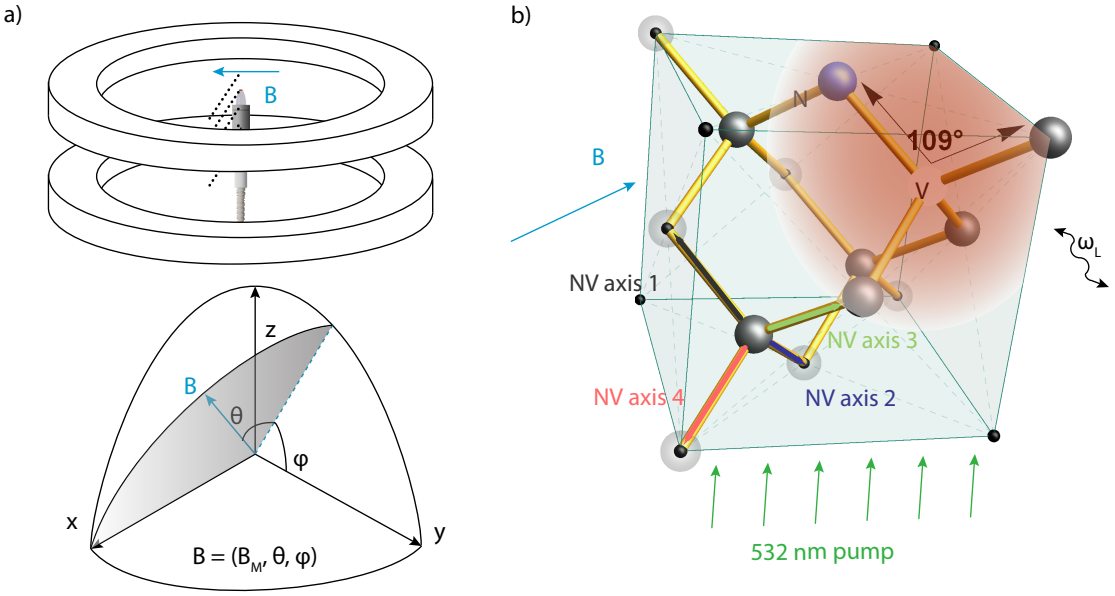

FIGURE 6.4: a) The orientation of the diamond sensor in the Halbach array. The orientation of the magnetic field is given in spherical coordinates with angle θ being the latitude angle with respect to the x-axis and ϕ the longitude. The main component of the magnetic field points along the x-axis. b) Illustration of the diamond lattice structure indicating the four different NV axes 1,2,3,4 and their relation to the applied magnetic field B. MW with frequency $\omega_L/(2\pi)$ are applied to the sample.

array in steps of 1 mm and 1.5 mm in z and y-direction, respectively. The experimental procedure to characterize this magnet involves reconstruction of the 3D magnetic field from these ODMR measurements, which we describe in the next part of this paper. The measurements confirmed the homogeneity of the magnetic field of the magnet to be consistent with Hall-probe and NMR measurements, but with a threefold improved field strength resolution, vector information of the magnetic field and sub-mm spatial information of these quantities. The orientation of the fiberized sensor in the Halbach magnet can be seen in Fig. 6.4 (a). The magnetic field is given in spherical coordinates with respect to the (100) axis of the diamond $\vec{B} = (B_M, \theta, \phi)$. The angle between the magnetic field vector and the yz-plane is θ, and ϕ is the angle between the projection of $\vec{B}$ in the yz-plane and the y-axis. The diamond sensor was oriented in the magnetic field such that different resonances were visible.

For each position in the $30 \times 20\,\mathrm{mm}^2$ plane a scan of the applied MW frequency between 3800 MHz and 5000 MHz was performed in steps of 1 MHz. This range was limited by the bandwidth of the MW components. At each frequency we

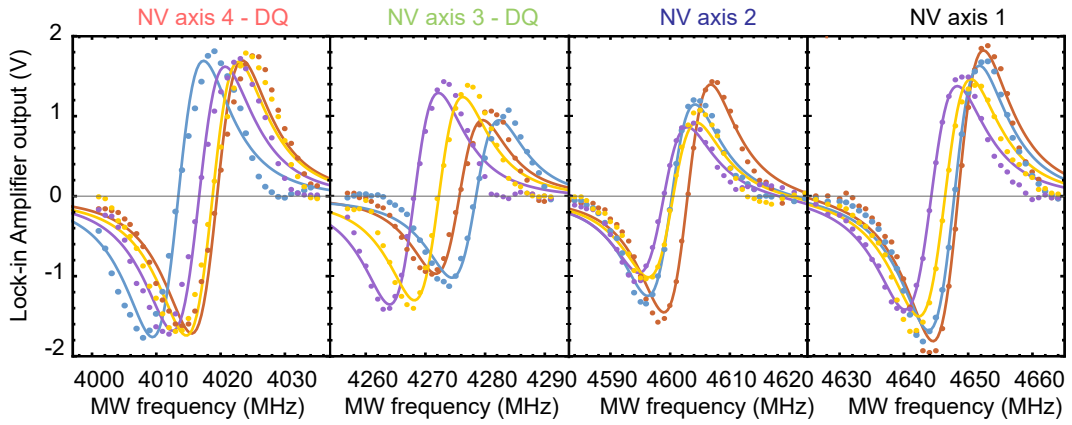

FIGURE 6.5: Example data traces of four optically detected resonances at different position near the center of the Halbach magnet. The resonances appear dispersive due to the use of a modulation technique. The resonances are fitted and their center frequencies are extracted. The four different plots correspond to different transitions indicated above the respective plot. The color of the traces indicate the positions at which the data was taken, as seen in Fig. 6.8.

recorded the demodulated PL from the LIA x-output with a data acquisition system and stored each data set with its respective position. To speed up the acquisition and after determining that no features were left out, we just acquired in total 164 frequency values around the expected position of the resonances. In total a frequency scan to determine the four center frequencies lasted 46 s. This can be dramatically improved by for example applying a frequency lock on the four transitions, respectively.

Figure 6.5 shows an example of collected data in four different points of the scan. The points are noted in Fig. 6.8 (b) with different colors. The four different frequency regions correspond to different kind of transitions as noted above the figures. The FWHM linewidth of the observed features is (11.48 ± 0.14) MHz and therefore much larger than the one given above (0.35 ± 0.02) MHz for a small background field along one of the NV axis. This is due to the strong transverse field component but also caused intentional via MW power broadening. This simplified the lineshape by suppressing the hyperfine features in the spectrum and therefore the analysis routine. We additionally like to note, that the two first of the features are double quantum transitions (DQ), i.e. magnetic transitions from the $m_s = -1$ to the $m_s = +1$ state, normally forbidden, but allowed when transverse magnetic field components are present.

Overall the sensor was moved in steps of 1 mm and 1.5 mm in z and y-direction,

respectively, such that the whole area was covered. The resulting frequency maps of the chosen four resonances can be seen in Fig. 6.8 (a); they show structures corresponding to the strength of the longitudinal (along the NV axis) and transverse (perpendicular to the NV axis) component of the magnetic field for a given diamond lattice axis. The information contained in these plots is more than sufficient to reconstruct all three vector components of the magnetic field at the position of the sensor.

§ 6.5.1 Frequency to vector field conversion

After acquiring MW frequency scans for different positions, the data were fitted with the sum of four derivatives of Lorentzians. The four center frequencies, four amplitudes and a combined linewidth were fit parameters, an example of the data and fits can be seen in Fig. 6.5. By matching these frequencies to the positions of the 3D translation stages we can make frequency maps as shown in Fig. 6.8 (a).

To proceed with the analysis and construction of the magnetic field maps we note that the four different features presented in Fig. 6.5 originate from the different NV orientations in the diamond crystal. The positions of these features are related to the alignment of the magnetic field to the NV axis, as well as its amplitude. If the magnetic field is along the NV axis (longitudinal) we observe the $m_s = 0 \rightarrow m_s = \pm 1$ transitions; if there is an additional magnetic field component orthogonal to the NV axis (transverse), transitions between the $m_s = -1$ and $m_s = +1$ are allowed. We call these double quantum (DQ) transitions. For a given magnetic field direction at the position of the sensor, both, the longitudinal and transverse components of the magnetic field are present. Due to mixing caused by the transverse magnetic field component, the NV gyromagnetic ratio depends on the background field strength.

As a result, to match the above frequencies to magnetic fields we create four vectors describing the NV axes. We use parameters β to describe the angle between NV axis and magnetic field and Ω for the field strength. With these parameters we derive a formula which describes the transition frequencies of the spin states, from $m_s = 0$ to $m_s = -1$, as well as $m_s = -1$ to $m_s = +1$ [94]. Here, we neglect strain and electric field effects.

The frequency of the resonances depends on the magnitube of the magnetic field B_M, as well as the angles θ and ϕ of the diamond orientation with respect to the

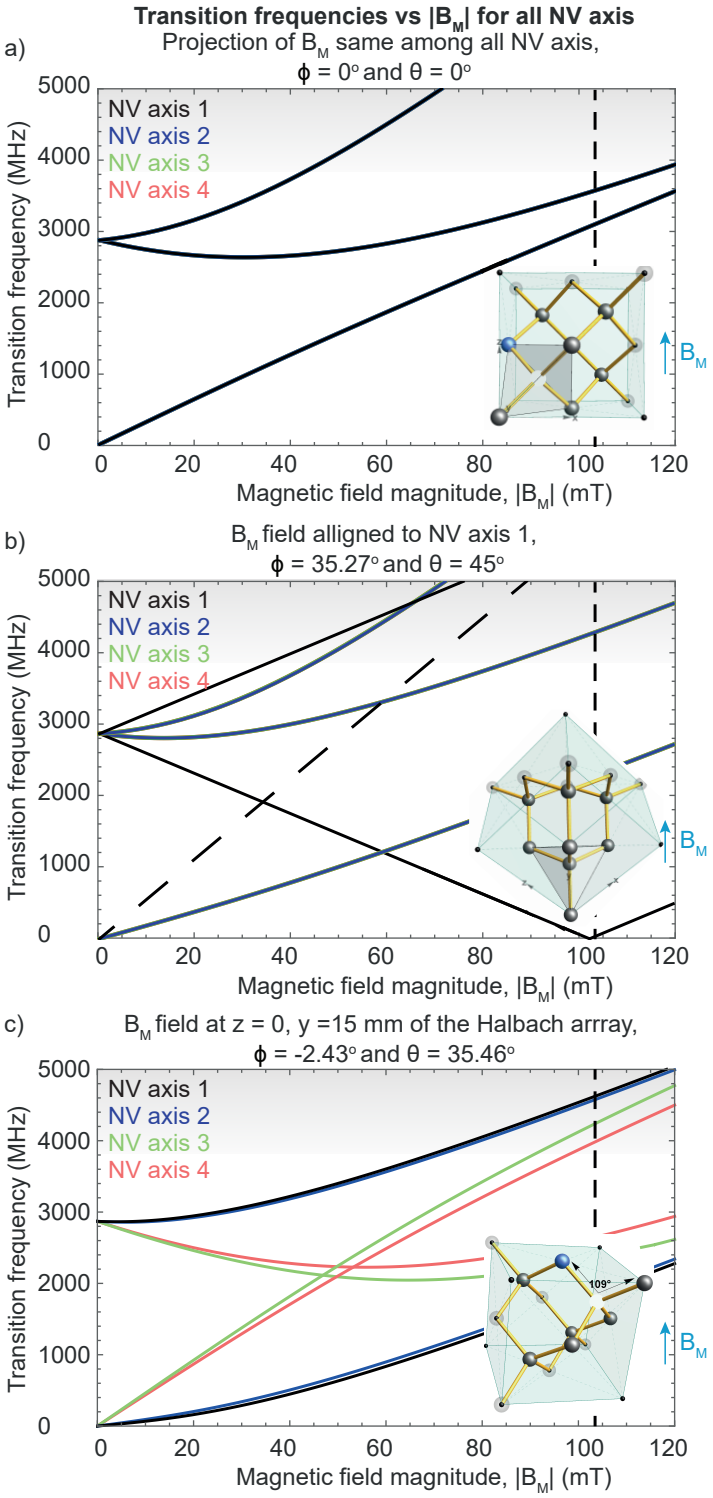

FIGURE 6.6: Transition frequencies as a function of $|B_M|$. The traces of the four different NV axes are depicted with colours consistent with those of Fig. 6.4. The gray area represents our scanning range, the vertical dashed line shows the mean field strength inside the Halbach magnet. a) For a magnetic field perpendicular to the (100) plane: all transitions overlap since the magnetic field projection is the same among all axes. b) For a magnetic field perpendicular to the (111) plane of a diamond: the magnetic field is aligned along NV axis 1, and the magnetic field projection is the same for the other three axes. The slanted dashed line for NV axis 1 corresponds to the frequency of the DQ transition which in this case due to the absence of transverse magnetic fields is not allowed. c) For a magnetic field configuration inside the Halbach magnet.

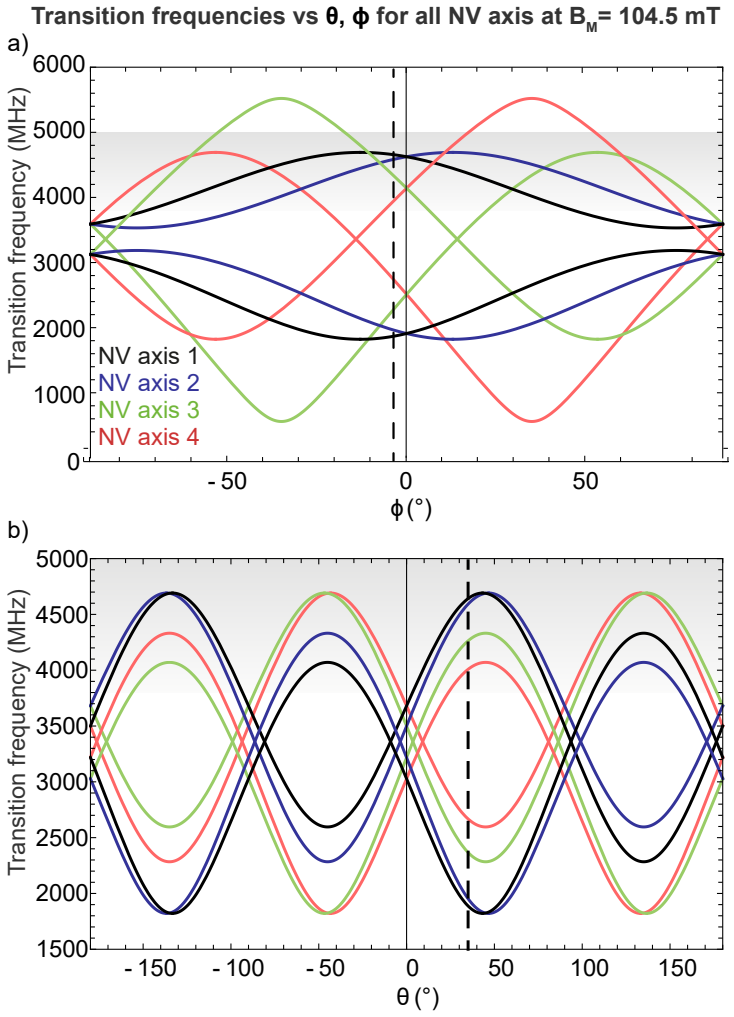

FIGURE 6.7: Simulated transition frequencies as a function of angles θ and ϕ for the average magnetic field magnitude $|B_M| = 104.5\,\mathrm{mT}$ inside the Halbach magnet. The gray area represents our frequency scan range, the vertical dashed line indicates the respective average angle of all the measurements. a) Transition frequencies as a function of angle θ for a fixed angle $\phi = -2.43°$. b) Transition frequencies as a function of angle ϕ for a fixed angle $\theta = 35.46°$.

magnetic field. Figure 6.6 shows the resonance frequency dependence as a function of magnetic field magnitude for different fixed angles θ and ϕ. Figures 6.6 (a,b) represent a magnetic field perpendicular to common diamond surface cuts, (100) plane for (a) and (111) plane for (b), (c) depicts a configuration inside our Halbach magnet. Figure 6.7 shows the dependence of the transition frequencies on the angles θ and ϕ for a magnetic field matching the mean magnitude inside the Halbach magnet. In Fig. 6.7 (a) ϕ = -2.43° and θ is varied. In Fig.6.7 (b) θ = 35.46° and ϕ is varied.

In both Fig. 6.6 and Fig. 6.7 the four different NV axes are depicted with colours matching those in Fig. 6.4. We observe that in Fig. 6.6 (a) all the transitions overlap, as the projection of the magnetic field is the same among all axes. In Fig. 6.6 (b) the magnetic field is aligned along the NV axis 1, and its projection is the same for the other three axes, which appear overlapped in the figure. The dashed line for NV axis 1 corresponds to the frequency of the DQ transition which in this case is not allowed, as there is no transverse field on NV axis 1. Figure 6.6 (c) represents a case we encounter while measuring the field inside our Halbach magnet. In Fig. 6.7, we note the symmetry between NV axes 1,2 and 3,4 which arises because of the crystallographic structure of the diamond. We can use the information of the above plots to translate the frequency into magnetic field.

After identifying the possible transition frequencies, we use a numerical method to translate the frequencies into magnetic field direction and strength. For this method we restrict the magnetic field strength values to within 10% of what the estimated magnetic field produced by our Halbach array is. Once the magnetic field is calculated for all the different frequencies we express it in polar coordinates. When the initial values for direction and magnitude of the field are approximately known, we find that the reconstruction is unique. We choose B_M to describe the strength of the field, angle θ the latitude angle with respect to the x-axis and ϕ the longitude angle as shown in Fig. 6.4 (a). Finally, we make a list of these parameters and plot them as shown in Fig. 6.8 (b). In Fig. 6.8 (b) we included four different coloured circles to represent the positions at which data for Fig. 6.5 are taken. The measured averages of angles θ and ϕ in the central 10×5 mm^2 (y-x) of the Halbach magnet are $(-2.433 \pm 0.009)^\circ$ and $(35.764 \pm 0.018)^\circ$, respectively, which is consistent with the orientation of the diamond lattice (cf. Fig. 6.4) relative to the coordinate system of the magnet.

Conclusion and Outlook

We constructed two fiberized NV based magnetic field sensors. The sensors feature sub-nT/$\sqrt{\text{Hz}}$ magnetic field sensitivity with high PL-to-pump-light ratio. The components used to make the sensors are commercially available which makes their construction easy and reproducible. The design for the Mainz sensor was made in such a way as to allow free access to the front side of the diamond as well as for robustness, portability, and small size.

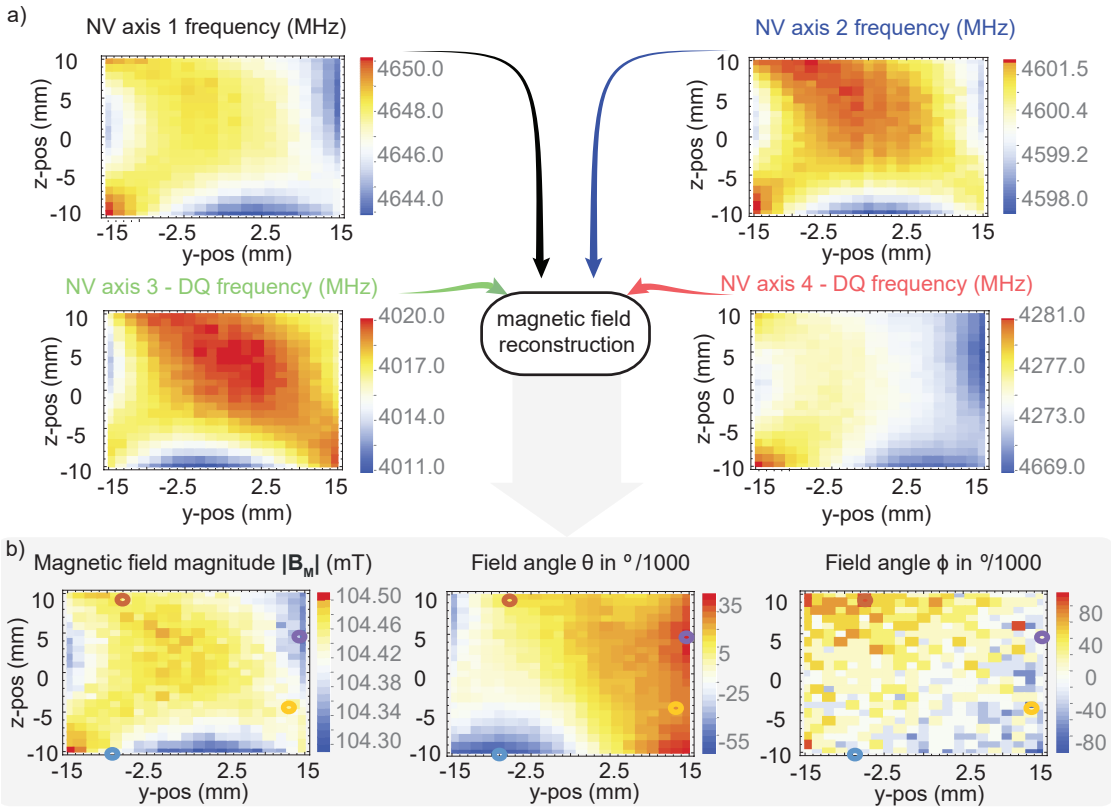

FIGURE 6.8: Figure adapted from Ref. [114]. (a) Spatially resolved frequency maps of the individual resonances from Fig. 6.5 (a). (b) The data collected are used to reconstruct the vector magnetic field in spherical coordinates as defined in Fig. 6.4 (a), the four colored circles note the positions at which data for Fig. 6.5 are taken.

With one of the main challenges for NV magnetometry, especially fiberized, being the low photon-collection efficiency, which leads to poor photon-shot-noise limited sensitivity, the 0.5% PL-to-pump-light ratio collection efficiency, demonstrated in the Mainz sensor, can be used to achieve even higher sensitivity, if the effect of other noise sources is minimized. This ratio could also be further optimized by implementing side collection on the diamond [15, 63], as well as highly reflective coatings on the opposite (front) side of the diamond. These features were not implemented in this sensor in order to keep all of its components commercial and easily accessible.

The access to the front side of the diamond allows for close proximity to magnetic field sources, which in turn leads to high spatial resolution. The proximity is currently limited to about 300 µm by MW wire on top of the diamond. It could be optimized further by using a thinner diamond sample, a sample with shallow implanted NV centers or a thinner MW wire such as, for example, a capton-tape

printed circuit board, all depending on the intended application, as these changes influence the sensitivity of the sensor. Such optimization would be especially beneficial for measurements of dipole fields or measurements that require high spatial resolution.

The robustness and portability of the sensors also make them attractive for mapping larger areas, or on-the-move measurements of magnetic fields. These features combined with the small size of the sensors suggest a use for measuring in hard-to-access places or small areas where maneuverability of the sensor would be required, e.g. endoscopic measurements inside the human body.

As a demonstration of the Mainz sensor we measured the magnetic field of a custom-designed Halbach array. For these measurements, the small fiberized diamond sensor showed a mm-scale spatial resolution, angular resolution of the magnetic field vector extracted in the measurements were 9×10^{-3} degrees and 18×10^{-3} degrees for angles θ and ϕ, respectively. We note here, that the corresponding displacement due to such a rotation of the diamond sensor (considering a (0.5×0.5) mm^2 square cross section) could optically not be resolved.

§ 6.6 Acknowledgment

This work is supported by the EU FET-OPEN Flagship Project ASTERIQS (action 820394), the German Federal Ministry of Education and Research (BMBF) within the Quantumtechnologien program (grants FKZ 13N14439 and FKZ 13N15064), the Cluster of Excellence "Precision Physics, Fundamental Interactions, and Structure of Matter" (PRISMA+ EXC 2118/1) funded by the German Research Foundation (DFG) within the German Excellence Strategy (Project ID 39083149). We acknowledge Fedor Jelezko for fruitful discussions.

§ 6.7 Author contribution

For the work presented in this chapter, I constructed and optimized the fiberized sensor made in Mainz. The data collected for the Mainz sensor, was acquired by Dr. Huijie Zheng and Dr. A. Wickenbrock. Dr. A. Wickenbrock and I led the analysis of the data. I constructed the figures, with the exception of Fig. 6.8 and with the help of the rest of the co-authors, I co-wrote the manuscript.

§ 7

Towards endoscopic measurements with NV centers

§ 7.1 Abstract

We present our efforts in the construction of a magnetic field sensor for endoscopic measurements using nitrogen-vacancy centers. Multiple people collaborated for the creation of the sensor, with major contribution being made by me, Dr. Arne Wickenbrock and Dr. Geoffrey Iwata. The sensor features $7\,\mathrm{pT}/\sqrt{\mathrm{Hz}}$ magnetic sensitivity, with $5\,\mathrm{pT}/\sqrt{\mathrm{Hz}}$ photon-shot noise-limited sensitivity. It consists of three main parts, each of them designed for a specific purpose: A high-reflective-coated diamond optical assembly, a copper pipe with gold coating and a 90°-parabolic aluminium mirror. Becides the three main parts we also use a photodetector coated with an optical notch filter for 532 nm with an accompanying electronic circuit and a custom designed flexible microwave delivery circuit. Each of the parts is described in its own section. The purpose of the diamond optical assembly is to improve photon collection and heat management of the system. The copper pipe further aids in heat management and serves as a light guide for the emitted diamond photoluminescence. The 90°-parabolic mirror includes a lens, which collimates the pump light and guides it through the copper pipe, while at the same time directing the fluorescent light produced by the diamond to the photodetector. The flexible microwave delivery circuit allows delivery of microwaves to the diamond in a configuration that enables zero-field magnetometry with nitrogen-vacancy centers.

§ 7.2 Introduction

One project that is still ongoing at the time of writing of this thesis is the construction of a high-magnetic-field-sensitivity nitrogen-vacancy (NV) sensor for endoscopic measurements. It is a project I plan to continue after graduation and this chapter details the efforts on it so far. The goals for this sensor are threefold. First the magnetic field sensitivity should be at the level of $1\,\mathrm{pT}/\sqrt{\mathrm{Hz}}$. Second, the sensor should have a miniaturized footprint with a diameter $< 10\,\mathrm{mm}$. Third, the temperature of the sensor should not be raised by more than a couple of °C above human body temperature, so that the design can be used endoscopically. With our previous work, we were able to achieve sensitivity values of $22\,\mathrm{pT}/\sqrt{\mathrm{Hz}}$, limited by photon-shot noise [26]. As seen in Eq. 2.6 to improve on this limit we have to increase photon collection or improve the contrast-to-linewidth ratio of the resonance we are addressing during measurement. We optimize the photon collection by the geometry of our design and while contrast-to-linewidth ratio can be optimized for a given diamond sample, it will be ultimately limited by the diamond sample used. To address this, we acquired a new sample, produced by Prof. J. Isoya, through collaboration with Prof. J. Wrachtrup. The sample is a 99.97% ^{12}C, (111)-cut diamond single crystal, with dimensions $0.71\,\mathrm{mm} \times 0.69\,\mathrm{mm}$ and a thickness of 0.43 mm. It is laser-cut from a ^{12}C-enriched diamond single crystal grown by the temperature-gradient method at high pressure (6.1 GPa) and high temperature (1430 °C). A metal solvent containing a nitrogen getter and carbon powder prepared by pyrolysis of 99.97% ^{12}C enriched methane as a carbon source were used. The sample was irradiated with 2 MeV electrons from a Cockcroft-Walton accelerator to a total fluence of $1.8 \times 10^{18}\,\mathrm{cm}^{-2}$ at room temperature, and annealed at 800 °C for 5 h. This source diamond was reported to have 3-ppm initial nitrogen and 0.9-ppm NV-after conversion, measured by electron-paramagnetic-resonance techniques. We refer to this sample as S1. By performing optically detected magnetic resonance (ODMR) measurements on it we are able to achieve a contrast of 1 % with a linewidth of 100 KHz, for comparison our $22\,\mathrm{pT}/\sqrt{\mathrm{Hz}}$ sensor featured a diamond which had an ODMR linewidth of 6 MHz.

§ 7.3 Optical assembly

As already discussed in Chapter 2 and Chapter 3 one of the greatest challenges that NV-based sensors face is collecting the produced photoluminescence (PL) from the

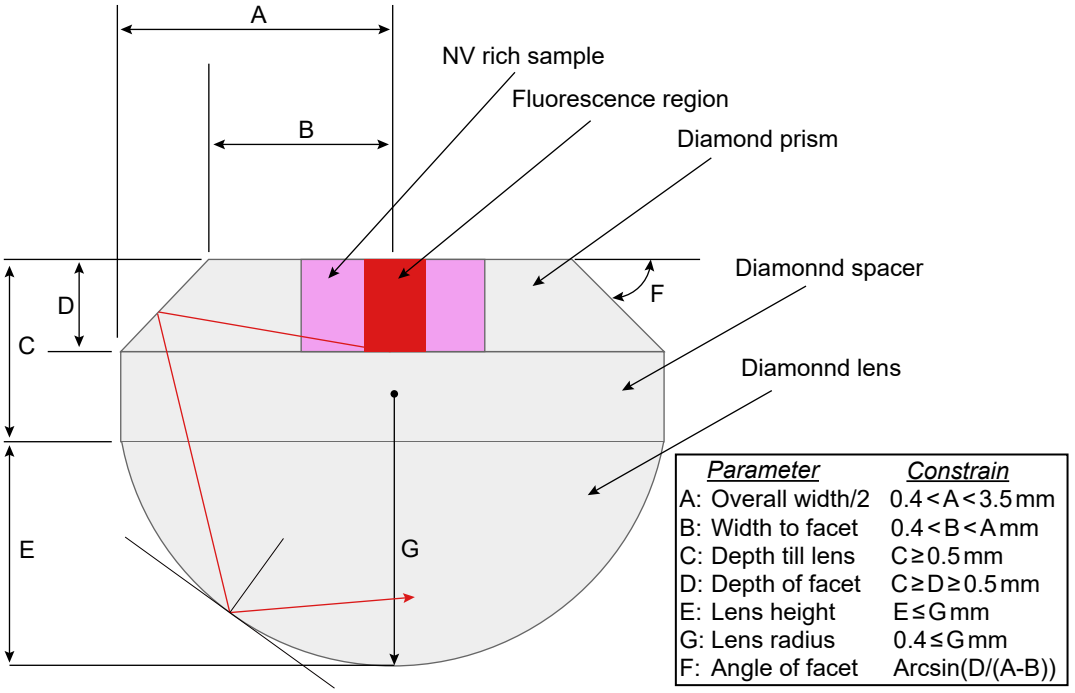

FIGURE 7.1: Schematic of parameters to vary for optical assembly optimization. The different parameters are noted with capital letters in the figure, with a legend at the bottom-right showing constrains. Sample fluorescence is shown emitted from the red fluorescent area, of the pink-coloured NV rich diamond sample, and reflected throughout the array.

NVs after illumination with green light. To address this problem we constructed an optical assembly which aimed to maximize the collected PL. We choose to make the optical assembly with diamond, to avoid change in index of refraction between the NV containing diamond (S1) and the rest of the collection optics of the assembly. Another benefit of choosing diamond is the high thermal conductivity of the material ($2200\frac{\mathrm{W}}{\mathrm{m}\cdot\mathrm{K}}$), which aids us in our goal of keeping the sensor bellow 37 °C. To optimize the design for PL collection we vary a plethora of different parameters and perform ray tracing simulations using COMSOL Multiphysics.

A list of parameters we accounted for can be seen in Fig. 7.1, the different parameters are noted with capital letters in a legend at the bottom right of figure. The legend also includes limitations or constrains for some of the parameters. Some of the values, e.g., radius of hemi-spherical lens, G, ended up being selected based on what is commercially available, while others e.g., E, angle facet of the prisms, where optimized based on the COMSOL simulations. The red area in Fig. 7.1 represents the fluorescing area of S1 after illumination with green light, which is omitted form the figure. Sample PL is shown emitted from the red fluorescent

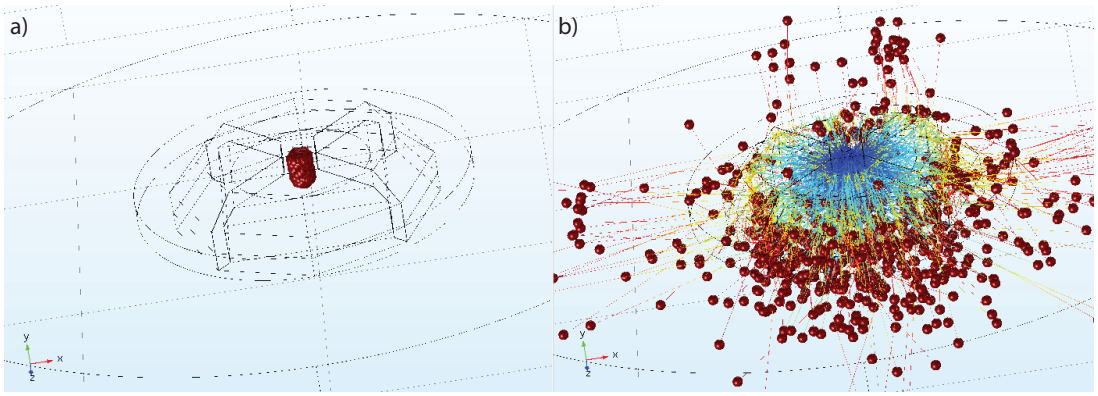

FIGURE 7.2: a) Multiple 637 nm rays are generated in the center of the diamond optical assembly b) the rays are propagated in random directions reflecting throughout the optical assembly.

area, of the pink-coloured NV rich diamond sample, and reflected through the assembly.

To preform the simulations we design the optical assembly with the aid of a computer-aided design(CAD) program and then import it into COMSOL Multiphysics. Then, we set the refractive index for the materials and in some cases apply coatings to the different surfaces.

We generate more than 1000 rays at the center of the array, at the fluorescing area, and we let the rays propagate at random directions, tracing them throughout the optical assembly. We then create a surface 5 mm bellow the array and measure the number of rays reaching it at an incident angle of $< 80°$, which is the acceptance angle of our photodetector (PD). An example of the first steps of the simulation can be seen in Fig. 7.2. We then change one of the assembly parameters seen in Fig. 7.1 and repeat the process comparing the number of collected rays at the end.

An example is presented in Fig. 7.3. The data is taken for change in parameter G, the radius of the hemispherical lens. We see that, with the the physical constrains taken into account, there is a local maximum, for the no high reflective coating case, but this maximum is not present after we apply the coating. The maximum is ~ 1.5 mm, which is commercially available through the company Dutch Diamonds.

Figure 7.4 depicts the diamond optical assembly, the top left side of the figure depicts the side that would be closest to the magnetic field source during measurements, we refer to this side as front side. The top right depicts the side from where the PL produced by the diamond would be collected, we refer to this as the back side of the assembly. The assembly consists of seven parts all made out

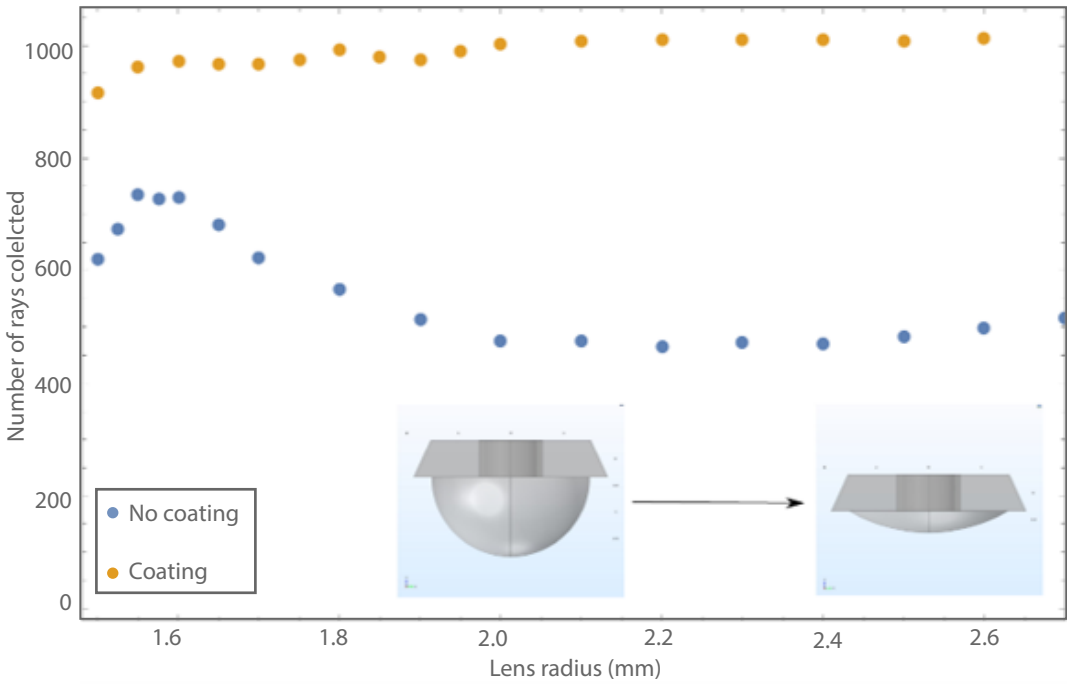

FIGURE 7.3: Number of collected rays as a function of lens radius, while the lens width is constrained to two times the width to the facet length (B). The legend at the bottom left notes the cases for high-reflective coating and no high-reflective coating on the front side of the assembly. The insert at the bottom right shows an example of the assembly with lens radius 1.5 mm and lens radius 2.6 mm. Because of the lens width being constrained a big part of the 2.6 mm radius lens has been cut, making the lens height (E) of this case smaller than the 1.5 mm case.

of diamond. Sample S1, which is the NV containing diamond of the assembly (labeled as a). Surrounding it are four identical diamond prisms (labeled b), that are cut at an angle of 45° with regards to the assembly's front surface, due to this angle PL side collection can be achieved. Bellow the prisms is a 7 mm diameter diamond ring (labeled c) with a central hole of 1.5 mm radius and two 0.3 mm holes, centered on its rim. The ring mainly acts as a heat bridge between the assembly and the copper pipe, with the central hole made for the placement of the next part and the outer-rim holes allowing for access of microwave (MW) coaxial cables to the front side of the assembly. Finally, a lens (labeled d) is placed inside the central hole of the ring, in contact with S1. The lens is manufactured from a half-spherical, 1.5 mm, diamond lens, 0.5 mm are removed from the base of the half-sphere, so that the center of curvature of the lens corresponds to the front side the assembly making the height of the assembly $\sim$1.5 mm. The top of the half-sphere is also flattened in order to create a 0.2 mm diameter surface, from which the collimated pump light beam can be guided into the assembly, without change

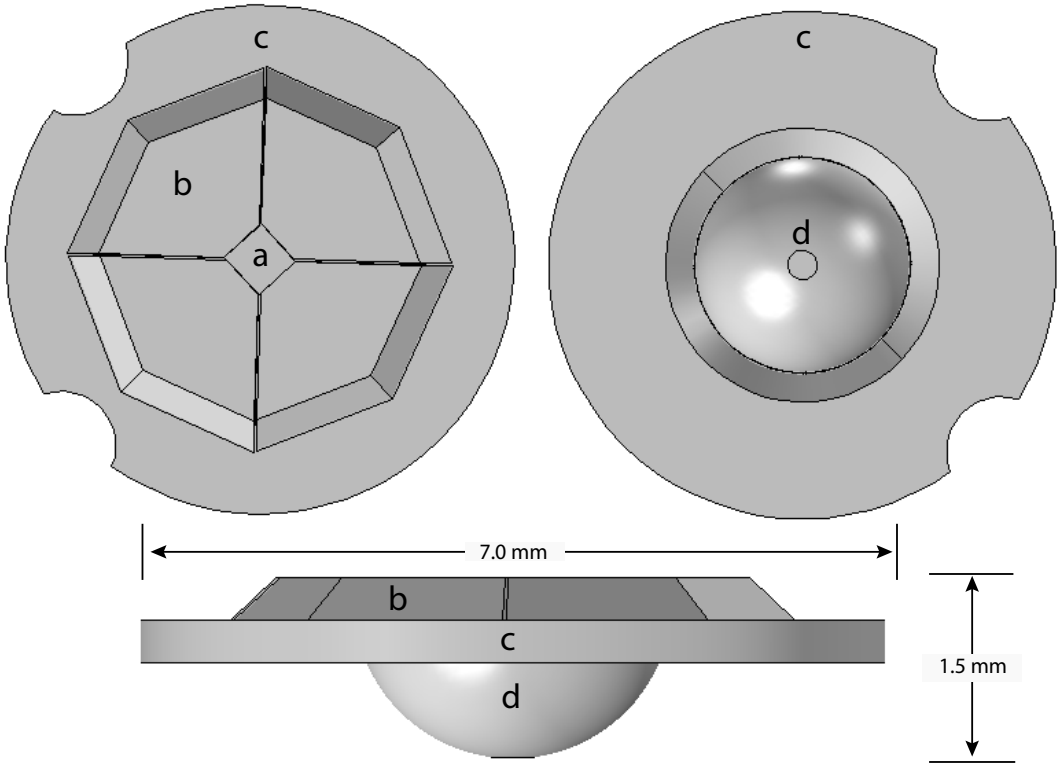

FIGURE 7.4: Schematic of diamond optical assembly, the left side depicts the front and the right side the back of the assembly, at the bottom a side view of the assembly is visible. The assembly consists of seven parts; the NV containing diamond (labeled a), four prisms identical prisms (b), a ring (c) and a lens (d)

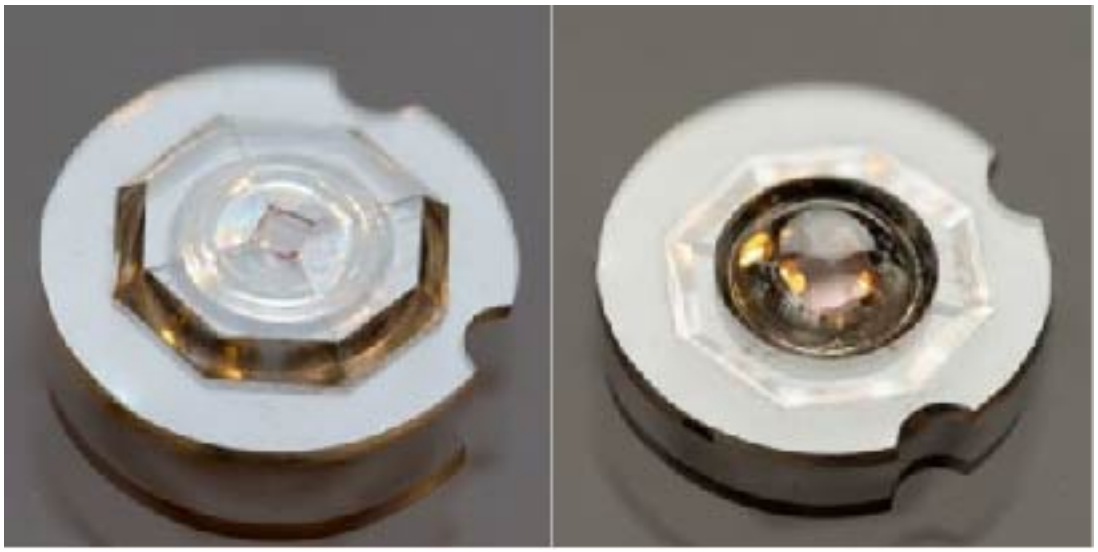

FIGURE 7.5: Constructed diamond optical assembly, the left side depicts the front side of the optical assembly (before HR coating) and the right side the back of the assembly.

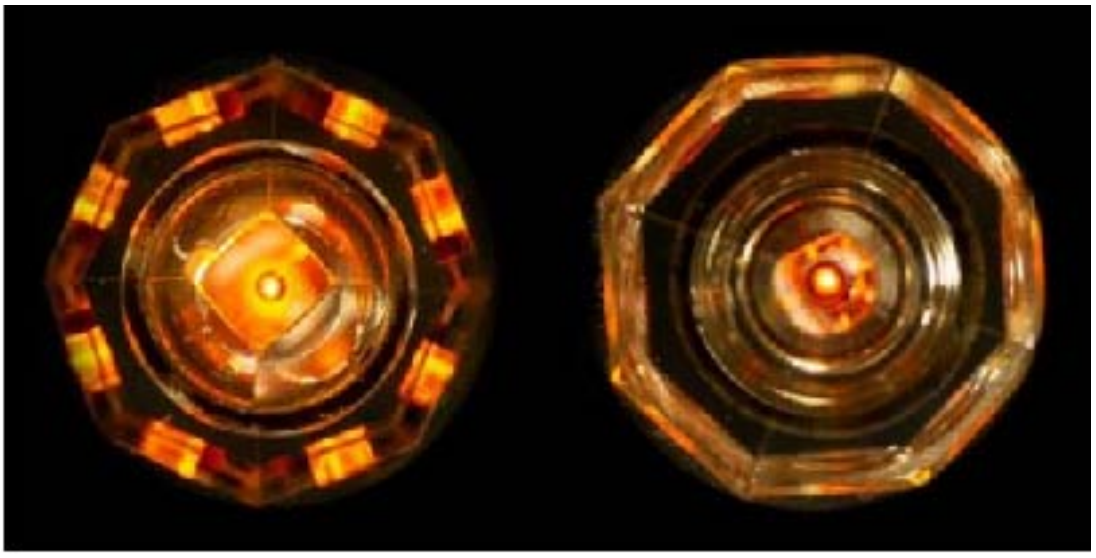

FIGURE 7.6: Red fluorescence imaged from the diamond optical assembly of Fig. 7.5 under illumination with a 532 nm laser. The image is taken through a 532 nm notch filter and before HR coating is applied to the optical assembly.

in the beam radius. The purpose of these parts is two-fold: First, to improve photon collection, due to the geometry of the design and the matching indices of refraction. Second, to act as high heat-conductivity materials which distribute the heat generated by the pump light and guide it outwards, away from the NV containing diamond and towards the copper pipe.

A photograph of the constructed array can be seen in Fig. 7.5. Figure 7.6 depicts the PL imaged from the diamond optical assembly of Fig. 7.5 under illumination with a 532 nm light. The image is taken through a 532 nm notch filter , before high reflective (HR) coating is applied to the optical assembly. In the picture we see the difference in light collected from the front and the back side, which is quantified as a factor of 5.4 more red photons collected from the back side. We notice eight (two per prism) images of S1 at the prisms angled surfaces. In all of the images a brighter red fluorescence line can be seen, which is attributed to the 532 nm pump light travelling through the sample. The intensity change of that line is due to absorption of 532 nm light and thus pump-intensity reduction, when the light is passing through the sample. Comparing the front and the back side we note the effect of the diamond lens, which magnifies the image of S1 in the center of the optical assembly. Finally, if the alignment of the 532 nm light to the optical assembly is correct as in Fig. 7.6, one can see a dark ring on the center of the optical assembly, around the light source that corresponds to the excitation light. This dark ring is the edge of the 0.2 mm flattened area on the top of the lens, which is made to avoid focusing of the incident 532 nm beam.

After these images were taken and the effectiveness of the design was confirmed and quantified, the diamond assembly was shipped to Helia Photonics Ltd, where silver coating of $\sim 92\%$ reflectivity, for the diamond fluorescence wavelengths, was applied to the front side of the assembly. The HR coating doubles the excitation path of the pump light and can improve the PL collection further, by collecting the light that is emitted outwards from the front side of the assembly.

§ 7.4 Copper pipe

A schematic of the copper pipe can be seen in Fig. 7.7. This part is made from a 50 mm long copper pipe, with an outer radius of 9.5 mm and inner radius of 6.0 mm. The length is chosen so that the magnetic noise, caused by the PD circuit at the end of the pipe, has decayed significantly when it reaches the diamond. The outer diameter is chosen to be similar to other endoscopes and the inner diameter is chosen after COMSOL simulations to optimize heat conductivity and photon collection, while at the same time allowing the optical assembly to fit into the pipe. Further processing to the pipe is done by the Johannes Gutenberg Universität (JGU) workshop. Two 1.5 mm diameter holes (labeled a), which allow access of the MW coaxial cables, through the pipe, and to the front side of the optical array. Two M1 holes (b) are drilled into one side of the array, their purpose is to allow the parabolic mirror to be screwed onto the array. On the same side a cutout (e) is made which allows for the PD and its circuit to be slotted in the copper pipe. On the other side of the array four M0.7 holes (c) are drilled that allow the optical assembly to be clamped onto the copper pipe with a use of a small ceramic ring. Finally a cutout of ~ 7 mm diameter (d) is made so that the optical assembly can be placed onto the pipe. The pipe is made out of copper because of its heat conductive properties and the inside of it is further coated with gold due its high broadband reflectivity. A photograph of the copper pipe, after it is coated is seen in Fig. 7.8

§ 7.5 Parabolic mirror

A schematic of the parabolic mirror can be seen in Fig. 7.9. It is constructed from a parabolic mirror (MPD00M9-M01, Thorlabs). The mirror is a 90° off-axis parabolic mirror, with protected gold coating and focal length of 15 mm. Further

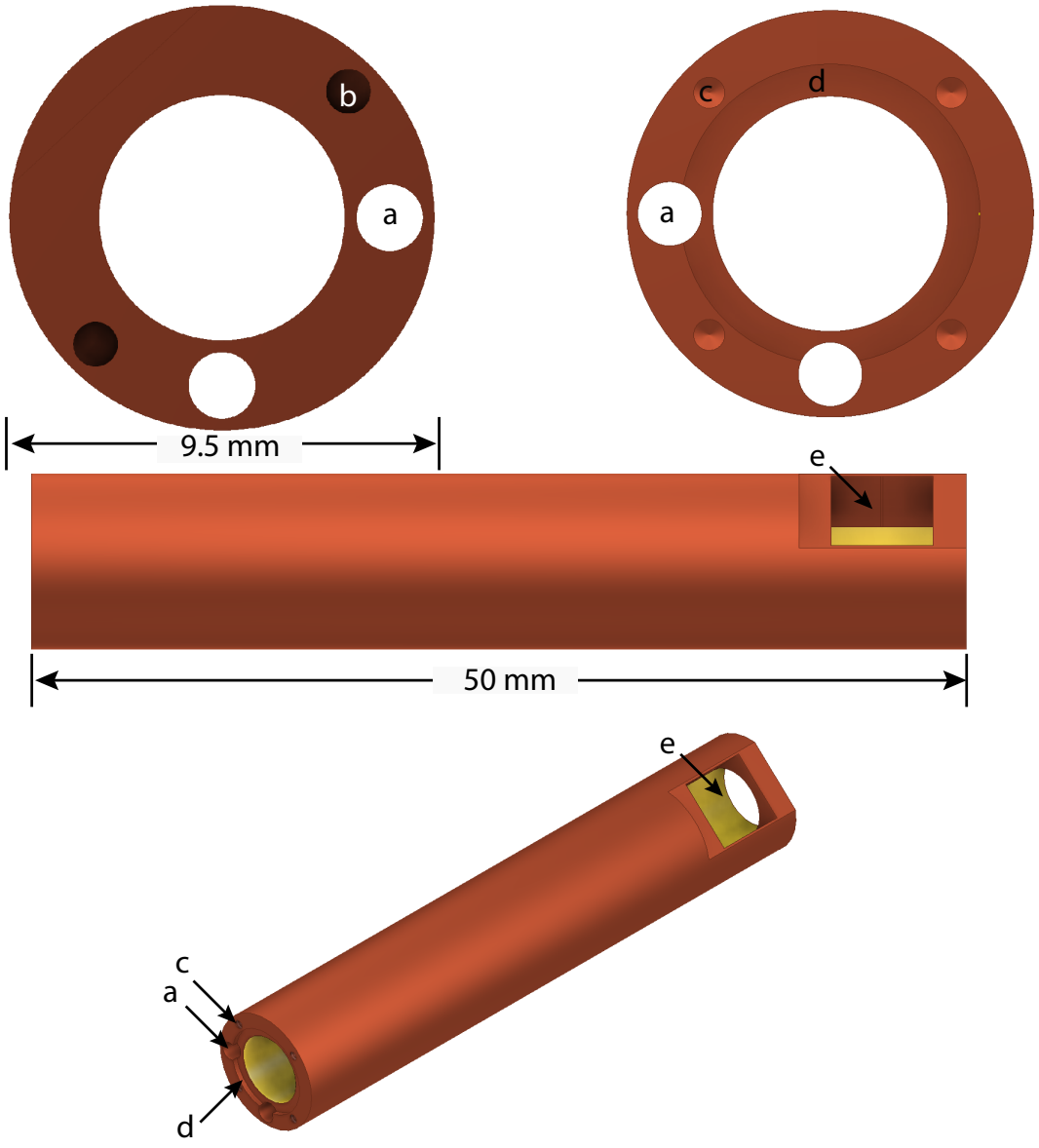

FIGURE 7.7: Schematic of the copper pipe from different point of view. The design is a copper pipe with holes for MW coaxial cables (labeled a), The part is constructed by machining a MPD00M9-M01, Thorlabs component.

processing to the parabolic mirror is done by the JGU workshop. The part is processed to include a hole in the back (labeled a) where a 4 mm focal length lens can be placed. The purpose of the lens is to collimate the 532 nm exiting a fiber to a parallel beam with 0.2 mm diameter. The lens can be secured to the holder with an M1.5 screw, centered through the top of the holder (entered through b). Two M1 screws on the side of the holder (entered through c) allow for the holder to be attached to the copper pipe. A central 0.3 mm diameter hole (labeled d) allows for the collimated light to enter into the copper pipe, the size of the hole

FIGURE 7.8: Copper pipe after electroplating as seen from different points of view.

is selected so that it does not induce any aberration to the incoming light, while at same time not reducing the reflective area surface (labeled e) of the parabolic mirror significantly. Two cutouts at the rim of the mirror (labeled f) allow for coaxial cables to pass through the holder and enter the copper pipe. The bottom of the holder is flattened so a custom made circuit board with a PD can rest on top of the holder. A photograph of the finished piece can be seen in Fig.7.10.

§ 7.6 Assembly

The three parts of the endoscope described above are attached together as seen in Fig. 7.11. The parabolic mirror is screwed onto the copper pipe through the holes labeled a. Holes b can be used so that coaxial MW wires can pass through the copper tube and access the front side of the optical assembly. The optical assembly is clamped to the copper pipe with the help of a ceramic ring, not shown in the picture, which is screwed onto the pipe using holes c.

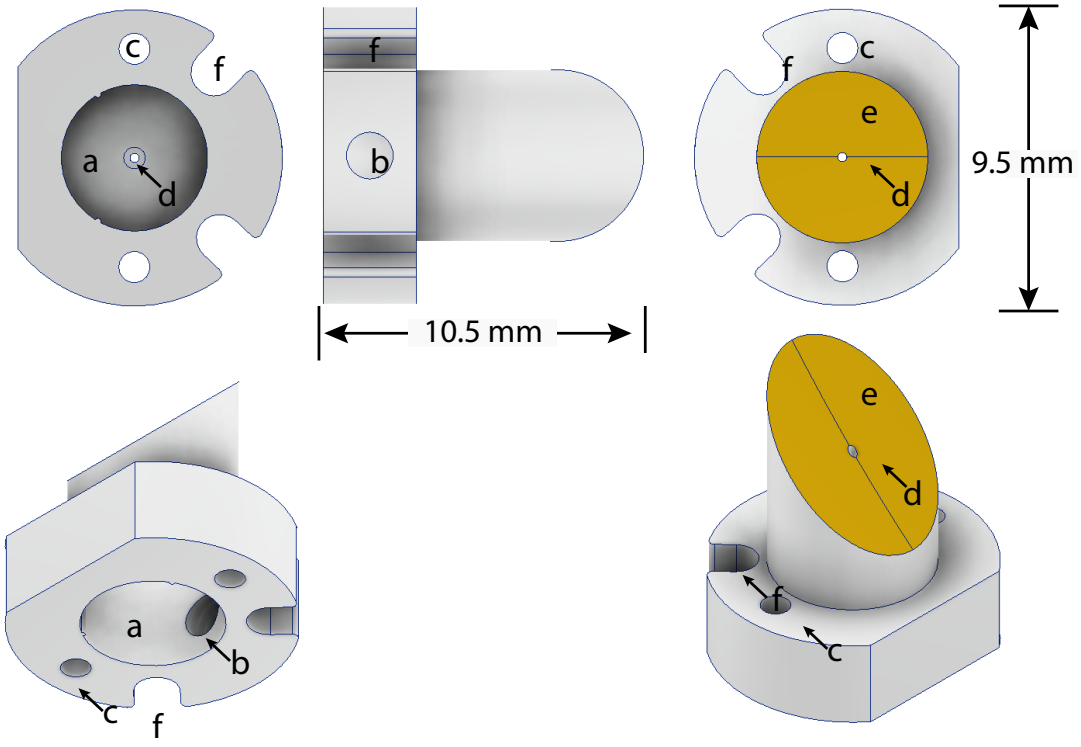

FIGURE 7.9: Schematic of parabolic mirror from different points of view. The part is constructed by machining a MPD00M9-M01, Thorlabs component.

FIGURE 7.10: Photograph of the MPD00M9-M01, Thorlabs parabolic mirror after processing from the JGU workshop.

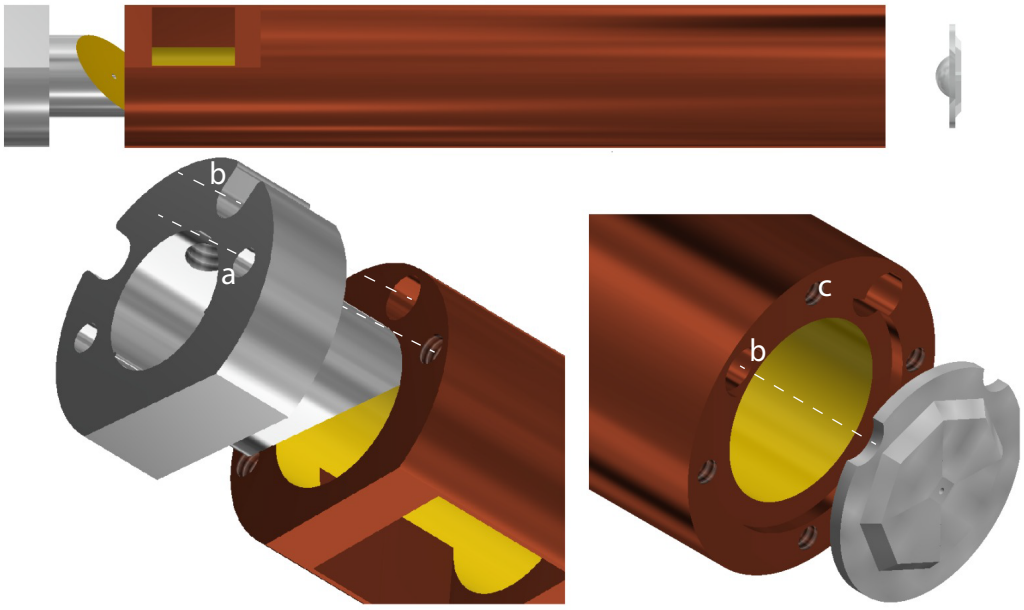

FIGURE 7.11: Schematic of the three major different sensor parts for assembling

FIGURE 7.12: Picture of the sensor with the three major pieces attached to one another. The left side shows the front side of the sensor and the right side shows the back side of the sensor.

The left side of Fig. 7.12 shows a picture of the front side of the sensor, i.e. the side that would be closest to the magnetic field source. The right side shows a picture of the back side, from where the pump light can enter the array. For initial testing, a fiber delivering the pump light can be aligned with respect to the sensor with the use of other components, not currently incorporated in the sensor. Once the endoscope sensitivity has been optimized and the current design effectiveness confirmed, additional components will be included in the parabolic mirror to attach and align the fiber.

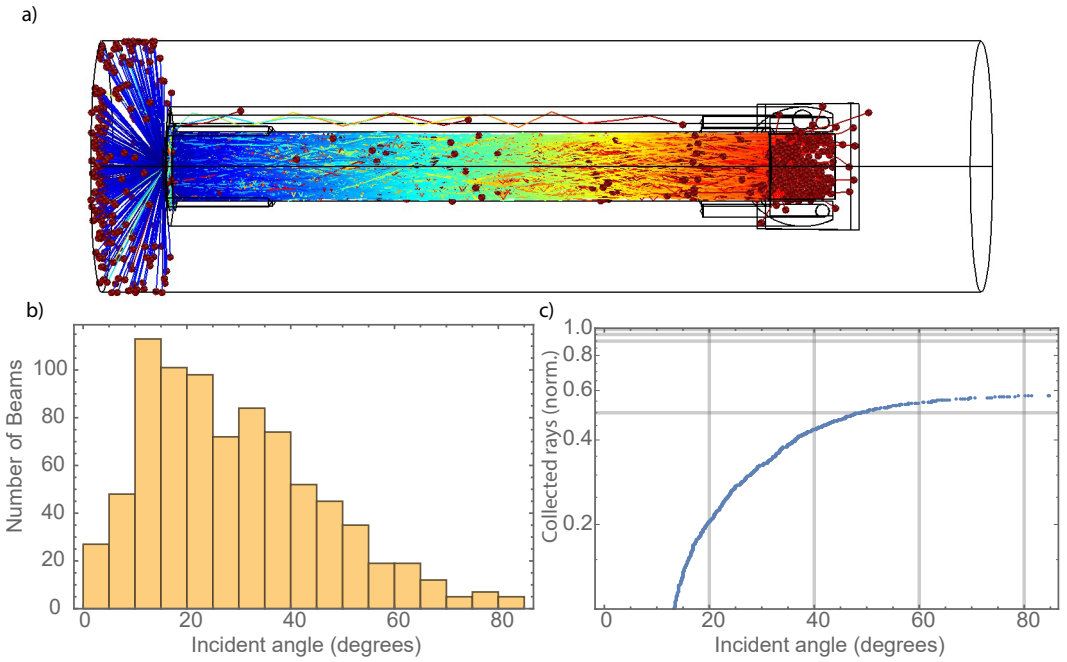

FIGURE 7.13: a) Screenshot from COMSOL simulation. One thousand rays are produced and propagated in throughout the assembly. b) Number of rays reaching the designated PD area as a function of their incident angle at contact. c) Normalized collected rays as a function of incident angle at the designated area for the PD.

Before conducting measurements in the lab, we performed simulations to estimate the photon-collection efficiency of the assembly and its heat managing properties.

To perform the photon-collection simulations, we create 1000, 637 nm rays at the fluorescing area of the diamond and let them propagate at random directions. We include HR silver coating on the front side of the array, as well as HR gold coating on the inside of the copper pipe and the parabolic surface of the mirror. We add a $5.0 \times 5.0\,\mathrm{mm}^2$ area at the designated spot for the PD, and we count the rays arriving there at an incident angle of $< 80°$. An example simulation can be seen in Fig. 7.13. From the simulations about 60 % of the produced rays are detected at the PD designated area.

For the heat-management simulation, we use the assembly geometry, connected to a heat sink at room temperature via a 1 mm diameter, 2 m long copper wire. The assembly is being heated via the green-pump laser at 1 W power, the heat is deposited at the front surface of the optical assembly. The simulations confirm that the assembly will not reach temperature above 37 °C.

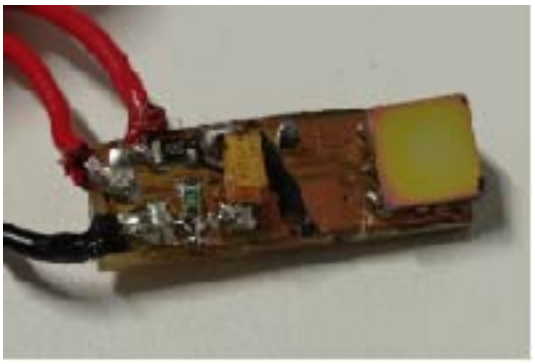

FIGURE 7.14: Coated PD and PD circuit used for the sensor.

§ 7.7 Photodiode

The PD used for PL detection, required a spectrally selective reflective coating which is applied by our collaborator in Bosch, Dr. Robert Rölver. The coating suppresses green light by nearly five orders of magnitude, while leaving PL unaffected.

The design for the PD circuit was led by Muhib Omar. The bandwidth requirement for the PD is selected to be in the range of 10 kHz. This bandwidth would allow circumventing the necessity of using a transimpedance-amplifier circuit and allow voltage readout from the change in photocurrent over an appropriately chosen resistor. The use of fewer components allows us to remain photon-shot-noise limited, instead of Johnson-noise limited, for the specified PL range, it also allows us to stay within the bandwidth despite the internal capacitance of the PD sensor. The resistors chosen are low-noise thin metal-film resistors. The uncoated PD sensor is a Hamamatsu S13957-01 chosen because of its large photosensitive area of $5.0 \times 5.0\,\mathrm{mm}^2$. The large surface area is useful since the optics used do not perfectly collimate the PL. The bias to the PD is applied externally via battery. A picture of the PD can be seen in Fig. 7.14.

§ 7.8 MW circuit

The design is made with COMSOL and was led by Dr. Geoffrey Iwata. The simulations aim to optimize the homogeneity of the MW field produced by the circuit in the interrogated diamond volume. To achieve the desired circularly polarized MW field, necessary for zero-field measurements, two of the circuits have

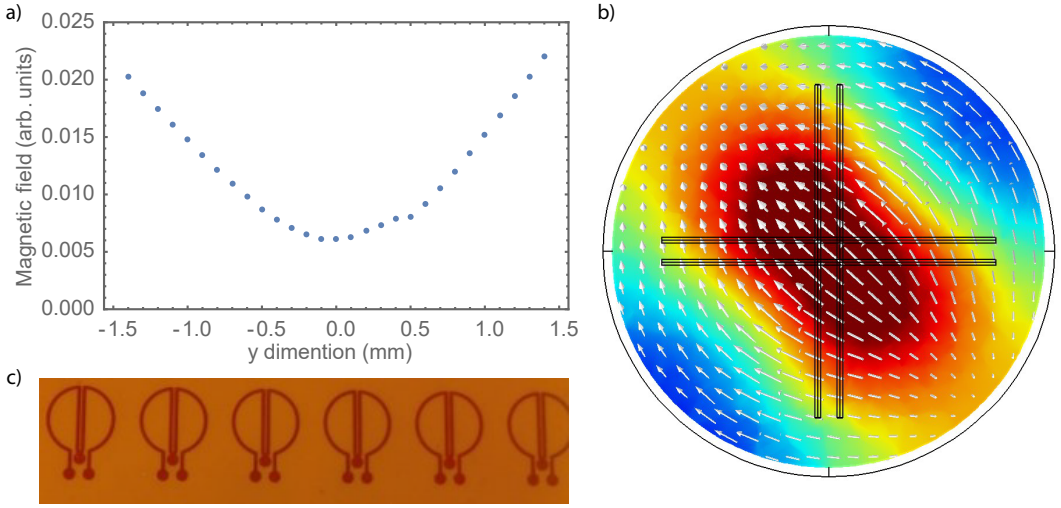

FIGURE 7.15: a) Magnetic field amplitude as a function of the dimension parallel to the diamond, produced by the COMSOL simulations b) Arrow density plot generated with COMSOL for the MW field simulation c) MW circuit printed on flexible kapton tape, for MW delivery on the front side of the optical assembly. Multiple circuits were printed but only two are needed for the measurements

to be placed crossed with one another. The central pad of the design is soldered onto the core of a co-axial cable while the two pads on the bottom are soldered to the ground of the cable. The circuits can be aligned with the holes labeled as b in Fig. 7.11. The circuit is printed on kapton tape to provide flexibility. The magnetic-field amplitude at the surface of the diamond optical assembly, as a function of the y-dimension centered at the the diamond can be seen in Fig. 7.15 (a). An arrow density plot of the magnetic field at the surface of the diamond produced by COMSOL can be seen in Fig. 7.15 (b). The circuit used to deliver MW to the diamond is shown in Fig. 7.15 (c).

§ 7.9 ODMR optimization

As discussed in previous chapters, a big part of optimizing the magnetic field sensitivity of the sensor is optimizing the ODMR features (see Eq. 2.6), once an appropriate diamond sample has been selected. As shown in Fig. 7.16 (a), the optimized ratio of contrast and linewdith for the ODMR of diamond used in this sensor is 1% and 100 KHz, respectively. However, due to hyperfine interaction from ^{14}N of the NV, three peaks are visible per single NV orientation in the ODMR. These three

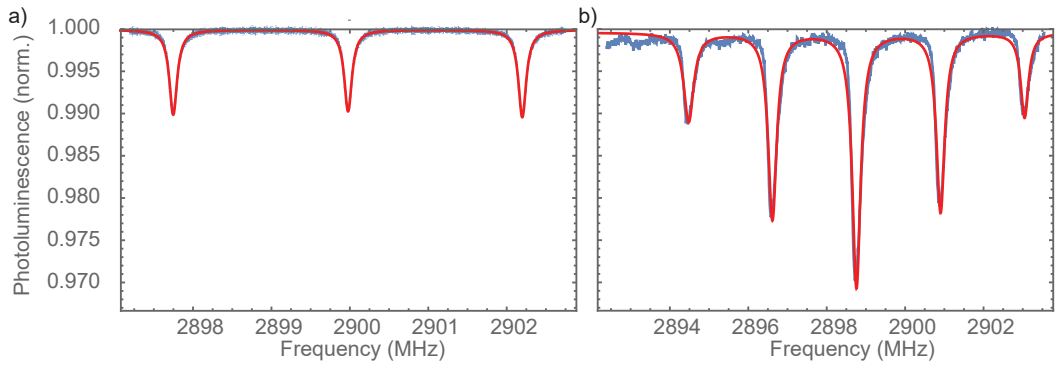

FIGURE 7.16: Normalized PL as a function of microwave frequency a) with a single MW frequency sweep b) with a three MW frequency sweep.

peaks can be coupled to improve the contrast of the measurement. To achieve this, we split the MW carrier into two paths, we mix one path with a frequency of 2.15 MHz (which matches the hyperfine splitting frequency) and re-introduce the carrier back with the use of a coupler. By doing so we are introducing three MW frequencies to our circuit and we address all the peaks at the same time, a MW frequency scan with the three frequencies can be seen in Fig. 7.16 (b). Other ways to improve contrast include applying an external field such that the ODMR peaks referring to different orientations overlap, or mixing another MW frequency to address the peaks created by both $m_s = +1$ and $m_s = -1$. In our case we introduced only hyperfine coupling, since we want to measure at zero-field, where the ODMR features of all orientations are overlapped, and apply circular MW, which excite either $m_s = +1$ or $m_s = -1$ selectively. The other factor to consider from Eq. 2.6, is the rate of photons collected. This depends on collection efficiency, as well as the pump light intensity. Finally, we optimize the ODMR features again by varying parameters, such as modulation depth and MW amplitude, for different green laser powers. Figure 7.17 shows the photon-shot noise as a function of pump-light power, for optimized MW frequency modulation depth and amplitude.

§ 7.10 Magnetic field sensitivity

Figure 7.18 shows the magnetic-field-noise spectra obtained by measurements with the optical assembly of the sensor and a QuSpin sensor for comparison. The blue and orange spectra are taken at zero-field on and off resonance, respectively. The purple and red spectra are taken at high-field on and off resonance, respectively.

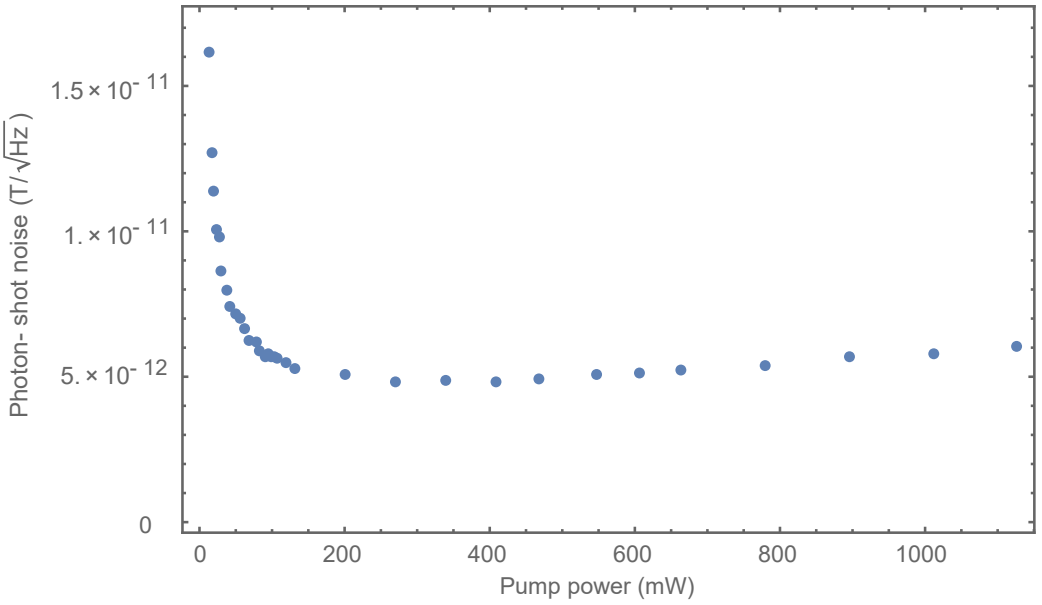

FIGURE 7.17: Photon-shot noise as a function of pump light power, for optimized MW frequency modulation depth and amplitude.

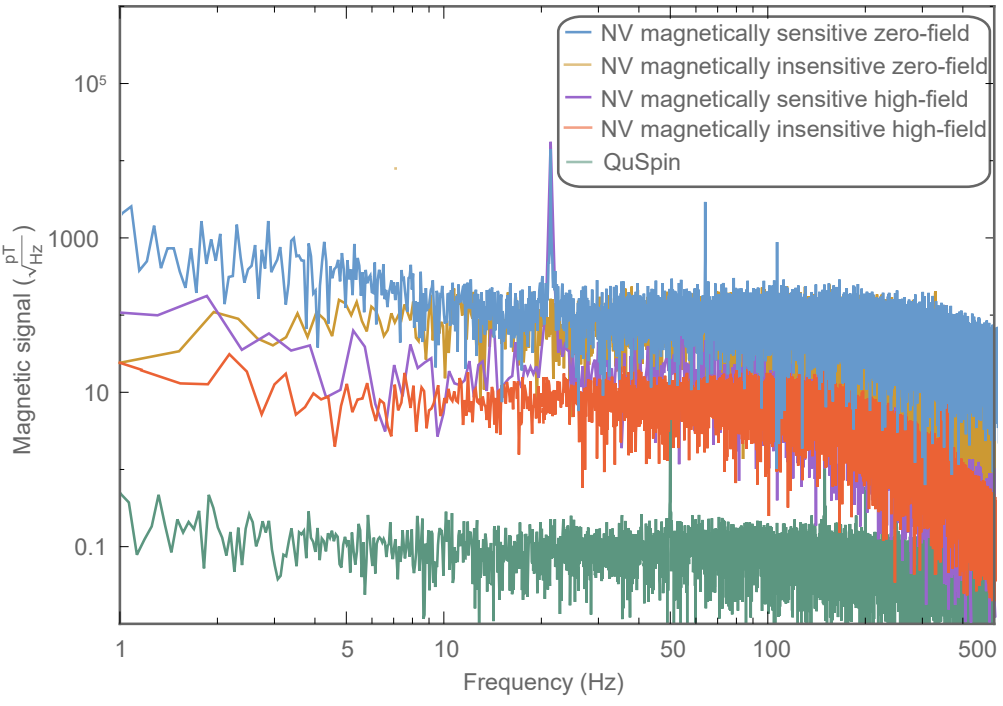

FIGURE 7.18: Magnetic-field-noise spectra obtained by measurements with the optical assembly of the sensor and a QuSpin sensor for comparison. The blue and orange spectra are taken at zero-field on and off resonance, respectively. The purple and red spectra are taken at high-field on and off resonance, respectively.

All four NV spectra are obtained by a Fourier transform of a LIA output, monitoring the NV PL, while a frequency modulated MW field is applied to the NVs. The modulation frequency is 4.6 kHz and the modulation depth 70 KHz.

The peaks at 50 Hz and harmonics are attributed to magnetic field from the power line in the lab and are not visible on the magnetically insensitive spectra. The insensitive spectra are obtained in the absence of a MW field. The noise floor in the region of 60-90 Hz for the magnetically insensitive spectrum is calculated as $75\,\mathrm{pT}/\sqrt{\mathrm{Hz}}$ and $7\,\mathrm{pT}/\sqrt{\mathrm{Hz}}$ for the zero-field and high-field cases, respectively. The above measurements are obtained with 1100 mW of pump light applied on the diamond for 0.5 s of acquisition time.

The difference in sensitivity between the high-field and zero-field cases can be attributed to loss of effective contrast in the sensor, which is cause because of the overlapping m_s ODMR resonances. As in the high-field case, they experience frequency shifts under external magnetic fields with the opposite sign. However, in the case of zero-field, the ODMR features attributed to the different m_s states are overlapped. Thus, if both m_s states are addressed during measurement, the effective sensitivity of this scheme to AC magnetic fields would be zero, due to the opposite frequency shift of the different m_s states.

§ 7.11 Conclusion and Outlook

We managed to construct a highly sensitive magnetic field sensor based on NV centers. The sensitivity of the sensor allows measurements of biological magnetic field, e.g., heart magnetic signal. If the sensor is further improved by one order of magnitude, it can be used measure magnetic fields produced by the brain, at a distance of a few cm from the skull, as already demonstrated with QuSpin magnetometers.

The materials used to construct the sensor and its geometry have a two-fold purpose. First, they are chosen to optimize the photon-collection to pump-light ratio of the sensor which, as of writing this thesis, is the best demonstrated in literature at 3.4 %. Second they achieve heat management of the sensor, limiting the temperature increase of the sensor, to temperatures bellow 37 °C, that would allow for endoscopic use, when it is connected to a heat sink via a copper wire and while an 1 W light beam for operation of the sensor.

The sensor has a demonstrated high-field sensitivity of $7\,\mathrm{pT}/\sqrt{\mathrm{Hz}}$, which makes it one of the most sensitive NV sensors, without having to use of ferrite "flux concentrators" or an AC measuring scheme. Furthermore, it can operate in zero-magnetic-field conditions e.g., a magnetically shielded room, where environmental magnetic-field noise would be detrimental for measurements.

Finally, the sensor's design is miniaturized and portable, while allowing access to the NV containing sample. The small size and portability enable its use as an endoscope in a medical context, while the access to the front side, allows for measurements with close proximity to the measured magnetic field source, minimizing the measured magnetic field's decay due to distance.

§ 8

Conclusion

In this dissertation, I presented a brief history of NV centers in diamond and gave an overview of the basic physics concerning the system, with a focus on optically pumped magnetometry. Then, I showcased the published work that resulted from this period of my doctoral research. The goals were to advance magnetic-field sensing with NV centers, achieving higher sensitivity and higher-resolution measurements, in portable and miniaturized designs. This work is a step towards new high-sensitivity NV-based sensing, enabling novel biological applications (e.g., brain-signal measurements) and resolving problems with current diagnostic sensors such as the requirement to operate at ultra-low temperatures and limited proximity to the magnetic-field source.

First, I presented the work (Ref [26]) on a miniaturized cavity-enhanced absorption-based diamond magnetometer with NV centers. At the time of publication, the sensor was the second-most-sensitive NV-based DC sensor in the world. It improved on the previous sensor of its kind [58] by two orders of magnitude in sensitivity, a record which most modern NV-based sensors still fail to surpass at the time of writing this thesis. The sensor had the added benefit of being miniaturized, with a diameter of 12.5 mm and a total length of 8 mm. The problem of limited photoluminescence collection faced by most NV-based sensors was overcome by monitoring absorption of the singlet IR NV transition. However, due to its smaller absorption cross-section compared to that of the commonly used triplet transition, it required a cavity-enhanced measuring scheme. The acquired knowledge aided in studying other IR-based NV measuring schemes, like the intracavity-etalon-based technique presented in Ref. [42].

Second, I presented the work from Ref. [119], where the abovementioned sensor was used, alongside others, to study the magnetic-field-dependent features of the

NV from 0 to $\sim 110\,\mathrm{mT}$. The study of these features is important, since they can be used for microwave (MW)-free magnetic-field measurements. These kinds of measurements would not be influenced by dynamic environments like the human body, where for example induced eddy currents could distort the MWs and influence the measurement sensitivity. By adapting the sensor of Ref. [26] to this technique, we were able to achieve an order of magnitude improvement in sensitivity compared to devices previously published in the literature [113] and gain valuable insight into the behavior of the magnetic-field-dependent NV features. We later built upon this knowledge in Ref. [54] and used it to construct a MW-free vector NV-based sensor [120].

Then, I presented an NV-based eddy-current-imaging sensor (Ref. [27]), based on the magnetic-field-dependent features we studied in Ref. [119]. The sensor used the MW-free scheme to detect changes on applied oscillating fields, in the range of 1 Hz to 4 MHz. The flat and wide bandwidth of the sensor is important, as other eddy-current-imaging technologies, like inductive coils and most atomic-vapor-cell magnetometers, perform poorly at low and high frequencies, respectively. The sensor was the first NV-based eddy-current-imaging sensor and was able to achieve sub-mm spatial resolution with high-sensitivity. The sensor being MW-free makes it an ideal candidate for measurements in a dynamic environment like the human body, where with higher sensitivity it could be used for diagnostics, e.g., cancer cell detection, due to the electric conductivity difference between cancerous and healthy cells [45]. As a continuation of this work, we later constructed a similar sensor and produced quality-control measurements on batteries [118], which enables the technology transfer of this NV-based magnetometry to industry.

Furthermore in collaborative work with Robert Bosch GmbH we constructed portable, miniaturized, highly sensitive, NV-based vector magnetic-field sensors (Ref. [87]). The sensors we constructed — fiber-coupled, less than 10 mm diameter and 40 mm in length, and sensitive to sub-nT fields — fulfilled these criteria. As a demonstration of one of the sensors, we produced magnetic field maps of the bore of a $> 100\,\mathrm{mT}$ Halbach magnet constructed [114] specifically for NV-based MW-free magnetic-field measurements.

Finally, I present a new sensor which culminates our efforts towards endoscopic measurements with NV centers in diamond. The new sensor surpassed the sensitivity of our previous efforts and has the same order-of-magnitude sensitivity as the most sensitive NV sensors to date [16]. It is miniaturised, portable and can be fully fiberized. It has the ability to operate at zero-magnetic-field conditions,

which are sometimes required for biological measurements in order to reduce environmental magnetic-field noise. We designed the sensor to optimize the photon-collection from magnetic-field sensitive NVs, achieving better photon-collection to pump-light ratio from what is currently presented in literature. At the same time it provided sufficient heat management to keep the sensor itself from surpassing temperatures that would be dangerous for operation within the human body. As of the writing of this thesis this work is still ongoing.

The above mentioned work can lead to many new projects that will advance the field of NV magnetometry and give it access to other well established fields. Since the NV still remains less sensitive to magnetic fields, compared to competitors like atomic-vapor-cell magnetometers and superconducting quantum interference device (SQUID) magnetometers, its future lies in measurements where magnetic fields decay with distance. Since NV magnetometers can be miniaturized, are portable and operate in dynamic environments, they would be able to achieve closer proximity than the competitors, especially in cases where the temperature of the magnetic field source should not be affected, as SQUID magnetometers have to operate at cryogenic temperatures and atomic-vapor-cell magnetometers need to be heated to well above room temperature for optimal operation.

One type of application that fulfils all the above mentioned criteria is biological measurements. Furthermore, diamond itself being bio-compatible enables a sensor that can be inserted inside a human body, where all the aforementioned advantages can be exploited. For that reason NV-based biological measurements are a natural way for the field to advance. Another ambition would be to use NV magnetometers to measure zero-to-ultra-low-field nuclear magnetic resonance (ZULF NMR) [19]. A high sensitivity zero-field NV magnetometer, like the one presented in this thesis, could enable such measurements, benefiting from the proximity to the field source that the NV allows, as well as the nano-scale spatial resolution of the NV when relevant.

Regarding NV-based magnetometry, the main challenges are intrinsic to the diamond's structure. Factors such as crystal strain, ^{12}C purity and [NV] to [N] concentration ratios can influence the linewidth and contrast of the probed resonance in an NV-based magnetometer, as seen in Eq. 2.4. At the forefront of addressing this issue are many commercial companies and research institutes around the globe, and this concerted effort to improve control over the diamond structure will likely result in improvement of NV-based sensors. Another improvement is likely to come from techniques that increase photon collection from the NV, like manufacturing

specialized optical assemblies (see Chap. 7), or alternatively using techniques based on absorption (see Chap. 3). A promising absorption technique has been explored theoretically already in Ref. [42], which with the current improvement on diamond sample manufacturing, can reach sub-pT/$\sqrt{\text{Hz}}$ sensitivities.

There are exiting times to be working on NV centers and I would be very happy to continuing my work and keeping up with advancements on the field.

§ A

Infrared-absorption cavity sensitivity estimates

For the sensor presented in Ch. 3, we consider a model like the one shown in Fig. A.1. A nitrogen-vacancy (NV) containing diamond is used to construct a cavity resonant with infrared (IR) light, and to the NV singlet-state zero-photon line. When the NVs are pumped by green light, absorption of IR light can be observed with a photodetector (PD), this absorption is enhanced by the cavity. By then applying a microwave (MW) field resonant to the $m_s = 0 \rightarrow m_s = \pm 1$, NV ground-state sublevels transition, population is, eventually, transferred to the singlet states. This leads to additional losses inside the cavity, which can be measured by the PD and used to estimate the magnetic field around the cavity.

The reflected-to-initial light-intensity ratio, R, and transmitted-to-initial light-intensity ratio, T, when the cavity is on resonance can be described by the following

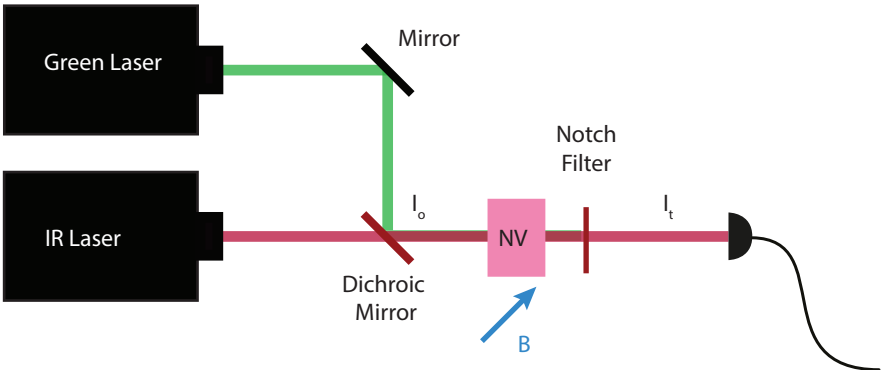

FIGURE A.1: Cavity enhanced measuring protocol experimental model schematic

equations:

$$R = \frac{I_r}{I_0} = \left(\frac{T_2 + A - T_1}{T_2 + A + T_1}\right)^2, \tag{A.1}$$

$$T = \frac{I_t}{I_0} = \frac{4T_1T_2(1-A)}{(T_2 + A + T_1)^2}, \tag{A.2}$$

where, T_1 and T_2 represented the transmission of cavity front and back mirrors, respectively and A notes the round trip losses of the cavity.

If the microwave frequency we apply is represented as, ν_{MW}. The cavity's sensitivity to losses, and thus magnetic field, B, can be related to change in the transmitted intensity as seen bellow:

$$\frac{\partial I_t}{\partial B} = I_0\frac{\partial T}{\partial B} = I_0\frac{\partial T}{\partial A} \times \frac{\partial A}{\partial \nu_{\mathrm{MW}}} \times \frac{\partial \nu_{\mathrm{MW}}}{\partial B} = c_0\, I_0\frac{\partial T}{\partial A}, \tag{A.3}$$

We can use Eq. A.1 to calculate:

$$\frac{\partial T}{\partial A} = \frac{4T_1T_2(A - T_1 - T_2 - 2)}{(A + T_1 + T_2)^3}. \tag{A.4}$$

We can now use Eq. A.4 to select the transmission for the front and back mirrors of the cavity in order maximize the sensitivity to loses. Form the work done in Ch. 3 we know that $A_{min} = 1.66\%$ and $A_{max} = 3.09\%$, where, A_{min} symbolizes the losses that are caused by the diamond crystal with no pump light applied and A_{max} symbolizes the losses of the cavity when the pump light intensity is enough to saturate the NVs of the B3a diamond sample. Selecting the value for saturation $A_{max} = 3.09\%$ we produce Fig. A.2 (a). For the current coating on B3a, $\mathrm{T}_2 = 0.008$, we can see in Fig A.2 (b) that the maximum response to losses would be for a front mirror transmission of $\mathrm{T}_1 \simeq 0.02$.

To optimize the sensitivity though we have to consider the overall transmission from the cavity, as this would affect the photon-shot noise limit (see Eq. 1.2). The photon-shot noise be approximated with:

$$\delta B_p \simeq \frac{\sqrt{T}}{|\partial T/\partial A|}. \tag{A.5}$$

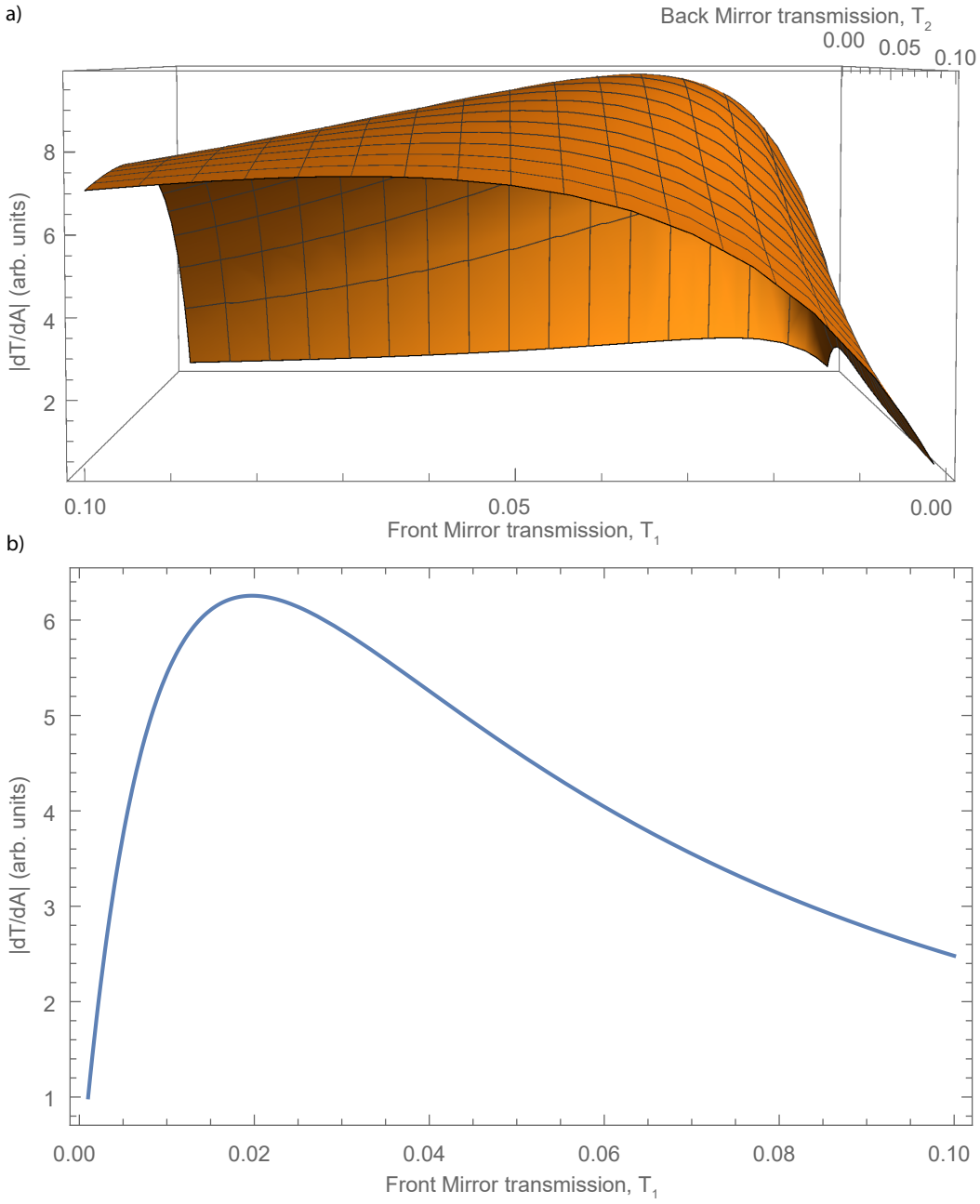

FIGURE A.2: a) Cavity response to losses for different mirror transmissions T_1 and T_2. b) Cavity response to losses for different mirror transmission T_1 and $T_2 = 0.008$.

We can follow a similar procedure varying the transmissions though the mirrors T_1 and T_2, the results of this are shown in Fig. A.3, where (a) is showing variations of both transmission values and (b) is showing variation of T_1 while $T_2 = =0.008$. We see now that the optimum is not $T_1 \simeq 0.02$, as Fig. A.2 suggests, but rather $T_1 \simeq 0.016$.

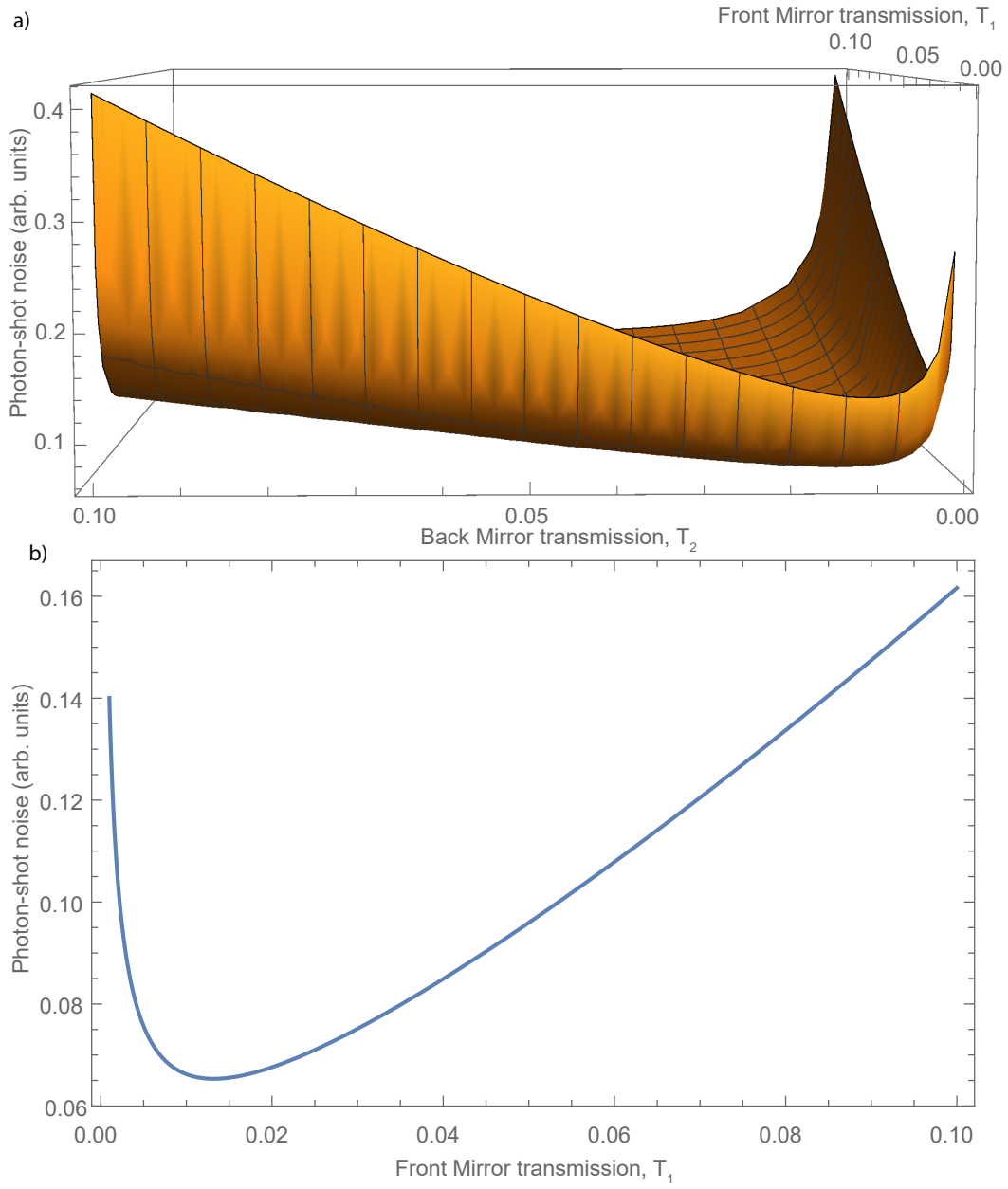

FIGURE A.3: a) Photon-shot noise for different mirror transmissions T_1 and T_2. b) Photon-shot noise for different mirror transmission T_1 and $T_2 = 0.008$.

§ B

Modeling eddy-current imaging sensitivity

As shown in Fig.B.1 materials with different conductivity produce a different response when imaged by eddy currents. This section aims to calculate the required magnetic field sensitivity, an NV-based sensor should have, in order to image and distinguish between different conductivity materials and in particular between biological tissues.

To perform this calculation we assume a cylindrical conductor with radius, r_0, height, h, and conductivity, σ, placed at a distance, d, from out sensor, as seen in Fig. B.2.

To induce eddy currents we need to place the conductor inside an oscillating magnetic field. For this purpose we use a coil, the field of which is given by the following equation:

$$B_{coil} = \frac{\mu_0 N I r_{coil}^2}{2(r_{coil}^2 + d^2)^{3/2}}, \tag{B.1}$$

where $\mu_0 = 4\pi 10^{-7}\,\mathrm{T\,m/A}$, N are the coil's turns, I is the current running though the coil, r_{coil} the coil radius, and d the distance between the coil and the conductor. For the setup used in Ref. [27] we calculate $\mathrm{B}_{coil} = 91\,\mu\mathrm{T}$.

We calculate the induced electromagnetic force U:

$$U = \frac{\Delta\Psi}{\Delta t} = E(r) 2\pi r, \tag{B.2}$$

where $\Delta\Psi$ is the magnetic flux, $1/\Delta t = \omega = 2\pi f$, with f being the modulation frequency of B_{coil}, and $E(r)$ the electric field intensity at the location r.

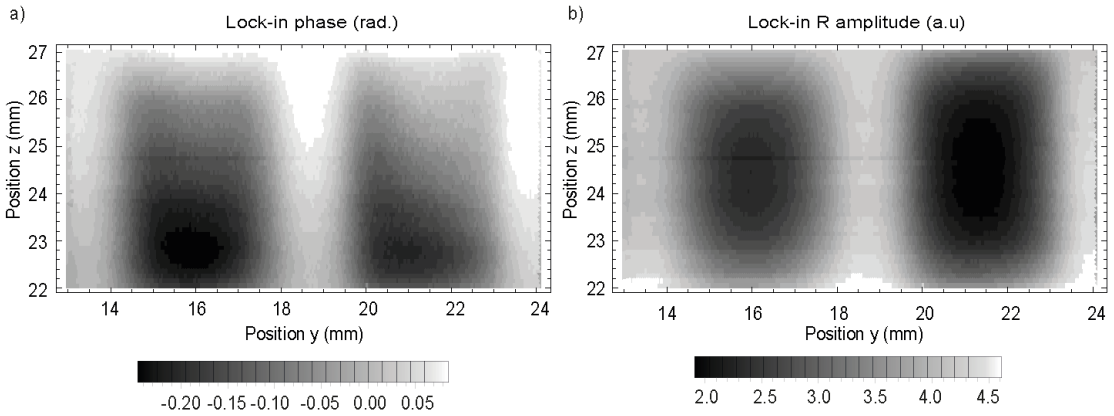

FIGURE B.1: Aluminium (left) and copper (right) metals, imaged with eddy currents.

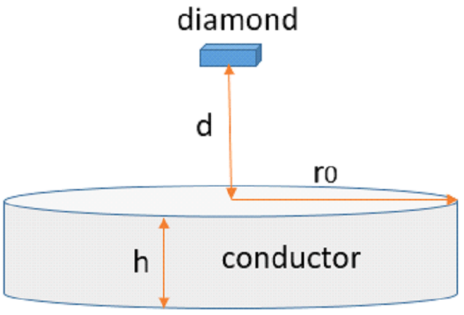

FIGURE B.2: Conductor and diamond sample with relevant dimensions for calculations.

Knowing that

$$\Delta\Psi = \pi r^2 B, \tag{B.3}$$

We simplify the electric field intensity as:

$$E = \pi r f B \tag{B.4}$$

Then by using the Biot-Savart law the field produced by the eddy currents can be calculated as:

$$B_{eddy}(r) = \frac{\mu_0}{4\pi} \int \frac{I dI \times r'}{|r'|^3}, \tag{B.5}$$

if $I = \sigma\, dr\, dh$ and $r' = \sqrt{r^2 + (d+h)^2}$:

$$B_{eddy}(r) = \int_0^h \int_0^{r_0} \frac{10^{-7}\, E\, \sigma}{(r^2 + (d+h')^2)^{3/2}}\, r\, 2\pi\, r\, dr\, dh'. \tag{B.6}$$

We can now calculate the magnetic field produced by the eddy currents using Eq.B.6. Selecting experimental parameters from Ref. 5: $f = 1\,\mathrm{MHz}$ for the oscillating magnetic field frequency, $r_0 = 1\,\mathrm{mm}$ and $h = 0.1\,\mathrm{mm}$ for the sample dimensions, a distance of $d = 200\,\mu\mathrm{m}$ and a sensitivity of $\sim 10\mu\mathrm{T}/\sqrt{Hz}$.

We calculate that items with conductivity higher than $\sigma = 1\,\mathrm{MS/m}$, ($\sigma_{copper} = 5.96\times10^7\,\mathrm{S/m}$, $\sigma_{aluminium} = 3.77\times10^7\,\mathrm{S/m}$) will be visible, which was proven experimentally.

Following the above calculations, if the sensitivity of the sensor is improved to $100\,\mathrm{fT}/\sqrt{Hz}$, objects with $\sigma = 0.1\,\mathrm{S/m}$ could be imaged, with signal to noise ratio of 10. Which would be enough to image some biological tissues e.g., Haemangiopericytoma with $1.3\,\mathrm{S/m}$ [45].

Currently the most sensitive NV sensors are in the range of $10\,\mathrm{pT}\sqrt{\mathrm{Hz}}$ [16,27], but there have been demonstrations of sub-$\mathrm{pT}\sqrt{\mathrm{Hz}}$ either at AC frequencies [115] or with the use of ferrite flux concentrators [44], so the use of NV-based eddy-current imaging sensors for detection of biological tissues might be possible.

§ C

Diamond samples used throughout the thesis

This appendix presents the diamond samples I used throughout my doctoral research. The characteristics of the diamond samples used to perform the measurements are crucial, as the composition of the diamond can determine factors such as the linewidth and contrast of the optically detected magnetic resonance features, amount of fluorescence emitted, etc.

Sample B3a

Diamond sample B3a is a $3.0 \times 3.0 \times 0.5\,\mathrm{mm}^3$ type Ib, (111)-cut, high-pressure–high-temperature grown sample, purchased from Element Six. The initial nitrogen concentration of the sample is specified as < 100 ppm. The sample is irradiated with 5 MeV of electrons and a dosage of $2\times\ 10^{19}\ \mathrm{cm}^{-2}$, and then annealed at 700 °C for 2 h. A high reflective coating of 98(0.5)% at the wavelengths of 532 nm and

Sample	**Type**	**Surface**	**[N] ppm**	**^{13}C**	**Used in**
B3a	HPHT	(111)	< 110	1.1%	§§3, 4
B1	HPHT	(111)	< 2	0.03%	§6
W4	CVD	(100)	< 1	1.1%	§4
F11	HPHT	(111)	< 200	1.1%	§§2, 4
C7	HPHT	(100)	< 200	1.1%	§4
E4	HPHT	(100)	< 13	0.01%	§6
S1	HPHT	(111)	< 3	0.03%	§§2, 7

TABLE C.1: Diamond samples used throughout the thesis. CVD: chemical vapor deposition, HPHT: high pressure, high temperature.

1042 nm was applied to one side of the diamond and an anti reflective coating for the same wavelengths on the other.

Sample B1

Diamond sample B1 is a $0.8 \times 0.8 \times 0.5\,\mathrm{mm}^3$ (111)-cut, type Ib, 99.97% ^{12}C enriched, HPHT grown diamond. The sample was irradiated with 2 MeV electrons at a dose of 2×10^{18} cm^{-2} at room temperature and then annealed at 1000 °C for 2 hours in vacuum. The [NV$^-$] concentration was determined by electron spin resonance to be 0.4 ppm.

Sample W4

Sample W4 is a $3.0 \times 3.0 \times 0.3\,\mathrm{mm}^3$, single-crystal (100)-cut, type Ib diamond, synthesized using the CVD-groth method. The diamond with had an initial nitrogen concentration of < 1 ppm and was electron-irradiated at 10 MeV (dose:10^{18} cm^{-2}). I was then annealed at 720°C for two hours.

Sample F11

Sample F11 is a $2.1 \times 2.3 \times 0.6\,\mathrm{mm}^3$ single-crystal (111)-cut, type Ib diamond, synthesized using a HPHT method (from Element six). The diamond with an initial nitrogen concentration of < 200 ppm was electron-irradiated at 14 MeV (dose: 10^{18} cm^{-2}) and then annealed at 700°C for three hours.

Sample C7

Sample C7 is a $3.1 \times 3.3 \times 0.4\,\mathrm{mm}^3$ single-crystal (100)-cut, type Ib diamond, synthesized using a HPHT method. The diamond had an initial nitrogen concentration of < 200 ppm and was electronirradiated at 10 MeV (dose: 10^{18} cm^{-2}) and then annealed at 750°C for three hours.

Sample E4

Sample E4 is a $2.0 \times 2.0 \times 0.5\,\mathrm{mm}^3$ single-crystal (100)-cut, type Ib diamond, synthesized using a HPHT method. It was purchased from Element Six. The initial [N] concentration of the sample was specified as < 10 ppm. The sample was irradiated with 5 MeV electrons at a dose of 2×10^{19} cm^{-2} and then annealed at 700 °C for 8 hours.

Sample S1

Sample S1 is a $0.69 \times 0.71 \times 0.49\,\mathrm{mm}^3$ 99.97% ^{12}C, (111)-cut diamond single crystal. It was laser-cut from a ^{12}C-enriched diamond single crystal, grown by the

HPHT method at 6.1 GPa and 1430 °C. A metal solvent containing a nitrogen-getter and carbon powder prepared by pylolysis of 99.97% ^{12}C-enriched methane as a carbon source were used. It was irradiated with 2 MeV electrons from a Cockcroft-Walton accelerator to a total fluence of 1.8×10^{18}cm^{-2} at room temperature, and annealed at 800 °C for 5 hours. Its source diamond was reported to have 3-ppm initial nitrogen and 0.9 ppm NV^- after conversion, measured by electron paramagnetic resonance techniques. This diamond sample provides remarkable narrow optically detected magnetic resonance and ground-state level anti-crossing features with small residual couplings to ^{13}C nuclear spins which is essential for the sensitivity.

Bibliography

[1] V. M. Acosta, E. Bauch, A. Jarmola, L. J. Zipp, M. P. Ledbetter, D. Budker. *Broadband magnetometry by infrared-absorption detection of nitrogen-vacancy ensembles in diamond*, Applied Physics Letters **97**, 17 (2010).

[2] V. M. Acosta, *et al.*. *Diamonds with a high density of nitrogen-vacancy centers for magnetometry applications.*, Phys. Rev. B. **8** (2009).

[3] V. M. Acosta, E. Bauch, M. P. Ledbetter, A. Waxman, L.-S. Bouchard, D. Budker. *Temperature Dependence of the Nitrogen-Vacancy Magnetic Resonance in Diamond*, Phys. Rev. Lett. **104** (2010).

[4] V. M. Acosta, A. Jarmola, E. Bauch, D. Budker. *Optical properties of the nitrogen-vacancy singlet levels in diamond*, Phys. Rev. B **82** (2010).

[5] V. M. Acosta, K. Jensen, C. Santori, D. Budker, R. G. Beausoleil. *Electromagnetically Induced Transparency in a Diamond Spin Ensemble Enables All-Optical Electromagnetic Field Sensing*, Phys. Rev. Lett. **110** (2013).

[6] A. Ajoy, P. Cappellaro. *Stable three-axis nuclear-spin gyroscope in diamond*, Phys. Rev. A **86** (2012).

[7] A. Ajoy, Y. Liu, P. Cappellaro. *DC Magnetometry at the T_2 Limit*, arXiv preprint arXiv:1611.04691 (2016).

[8] J. C. Angus, H. A. Will, W. S. Stanko, W. T., D. J. Twitchen, A. J. Whitehead, S. E. Coe, G. A. Scarsbrook. *Growth of diamond seed crystals by vapor deposition*, Journal of Applied Physics **39** (1968).

[9] S. V. Anishchik, V. G. Vins, K. L. Ivanov. *Level-crossing spectroscopy of nitrogen-vacancy centers in diamond: sensitive detection of paramagnetic defect centers*, arXiv1609.07957 (2016).

[10] S. Armstrong, L. J. Rogers, R. L. McMurtrie, N. B. Manson. *NV-NV electron–electron spin and NV-NS electron — electron and electron-nuclear spin interaction in diamond*, Physics Procedia **3**, 4 (2010).

[11] N. Aslam, G. Waldherr, P. Neumann, F. Jelezko, J. Wrachtrup. *Photo-induced ionization dynamics of the nitrogen vacancy defect in diamond investigated by single-shot charge state detection*, New Journal of Physics **15** (2013).

[12] G. Balasubramanian, *et al.*. *Nanoscale imaging magnetometry with diamond spins under ambient conditions*, Nature **455**, 7213 (2008).

[13] F. Barbieri, V. Trauchessec, L. Caruso, T. J. Rosillo, B. Telenczuk, E. Paul, T. Bal, A. Destexhe, C. Fermon, M. Pannetier-Lecoeur, G. Ouanounou. *Local recording of biological magnetic fields using Giant Magneto Resistance-based micro-probes*, Scientific Reports **6** (2016).

[14] P. E. Barclay, K.-M. C. Fu, C. Santori, R. G. Beausoleil. *Chip-based microcavities coupled to nitrogen-vacancy centers in single crystal diamond.*, Applied Physics Letters (2009).

[15] J. F. Barry, J. M. Schloss, E. Bauch, M. J. Turner, C. A. Hart, L. M. Pham, R. L. Walsworth. *Sensitivity optimization for NV-diamond magnetometry*, Rev. Mod. Phys. **92** (2020).

[16] J. F. Barry, M. J. Turner, J. M. Schloss, D. R. Glenn, Y. Song, M. D. Lukin, H. Park, R. L. Walsworth. *Optical magnetic detection of single-neuron action potentials using quantum defects in diamond*, PNAS **113** (2016).

[17] A. Batalov, V. Jacques, F. Kaiser, P. Siyushev, P. Neumann, L. J. Rogers, R. L. McMurtrie, N. B. Manson, F. Jelezko, J. Wrachtrup. *Low Temperature Studies of the Excited-State Structure of Negatively Charged Nitrogen-Vacancy Color Centers in Diamond*, Physical Review Letters **102** (2009).

[18] G. P. Berman, A. R. Bishop, B. M. Chernobrod, M. E. Hawley, G. W. Brown, V. I. Tsifrinovich. *Measurement of single electron and nuclear spin states based on optically detected magnetic resonance*, J. Phys.: Conf. Ser (2006).

[19] J. W. Blanchard, B. Dmitry, A. Trabesinger. *Lower than low: Perspectives on zero- to ultralow-field nuclear magnetic resonance*, Journal of Magnetic Resonance **323** (2021).

[20] P. D. Bloch, W. S. Brochlesby, R. T. Harley, M. J. Henderson. *Effects of microwave excitations on spectral hole-burning in colour centre systems*, J. Phys. (Paris) (1985).

[21] L.-S. Bouchard, V. M. Acosta, E. Bauch, D. Budker. *Detection of the Meissner effect with a diamond magnetometer*, New Journal of Physics **2** (2011).

[22] B. B. Buckley, G. D. Fuchs, L. C. Bassett, D. D. Awschalom. *Spin-Light Coherence for Single-Spin Measurement and Control in Diamond*, Science (2010).

[23] D. Budker, M. Romalis. *Optical magnetometry*, Nature **3** (2007).

[24] F. Bundy, H. T. Hall, H. Strong, R. Wentorf. *Man-made diamonds.*, Nature **176** (1955).

[25] G. Chatzidrosos, J. S. Rebeirro, H. Zheng, T. Schneemann, M. Omar, A. Brenneis, F. M. Stürner, T. Fuchs, T. Buck, R. Rölver, B. P., A. Budker, D. Wickenbrock. *Fiberized diamond-based vector magneto-meter*, arXiv:2102.11902 (2021).

[26] G. Chatzidrosos, A. Wickenbrock, L. Bougas, N. Leefer, T. Wu, K. Jensen, Y. Dumeige, B. D. *Miniature Cavity-Enhanced Diamond Magnetometer*, Phys. Rev. Applied **8** (2017).

[27] G. Chatzidrosos, A. Wickenbrock, L. Bougas, H. Zheng, O. Tretiak, Y. Yang, D. Budker. *Eddy-Current Imaging with Nitrogen-Vacancy Centers in Diamond*, Phys. Rev. Applied **11** (2019).

[28] B. M. Chernobrod, G. P. Berman. *Spin microscope based on optically detected magnetic resonance.*, J. Appl. Phys. **97** (2005).

[29] H. Clevenson, L. M. Pham, C. Teale, K. Johnson, D. Englund, B. D. *Robust high-dynamic-range vector magnetometry with nitrogen-vacancy centers in diamond featured*, Appl. Phys. Lett. **112** (2018).

[30] C. J. Cochrane, J. Blacksberg, M. A. Anders, P. M. Lenahan. *Vectorized magnetometer for space applications using electrical readout of atomic scale defects in silicon carbide*, Scientific Reports **6** (2016).

[31] H. Dang, A. C. Maloof, M. V. Romalis. *Ultrahigh sensitivity magnetic field and magnetization measurements with an atomic magnetometer*, Applied Physics Letters **97** (2010).

[32] G. D'Angelo, S. Rampone. *Shape-based defect classification for Non Destructive Testing*, 2nd IEEE International Workshop on Metrology for Aerospace, MetroAeroSpace 2015 - Proceedings **08** (2015).

[33] G. Davies, M. F. Hamer. *Optical studies of the 1.945 ev vibronic band in diamond*, Proc. R. Soc. London Ser. A **348** (1976).

[34] G. Davies, S. C. Lawson, A. T. Collins, A. Mainwood, S. J. Sharp. *Vacancy-related centers in diamond*, Phys. Rev. B **46** (1992).

[35] C. Deans, L. Marmugi, S. Hussain, F. Renzoni. *Electromagnetic induction imaging with a radio-frequency atomic magnetometer*, Applied Physics Letters **108** (2016).

[36] C. Deans, L. Marmugi, F. Renzoni. *Active underwater detection with an array of atomic magnetometers*, Applied Optics **57** (2018).

[37] I. A. Dobrinets, V. G. Vins, A. M. Zaitsev, T. Sekiguchi, H. Watanabe, H. Kato, T. Makino, H. Okushi, S. Yamasaki. *HPHT-treated diamonds*, Springer (2016).

[38] M. W. Doherty, N. B. Manson, P. Delaney, L. C. L. Hollenberg. *The negatively charged nitrogen-vacancy centre in diamond: the electronic solution.*, New Journal of Physics **13** (2011).

[39] M. W. Doherty, V. V. Struzhkin, D. Simpson, L. P. McGuinness, Y. Meng, A. Stacey, T. J. Karle, H. R. J., M. N. B., L. C. Hollenberg, S. Prawer. *Electronic properties and metrology applications of the diamond NV center under pressure.*, Phys. Rev. Lett. **112** (2014).

[40] F. Dolde, H. Fedder, M. W. Doherty, T. Nobauer, F. Rempp, G. Balasubramanian, T. Wolf, F. Reinhard, L. C. L. Hollenberg, F. Jelezko, J. Wrachtrup. *Electric-field sensing using single diamond spins*, Nature Physics Letter **455** (2008).

[41] Y. Dumeige, M. Chipaux, V. Jacques, F. Treussart, J.-F. Roch, T. Debuisschert, V. M. Acosta, A. Jarmola, K. Jensen, P. Kehayias, D. Budker. *Magnetometry with nitrogen-vacancy ensembles in diamond based on infrared absorption in a doubly resonant optical cavity*, Phys. Rev. B **87** (2013).

[42] Y. Dumeige, J.-F. Roch, F. Bretenaker, T. Debuisschert, V. Acosta, C. Becher, G. Chatzidrosos, A. Wickenbrock, L. Bougas, A. Wilzewski, B. D. *Infrared laser threshold magnetometry with a NV doped diamond intracavity etalon*, arXiv:2008.07339 **27** (2019).

[43] D. Farfurnik, A. Jarmola, L. M. Pham, Z.-H. Wang, V. V. Dobrovitski, R. L. Walsworth, D. Budker, N. Bar-Gill. *Optimizing a dynamical decoupling protocol for solid-state electronic spin ensembles in diamond*, Phys. Rev. B **92** (2015).

[44] I. Fescenko, A. Jarmola, I. Savukov, P. Kehayias, J. Smits, J. Damron, N. Ristoff, N. Mosavian, V. M. Acosta. *Diamond magnetometer enhanced by ferrite flux concentrators*, Phys. Rev. Research **2** (2020).

[45] K. Foster, J. Schepps. *Dielectric Properties of Tumor and Normal Tissues at Radio through Microwave Frequencies*, Journal of Microwave Power **16**, 2 (1981).

[46] K.-M. Fu, C. Santori, P. E. Barclay, L. J. Rogers, N. B. Manson, R. G. Beausoleil. *Observation of the Dynamic Jahn-Teller Effect in the Excited States of Nitrogen-Vacancy Centers in Diamond*, Phys. Rev. Lett. (2009).

[47] D. R. Glenn, K. Lee, H. Park, R. Weissleder, A. Yacoby, M. D. Lukin, H. Lee, R. L. Walsworth, C. B. Connolly. *Single-cell magnetic imaging using a quantum diamond microscope*, Nature methods **12** (2015).

[48] A. Gruber, A. Däbenstedt, C. Tietz, L. Fleury, J. Wrachtrup, C. von Borczyskowski. *Scanning Confocal Optical Microscopy and Magnetic Resonance on Single Defect Centers.*, Science **276** (1997).

[49] J. P. Hadden, J. P. Harrison, A. C. Stanley-Clarke, L. Marseglia, Y.-L. D. Ho, B. R. Patton, J. L. O'Brien, J. G. Rarity. *Strongly enhanced photon collection from diamond defect centers under microfabricated integrated solid immersion lenses*, Applied Physics Letters **97** (2010).

[50] L. T. Hall, P. Kehayias, D. A. Simpson, A. Jarmola, A. Stacey, D. Budker, L. C. L. Hollenberg. *Detection of nanoscale electron spin resonance spectra demonstrated using nitrogen-vacancy centre probes in diamond*, Nat Commun **7** (2016).

[51] L. T. Hall, P. Kehayias, D. A. Simpson, A. Jarmola, D. Stacey, A. Budker, L. C. L. Hollenberg. *Electron Spin Resonance Spectroscopy via Relaxation of Solid-State Spin Probes at the Nanoscale*, arXiv:1503.00830 (2015).

[52] S. Hussain, L. Marmugi, C. Deans, F. Renzoni. *Electromagnetic imaging with atomic magnetometers: a novel approach to security and surveillance*, SPIE 9823, Detection and Sensing of Mines, Explosive Objects, and Obscured Targets XXI, 98230Q **9823** (2016).

[53] J. Isberg, J. Hammersberg, E. Johansson, W. T., D. J. Twitchen, A. J. Whitehead, S. E. Coe, G. A. Scarsbrook. *High carrier mobility in single-crystal plasma-deposited diamond*, Science **297** (2002).

[54] V. Ivády, H. Zheng, A. Wickenbrock, L. Bougas, G. Chatzidrosos, K. Nakamura, H. Sumiya, T. Ohshima, J. Isoya, B. D., I. A. Abrikosov, A. Gali. *Photoluminescence at the ground state level anticrossing of the nitrogen-vacancy center in diamond*, arXiv:2006.05085 (2020).

[55] F. Jelezko, T. Gaebel, I. Popa, M. Domhan, A. Gruber, J. Wrachtrup. *Observation of Coherent Oscillation of a Single Nuclear Spin and Realization of a Two-Qubit Conditional Quantum Gate*, Phys. Rev. Lett. **93** (2004).

[56] F. Jelezko, T. Gaebel, I. Popa, A. Gruber, J. Wrachtrup. *Observation of Coherent Oscillations in a Single Electron Spin.*, Phys. Rev. Lett. (2004).

[57] K. Jensen, *et al.*. *A protease-based biosensor for the detection of schistosome cercariae*, Scientific Reports **6**, 24725 (2016).

[58] K. Jensen, N. Leefer, A. Jarmola, Y. Dumeige, V. M. Acosta, P. Kehayias, B. Patton, D. Budker. *C*, Phys. Rev. Lett. **112** (2014).

[59] H. Kanda. *HPHT-treated diamonds*, Journal of Physics **30** (2000).

[60] J. R. Kirtley, A. C. Mota, M. Sigrist, T. M. Rice. *Spin microscope based on optically detected magnetic resonance.*, J. Phys. Condens. Matter **10** (1998).

[61] G. Kucsko, P. C. Maurer, N. Y. Yao, M. Kubo, H. J. Noh, P. K. Lo, H. Park, M. D. Lukin. *Nanometre-scale thermometry in a living cell*, Nature Physics Letter **500** (2013).

[62] D. Le Sage, K. Arai, D. Glenn, S. DeVience, L. Pham, L. Rahn-Lee, M. Lukin, A. Yacoby, A. Komeili, R. Walsworth. *Optical magnetic imaging of living cells*, Nature **496** (2013).

[63] D. Le Sage, L. M. Pham, N. Bar-Gill, C. Belthangady, M. D. Lukin, A. Yacoby, R. L. Walsworth. *Efficient photon detection from color centers in a diamond optical waveguide*, Phys. Rev. B **85** (2012).

[64] M. Ledbetter, I. M. Savukov, D. Budker, V. Shah, S. Knappe, J. Kitching, D. Michalak, A. Xu, S. Pines. *Zero-field remote detection of NMR with a microfabricated atomic magnetometer.*, PNAS **105** (2008).

[65] M. P. Ledbetter, K. Jensen, R. Fischer, A. Jarmola, D. Budker. *Gyroscopes based on nitrogen-vacancy centers in diamond*, Phys. Rev. A **86** (2012).

[66] A. Lenef, S. C. Rand. *Electronic structure of the N-V center in diamond: Theory*, Phys. Rev. B **53** (1996).

[67] T. Lenz, *et al.*. *Probing topological spin structures using light-polarization and magnetic microscopy*, Phys. Rev. Applied **15** (2021).

[68] J. H. N. Loubser, A. van Wyk. *Electron spin resonance in the study of diamond*, Rep. Prog. Phys. **43** (1978).

[69] I. Lovchinsky, *et al.*. *Nuclear magnetic resonance detection and spectroscopy of single proteins using quantum logic*, Science **351** (2016).

[70] D. Maclaurin, M. W. Doherty, L. C. L. Hollenberg, A. M. Martin. *Measurable Quantum Geometric Phase from a Rotating Single Spin*, Phys. Rev. Lett. **108** (2012).

[71] P. Manandhar, K.-S. Chen, K. Aledealat, G. Mihajlović, C. S. Yun, M. F., G. J. Sullivan, G. F. S., P. B. Chase, S. von Molnár, P. Xiong. *The detection of specific biomolecular interactions with micro-Hall magnetic sensors*, Nanotechnology **20** (2009).

[72] N. B. Manson, J. Harrison. *Photo-ionization of the nitrogen-vacancy center in diamond*, Diamond & Related Materials **14** (2005).

[73] L. Marmugi, C. Deans, R. Renzoni. *Atomic Magnetometry-Based Electromagnetic Imaging of Low-conductivity Semiconductors*, arXiv:1805.05743 (2018).

[74] L. Marmugi, S. Hussain, F. Renzoni. *Electromagnetic induction imaging with a radio-frequency atomic magnetometer*, Appl. Phys. Lett. **108** (2016), p. 103503.

[75] L. Marmugi, F. Renzoni. *Optical Magnetic Induction Tomography of the Heart*, Scientific Reports **6** (2016).

[76] J. R. Maze, A. Gali, E. Togan, Y. Chu, A. Trifonov, E. Kaxiras, M. D. Lukin. *Properties of nitrogen-vacancy centers in diamond: the group theoretic approach.*, New Journal of Physics **13** (2011).

[77] J. R. Maze, *et al.*. *Nanoscale magnetic sensing with an individual electronic spin in diamond*, Nature **455**, 7213 (2008).

[78] C. A. McLellan, B. A. Myers, S. kraemer, O. K., D. D. Awschalom, A. C. Bleszynski Jayich. *Patterned formation of highly coherent nitrogen vacancy centers using a focused electron irradiation technique*, Nano letters **16** (2016).

[79] J. Meijer, B. Burchard, M. Domhan, C. Wittman, T. Gaebel, I. Popa, F. Jelezko, J. Wrachtrup. *Generation of single color centers by focused nitrogen implantation.*, Appl. Phys. Lett. **87** (2005).

[80] E. E. Mikhailov, I. Novikova, M. D. Havey, F. A. Narducci. *Magnetic field imaging with atomic Rb vapor.*, Optics Letters **34** (2009).

[81] T. Mittiga, S. Hsieh, C. Zu, B. Kobrin, F. Machado, P. Bhattacharyya, N. Z. Rui, A. Jarmola, S. Choi, D. Budker, N. Y. Yao. *Imaging the Local Charge Environment of Nitrogen-Vacancy Centers in Diamond*, Phys. Rev. Letters **121** (2018).

[82] N. Mizuochi, J. Isoya, J. Niitsuma, T. Sekiguchi, H. Watanabe, H. Kato, T. Makino, H. Okushi, S. Yamasaki. *Isotope effects between hydrogen and deuterium microwave plasmas on chemical vapor deposition homoepitaxial diamond growthd*, Journal of applied physics **101** (2007).

[83] K. Ohno, J. F. Heremans, L. C. Bassett, M. B. A., D. M. Toyli, A. C. Bleszynski Jayich, C. J. Palmstrøm, D. D. Awschalom. *Engineering shallow spins in diamond with nitrogen delta-doping*, Applied Physics Letters **101** (2012).

[84] C. Osterkamp, M. Mangold, J. Lang, P. Balasubramanian, T. Teraji, B. Naydenov, F. Jelezko. *Engineering preferentially-aligned nitrogen-vacancy centre ensembles in cvd grown diamond*, Scientific reports **9** (2019).

[85] P. Ovartchaiyapong, K. W. Lee, B. A. Myers, A. C. B. Jayich, A. Stacey, D. Budker, L. C. L. Hollenberg. *Dynamic strain-mediated coupling of a single diamond spin to a mechanical resonator*, Nat Commun **5** (2014).

[86] Y. N. Palyanov, I. N. Kupriyanov, A. F. Khokhryakov, R. V. G. *HPHT-treated diamonds*, Handbook of Crystal Growth (2015).

[87] R. L. Patel, *et al.. Sub-nanotesla magnetometry with a fibre-coupled diamond sensor*, Phys. Rev. Applied **14** (2020).

[88] S. Pezzagna, B. Naydenov, F. Jelezko, J. Wrachtrup, J. Meijer. *Creation efficiency of nitrogen-vacancy centres in diamond, New Journal of Physics*, New Journal of Physics **12** (2010).

[89] J. R. Rabeau, P. Reichart, G. Tamanyan, D. N. Jamieson, S. Prawer, F. Jelezko, T. Gaebel, I. Popa, M. Domhan, J. Wrachtrup. *Implantation of labelled single nitrogen vacancy centers in diamond using* ^{15}N., Appl. Phys. Lett. **88** (2006).

[90] N. R. S. Reddy, E. R. Krausz. *Two-laser spectral hole burning in a colour centre in diamond*, J. Lumin. (1987).

[91] E. Rittweger, K. Y. Han, S. E. Irvine, C. Eggeling, S. W. Hell. *STED microscopy reveals crystal colour centres with nanometric resolution*, Nat Photon **3**, 3 (2009).

[92] L. Robledo, H. Bernien, T. van der Sar, R. Hanson. *Spin dynamics in the optical cycle of single nitrogen-vacancy centres in diamond*, New Journal of Physics **13**, 2 (2011).

[93] L. Robledo, H. Bernien, I. van Weperen, R. Hanson. *Control and Coherence of the Optical Transition of Single Nitrogen Vacancy Centers in Diamond.*, Rev. Lett. (2010).

[94] S. Rochester, D. Budker. *NV Centers in Diamond*, Online Tutorial http://budker.berkeley.edu/Tutorials/index.html (2013).

[95] L. Rondin, J.-P. Tetienne, T. Hingant, J.-F. Roch, P. Maletinsky, V. Jacques. *Magnetometry with nitrogen-vacancy defects in diamond*, Reports on Progress in Physics **77**, 5 (2014).

[96] C. Santori, P. E. Barclay, K.-M. C. Fu, R. G. Beausoleil. *Vertical distribution of nitrogen-vacancy centers in diamond formed by ion implantation and annealing.*, Phys. Rev. B (2009).

[97] C. Santori, P. E. Barclay, K.-M. C. Fu, R. G. Beausoleil, S. Spillane, M. Fisch. *Nanophotonics for quantum optics using nitrogen-vacancy centers in diamond.*, Nanotechnology (2010).

[98] V. Shah, S. Knappe, S. P. P. Schwindt, J. Kitching. *Subpicotesla atomic magnetometry with a microfabricated vapour cell*, Nature Photonics **1** (2007).

[99] C. S. Shin, C. E. Avalos, M. C. Butler, D. R. Trease, S. J. Seltzer, J. Peter Mustonen, D. J. Kennedy, V. M. Acosta, D. Budker, A. Pines, V. S. Bajaj. *Room-temperature operation of a radiofrequency diamond magnetometer near the shot-noise limit*, Journal of Applied Physics **112** (2012).

[100] D. A. Simpson, J.-P. Tetienne, J. M. McCoey, K. Ganesan, L. T. Hall, S. Petrou, R. E. Scholten, L. C. L. Hollenberg. *Magneto-optical imaging of thin magnetic films using spins in diamond*, Scientific Reports **6** (2016).

[101] P. Siyushev, F. Kaiser, V. Jacques, I. Gerhardt, S. Bischof, H. Fedder, J. Dodson, M. Markham, D. Twitchen, F. Jelezko, J. Wrachtrup. *Monolithic diamond optics for single photon detection*, Applied Physics Letters **97**, 24 (2010).

[102] S. Steinert, F. Dolde, P. Neumann, A. Aird, B. Naydenov, G. Balasubramanian, F. Jelezko, J. Wrachtrup. *High sensitivity magnetic imaging using an array of spins in diamond*, Review of Scientific Instruments **81** (2010).

[103] J.-H. Storm, P. Hömmen, D. Drung, R. Körber. *An ultra-sensitive and wideband magnetometer based on a superconducting quantum interference device*, Applied Physics Letters **110** (2017).

[104] F. M. Stürner, *et al.*. *Integrated and portable magnetometer based on nitrogen-vacancy ensembles in diamond*, Advanced Quantum Technologies **4** (2021).

[105] J. M. Taylor, P. Cappellaro, L. Childress, L. Childress, L. Jiang, D. Budker, P. R. Hemmer, A. Yacoby, R. Walsworth, M. D. Lukin. *Scanning Confocal Optical Microscopy and Magnetic Resonance on Single Defect Centers.*, Nat. Phys. **276** (2008.).

[106] J. M. Taylor, P. Cappellaro, L. Childress, L. Jiang, P. Neumann, D. Budker, P. R. Hemmer, A. Yacoby, R. Walsworth, M. D. Lukin. *High-sensitivity diamond magnetometer with nanoscale resolution*, Nature Physics **4** (2008).

[107] U. D. Ulusar, J. D. Wilson, P. Murphy, R. B. Govindan, H. Preissl, C. L. Lowery, H. Eswaran. *Bio-magnetic signatures of fetal breathing movement*, Physiological Measurement **32**, 2 (2011).

[108] E. van Oort, N. B. Manson, M. Glasbeek. *Optically detected spin coherence of the diamond N-V centre in its triplet ground state*, J. Phys. C: Solid State Phys. **71** (1988).

[109] E. van Oort, P. Stroomer, M. Glasbeek. *Low-field optically detected magnetic resonance of a coupled triplet-doublet defect pair in diamond*, Phys. Rev. B **42** (1990).

[110] M. M. W., A. S. A. *Colloquium: Quantum limits to the energy resolution of magnetic field sensors*, Rev. Mod. Phys. **92** (2020).

[111] A. Wickenbrock, S. Jurgilas, A. Dow, L. Marmugi, R. Renzoni. *Magnetic induction tomography using an all-optical ^{87}Rb atomic magnetometer*, Optics Letter **39** (2014).

[112] A. Wickenbrock, N. Leefer, J. W. Blanchard, D. Budker. *Eddy current imaging with an atomic radio-frequency magnetometer*, Applied Physics Letters **108** (2016).

[113] A. Wickenbrock, H. Zheng, L. Bougas, N. Leefer, S. Afach, A. Jarmola, V. M. Acosta, D. Budker. *Microwave-free magnetometry with nitrogen-vacancy centers in diamond*, Applied Physics Letters **109** (2016).

[114] A. Wickenbrock, H. Zheng, G. Chatzidrosos, J. S. Rebeirro, T. Schneemann, P. Bluemler. *High homogeneity permanent magnet for diamond magnetometry*, Journal of Magnetic Resonance **322** (2021).

[115] T. Wolf, P. Neumann, K. Nakamura, H. Sumiya, T. Ohshima, J. Isoya, J. Wrachtrup. *Subpicotesla Diamond Magnetometry*, Phys. Rev. X **5** (2015).

[116] J. D. A. Wood, D. A. Broadway, L. T. Hall, A. Stacey, D. A. Simpson, J.-P. Tetienne, L. C. L. Hollenberg. *Wide-band nanoscale magnetic resonance spectroscopy using quantum relaxation of a single spin in diamond*, Phys. Rev. B **94** (2016).

[117] J. D. A. Wood, J.-P. Tetienne, D. A. Broadway, L. T. Hall, D. A. Simpson, A. Stacey, L. C. L. Hollenberg. *Microwave-Free Nuclear Magnetic Resonance at Molecular Scales*, Nature Communications **8** (2017).

[118] X. Zhang, G. Chatzidrosos, Y. Hu, H. Zheng, A. Wickenbrock, A. Jerschow, D. Budker. *Battery characterization via eddy-current imaging with nitrogen-vacancy centers in diamond.*, Appl. Sci. **11** (2021).

[119] H. Zheng, G. Chatzidrosos, A. Wickenbrock, L. Bougas, R. Lazda, A. Berzins, F. H. Gahbauer, M. Auzinsh, R. Ferbe, D. Budker. *Level anti-crossing magnetometry with color centers in diamond*, Proc. of SPIE **2** (2017).

[120] H. Zheng, Z. Sun, G. Chatzidrosos, C. Zhang, K. Nakamura, H. Sumiya, T. Ohshima, J. Isoya, J. Wrachtrup, A. Wickenbrock, D. Budker. *Microwave-Free Vector Magnetometry with Nitrogen-Vacancy Centers along a Single Axis in Diamond*, Phys. Rev. Applied **13** (2020).